Thin Film Fluid Flow Simulation on Rotating Discs

Petr Víta

Dissertation
submitted to
Montanuniversität Leoben

in partial fulfilment of
the requirements for the degree of
Doktor der montanistischen Wissenschaften

May 2016

To my wife Trine
and my children Sebastian and Tobias

Affidavit

I declare in lieu of oath that I wrote this thesis and performed the associated research myself using only literature cited in this volume.

.....
Petr Víta, 19th May 2016

Abstract

Prediction and analysis of complex industrial processes, for example wet chemical wafer etching, depend on accurate modelling of physical phenomena. This work presents a series of numerical studies of film flow with an impinging jet on rotating discs which is the basis for a high performance simulation tool that can be used in design and optimisation of such industrial processes. Numerical studies based on the Volume-of-Fluid (VoF) method were performed and evaluated against reported experimental data. The conclusion drawn is that a transient two-phase 3D free-surface VoF-simulation with a dynamically moving jet is impractical for an industrial use due to very long computational times required. The thin film model based on an integral method, which reduces the three-dimensional nature of the problem into a two-dimensional one by integrating the Navier-Stokes equations over the film thickness, is proposed as a possible remedy. An application of Reynolds decomposition and profile modelling of dependent variables allows capturing of the important inertial and centrifugal forces that would otherwise be lost during the equation transformation. An implementation of the derived thin film model was carried out in the open-source software toolbox OpenFOAM® using the Finite Area method, a specialisation of the Finite Volume method for film flows on the arbitrary surfaces. The resulting code fulfils the requirements of a high-performance transient incompressible solver for the thin film and features a dynamic inlet implementation. The approach is validated with the ANSYS Fluent software and its VoF-implementation. An extension of the solver with a simple diffusion-controlled chemistry model for a wet chemical etching of silicon wafers is presented.

Zusammenfassung

Dünnfilmströmungen auf rotierenden Scheiben, erzeugt durch einen auf die Scheibe auftreffenden Flüssigkeitsstrahl, sind in vielen industriellen Anwendungen, wie zum Beispiel dem nasschemische Ätzen von Wafern, ein wichtiger Prozessparameter. In dieser Arbeit wird eine Serie von numerischen Fallstudien, basierend auf der Volumen-of-Fluid-Methode (VoF), durchgeführt und mit publizierten, experimentellen Daten verglichen. Die Vergleiche zeigen, dass eine vollständige transiente Zweiphasen 3D VoF-Simulation mit einem frei beweglichen Einlass für den industriellen Einsatz aufgrund sehr langer Rechenzeiten nicht praktikabel ist. Daher dient das Dünnfilm-Modell, basierend auf einem integralen Verfahren, welches die dreidimensionale Natur des Problems durch Integration der Navier-Stokes-Gleichungen über die Filmdicke auf zwei Dimensionen reduziert, als Grundlage. Durch die Anwendung der Reynolds Zerlegung und Profilmodellierung von abhängigen Variablen können Trägheits- und Zentrifugalkräfte, die sonst während der Gleichungstransformation verloren gegangen wären, erhalten werden. Die Implementierung des so entwickelten Dünnfilmmodells wurde in der Open-Source-Software-Toolbox OpenFOAM® unter Verwendung der Finite-Area-Methode, welche eine Spezialisierung der Finite-Volumen-Verfahren für Dünnfilmströmungen auf beliebigen Oberflächen ist, umgesetzt. Das resultierende Programm erfüllt die Anforderungen eines transienten, inkompressiblen Hochleistungssolvers für Dünnfilmströmungen, unter Berücksichtigung eines frei beweglichen Einlasses. Die Validierung erfolgte mit der VoF-Implementierung der ANSYS Fluent Software. Eine Erweiterung des Solvers stellt das diffusionsbasierende Modell für nasschemisches Ätzen von Silizium-Wafern dar.

Acknowledgements

I wish to express my deepest gratitude to everyone who supported me in writing of the thesis, in particular, my research supervisor Prof. Wilhelm Brandstätter for his patient guidance, advices and constructive critiques and whom I value as a great mentor.

I am indebted to my project leader Bernhard Gschaider who formed my approach to numerical programming and introduced me to OpenFOAM® for his encouragement, support and new ideas.

I am obliged to colleagues from Graz University of Technology (TU Graz), particularly, to Doris Prieling and Prof. Helfried Steiner for valuable information and research data shared in the project.

I want to thank to Markus Junk, Felix Staudegger and Frank Ludwig Holsteyns from Lam Research AG for their support and discussions on various issues of the research project.

I am very thankful to Clemens Langbauer for the proofreading and comments on the thesis.

I want express my thanks to the colleagues and friends from ICE Strömungsforschung GmbH and Department Petroleum Engineering at Montanuniversität Leoben for making my work an enjoyable place to be in.

Finally I am thankful to my parents, family, for their support and love.

Contents

Chapter 1

Introduction

We meet a plethora of physics phenomena around us every day. One particular group of them is connected to free-surface liquid films. Natural films, be it rivers, lava flows, avalanches, a rain film on a car windshield or a house window or even the liquid film formed in a kitchen sink, are usually driven by gravity. Observations of various wave patterns or a formation of a hydraulic jump may please an observer's eye but there is much more potential hidden in the liquid films. The industry quickly recognised the liquid films' high heat and mass transfer. Especially under centrifugal forces liquid films tend to thin and to accelerate what translates into even higher heat and mass transfer coefficients. Many industrial applications for liquid film flows have been developed–heat pumps, coating processes, desalinisation plants, chemical reactors etc.

The industrial devices usually contain a spinning disc and an inlet opening that allows to control the liquid film formation, its thickness and velocity. The same principle is used as well in the spin processing tool developed by Lam Research[58]. The spin processor is a widespread technology used in the semiconductor industry for wet chemical processing of crystalline silicon substrates, also called wafers, as

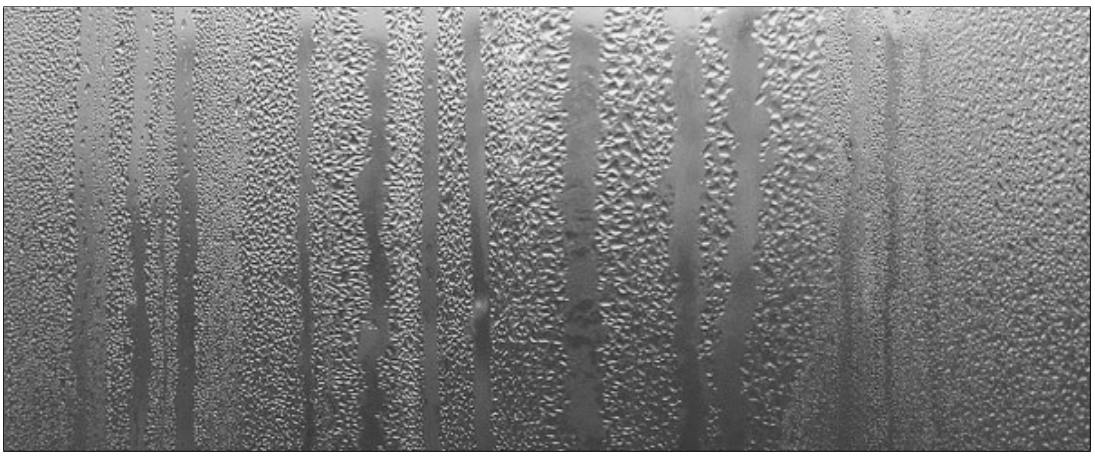

Figure 1.1: Liquid film on a window

(a) Chamber (b) Chuck

Figure 1.2: Spin processor Lam SEZ SP203

described by Junk[52]:

> The wafer is placed on a chuck with the side to be processed facing up inside of the spin processor chamber. A nitrogen cushion protects the bottom side from any contamination. While the chuck and the wafer rotate, chemical mixtures are applied on the wafer by means of a dispenser in order to form a liquid layer on the wafer surface. Dependent on the process step, the dispenser is either in a fixed position (centre or off-centre) or is moving across the wafer surface. The continuously supplied chemicals are spun off the wafer and collected in drain levels surrounding the chuck for recycling.

The spin processor has to clean the wafer as uniformly and with as little liquid as possible while avoiding any damage to the nano-structures on its surface. There are many sources of possible damages which have to be avoided. Let us mention few of the major one such as dry spots on the wafer resulting from liquid film discontinuity, droplet formation in the processing chamber especially at the spinning disc edge or an excessive shear stress at the bottom of the film directly acting on the wafer surface structures that could lead, for example, to a photo resist lift-off[34]. The semiconductor industry–striving to increase process efficiency, yield and cost savings of expensive etching chemicals–is thus highly interested in the understanding of the liquid film dynamics.

1.1 Previous Works

The understanding of the fluid film flow regimes was historically achieved through experiments and analytical modelling. The first investigated thin films have been driven mainly by gravity forces, either falling thin films or thin films on an inclined

surface. Later there has been a growing interest in film flows driven by centrifugal forces.

All film flows share common features; however, they can be classified concerning the effect of inertial forces which either are neglected or are seen to be significant. There are numerous scientific works providing comprehensive reviews on the liquid film dynamics, e.g. Chang and Demekhin[21], Craster and Matar[23].

The experimental works are focusing on the measurement of the film thickness and classification of the wave formations. The rotating disc makes the film thickness measurement challenging and various contact and contactless measurement techniques have been introduced. The observation of the wave formations and their classification are usually based on the photographic material. The hydraulic jump, an abrupt increase of the film height as supercritical flow is slowed down and converts its kinetic energy into potential one, has as well captured an attention of researchers.

One of the first contact measuring methods was a needle probe applied by Espig and Hoyle[29] which allowed to find out the peak values for the fluid film thickness (that is the height of the film to the crest of the film waves). Their measurements have been correlated to the Nusselt flat-film solution. The very same contact technique was used as well by Leshev and Peev[63]. They confirmed dominance of inertial forces and continuously decreasing film thickness with increasing disc radius. Farther Leshev and Peev observed onset of the hydraulic jump at low rotation velocities and correlated the influence of disk revolutions, liquid properties and flow rate on the jump position with Ekman, Reynolds and Weber numbers. Bush and Arristof[17] studied and measured the formation of a circular hydraulic jump on a stationary plate as well with a needle method. Their work linked the surface tension effects to the formation of the hydraulic jump.

Figure 1.3: Hydraulic jump in a sink

The limitations of the contact measuring approaches led to development of the contactless, electrical and optical, measuring methods.

Charwat et al.[22] used an optical method based on an absorption of the infrared light in different solutions flowing on the rotating disc made out of an optical glass. This technique allowed to measure time averaged film thickness and the

results showed significantly lower film thicknesses as expected from the analytical asymptotic solution. This is not surprising as the influence of the inertial forces was generally neglected in the asymptotic solutions. Woods[117] applied a similar technique, measuring the intensity of the light passing through a dye coloured water film and was able to accurately capture an instantaneous shape of the wavy free-surface. Ozar et al.[76] used laser light interface reflection to get readings of the instantaneous film thickness over a segment of the disc. Ozar reported existence of the three main regions on the rotating disc–an inertia dominated region with prevalence of inertial and frictional forces, a rotation dominated region where centrifugal forces are dominant and a transition region with characteristics of both inertia- and rotation-dominated regions. Additionally their method showed the relative importance of radial and tangential forces and their influence on the propagation of the formed surface waves.

Miyasaka[68] conducted measurements based on a liquid conductivity with a focus on the radially inner flow region. This electrical method limited measurements to only a few discrete points. The more efficient approach is for example based on a capacitance sensor as used by Spiers[98] or Thomas et al.[101]. The capacitance technique can measure the film thickness all along the radius of the disc and is more suitable for heat transfer experiments as the disc can be made out of a metal. Another electrical measuring method used by Burns et al.[16] exploited an electrical resistance. Once again it was experimentally confirmed that Nusselt flat-film model cannot cope with strong inertial effects and the use of the more complex 2D Pigford model of Wood and Watts[116] was suggested.

The falling films provided the first insight into the problem. One of the well known steady-state solutions of the Navier-Stokes equations for a thin film falling in the gravity field presented Nusselt[73]. The film flow instabilities which lead to interesting wave patterns have been studied both in experiments, e.g. Kapitza and Kapitza[54], Binnie[9], and analytical methods, e.g. Yih[119], Benjamin[7] and Benney[8].

Benney presented a single evolution equation for the film thickness. However, it is relevant only for flows with low inertial forces. The more interesting flow regimes with higher Reynolds numbers and thus stronger inertial effects have been investigated by Shkadov[95]. He used a combination of the boundary layer theory and Karmán-Pohlhausen integral method to analyse a film flow. The Shkadov model, known as Integral Boundary Layer (IBL) model, forms a coupled system of nonlinear hyperbolic partial differential equations which are solved for depth-averaged flow variables assuming polynomial velocity profiles. The IBL model was used to classify wave patterns by Bunov et al.[14], Sisoev and Shkadov[97]. Further improvements of the IBL model by Ruyer-Quil and Manneville[91] led to the development of the Weighted Residual Integral Boundary Layer (WRIBL) model. The qualities of the WRIBL model have been validated by Liu et al.[64],

Park and Nosoko[78].

Film flows driven by centrifugal forces on the rotating disc, the main focus of the thesis, are closely connected to falling film flows and most findings from the research of falling films apply. The main difference is however, varying acceleration in the radial direction. If a rotating reference frame is used, centrifugal forces and Coriolis forces are occurring. These apparent forces are considered, for example, by Momoniat and Mason[69], Myers and Lombe[71].

The low Reynolds number regimes with negligible inertial forces are directly comparable with falling films, as shown by Prieling[82]:

> ... the centrifugal force term is driving the radial motion equivalently to gravitational force term in the Nusselt flat-film solution for falling liquid films.

The typical flow regimes of interest are however of moderate and higher Reynolds numbers implying strong inertial forces.

The analytical solutions and approximations for liquid films on the rotating discs are derived from the falling films origins and directly connect to the Nusselt flat-film solution replacing the gravity term with a centrifugal force term. Rauscher et al.[87] used an asymptotic expansion of the Navier-Stokes equations with free-surface boundary condition at the liquid-gas interface. The existence of the inner and outer region observed by Ozar was identified in the steady-state solution by Needham and Merkin[72] who used the method of matched asymptotic expansions. The IBL model was as well directly applied to modelling of liquid films on a rotating disc and the selection of the velocity profiles in the underlaying Karmán-Pohlhausen method was found to be of great importance. Matar and Lawrence[66] selected analytically calculated parabolic velocity profile, albeit with shortcomings in the inner flow region. The quartic velocity profiles selected by Kim and Kim[56] proved to be in better agreement with the results of the Navier-Stokes equations. Their solution included surface tension effects. Bohr et al.[11] used the IBL model to analyse the hydraulic jump formation and concluded that the IBL model is able to capture the structure of the both, linear and circular, hydraulic jumps.

However experiments are limited by technical possibilities and analytical solutions by assumptions placed on the model. Therefore it does not come as a surprise that with the advent of Computational Fluid Dynamics (CFD) the interest shifted toward numerical investigations of liquid films. Solutions with little or no assumptions are very intriguing and thus numerical simulations of the Navier-Stokes equations are considered by many.

Malamataris and Papanastasiou[65] used a Galerkin Finite Element (FE) method[4] to analyse three cases of unsteady free surface flows on a vertical plate. To lower computational costs they truncated the domain and imposed a free bound-

ary condition[77] at the outlet. A bit more demanding approach, steady-state 2D Volume-of-Fluid (VoF) method for tracking of the liquid-gas interface with Continuum Surface Force (CSF) model[13] to include surface tension effects was used by Gao et al.[38]. Very good agreement with experimental and analytical works was reported including the existence of recirculation zones in large waves. An increasing interest in the numerical simulation of the free-surface flows put into focus the VoF method and its interface tracking models. Gopala and van Wachem[39] investigated different interface tracking models and their influence on VoF solutions. Tuković and Jasak[102] presented 2D simulations of a thin liquid film on an arbitrary surface using the Finite Area (FA) method implemented in OpenFOAM®[74, 112, 51].

Special attention was payed to the simulation of the hydraulic jump. Zhou and Stansby[123] investigated the hydraulic jump in a straight open channel with the Shallow Water (SW) equations in their strong conservation form. The equations were solved with a steady-state 2D Finite Volume (FV) method. The solution showed good agreement with experimental data but it worked with semi-empirical bed friction coefficients for modelling of the shear-stress at the film bottom. Yokoi and Xiao[120, 121] used a 2D VoF method (CIP-CUP algorithm[118, 60]) with CSF model for surface tension modelling. They classified the hydraulic jumps into two categories and confirmed numerical difficulties in the modelling of the reverse roller connected to the selection of the velocity profile function.

A notable numerical simulation of the liquid film on a rotating disc presented Rahman and Faghri[85]. They used steady-state axisymmetric Finite Difference (FD) method for modelling of a film flow where a free-surface is forming an upper boundary of the computational domain, effectively closing the gas phase out. A similar approach as Gao et al., a steady-state 2D axisymmetric VoF method, was applied by Rice et al.[89] to liquid films on rotating discs. Their results showed reasonable agreement with observations of experiments by Thomas et al.[101] and Ozar et al[76]. Finally Kaneko et al.[53] performed 2D axisymmetric VoF simulations to investigate the flow on a wafer. Their model additionally contained a species transport equation for a simple diffusion controlled chemical etching model. The computed etching rate was found to be in good agreement with experimental results.

It has to be mentioned that current state of the art of numerical simulations of liquid films is not satisfactory. Thin films tend to have excessively high requirements on the spatial resolution due to their large disparity between the governing length scales. The computational complexity is increased even more should the heat and mass transfer or supporting chemical models be included. As a result a full scale 3D free-surface numerical simulation is not yet, at the time of writing, economical and hence simplified solutions–2D domains or axisymmetric domain cuts, symmetry exploiting central impingements, static inlets–are still state of the

art.

1.2 Objectives

The current state of the art of a liquid film research has been described in the previous section. The limitations of free-surface numerical simulations are especially unsatisfactory. There is a clear need for affordable simulation tools which would support design and optimisation of the industrial devices.

The semiconductor industry, for example, is very interested in transient simulations that would cover the whole etching process length, in simulations where the impingement of the etching chemicals is a dynamic rather as a static process, in simulations that can handle chemical models next to the heat and mass transfer. In fact the industry is ready to sacrifice an exact solution and accept an approximation with a reasonable agreement could above mentioned features, even partially, be met.

The main goals of the thesis are therefore:

- Development of a thin film model for high inertial and centrifugal forces.
- Implementation of the thin film model into a fast transient numerical solver with a dynamically moving inlet. The solver has to be robust enough to accommodate an extension with a chemical etching model.
- Validation of the solver against experimental data and 3D VoF simulations without additional assumptions.

1.3 Outline

The thesis is structured into the following chapters:

Chapter 1: Introduction provides a context and a motivation for the thesis. An overview of a previous research is presented and the objectives are set.

Chapter 2: Governing Equations introduces governing equations of the fluid mechanics which are forming the theoretical background of the work and provide the starting point to the derivation of the thin film model.

Chapter 3: Volume-of-Fluid Simulations presents the VoF method and 2D and 3D numerical simulations of the liquid films investigated in the selected experiments.

Chapter 4: Thin Film Model shows a derivation of the thin film model based on the shallow water equations and velocity profile functions by Karmán-Pohlhausen method. An innovative approach of Reynolds decomposition applied into modelling of the shallow water boundary layer in order to capture the inertia terms is presented.

Chapter 5: Thin Film Approximation presents an application of the thin film model under locally invalid assumptions, so called Thin Film Approximation (TFA), at the 2D numerical simulation based on the FA method. A primer on FA method and details of the TFA solver implementation are given. The results of 2D TFA simulations are compared with 3D VoF numerical simulation.

Chapter 6: Chemistry Model provides details on a simple diffusion-controlled chemistry model for the wet etching of the wafers based on the thin film model.

Chapter 7: Summary and Conclusion discusses the achieved results, challenges and possible new directions for future work.

Chapter 2

Governing Equations

In what follows, the underlaying mathematical framework for liquid films is presented. This provides the necessary basis for the rest of the thesis and is a summary of textbooks, lecture notes, e.g. Versteeg and Malalasekera[107], Blazek[10], Batchelor[6], Jasak[50], Cebeci and Bradshaw[20], Zienkiewicz and Taylor[124], Abeyaratne[1], Wilcox[114], Sert[94], Gurtin[43], Petrila and Trif[81], Patankar[79] and other resources[19, 2] on fluid mechanics.

2.1 Conservation Laws

The conservation laws give a relation between the quantity of the conserved property and its transport. Generally they state that the amount of the conserved property within a volume can only change by the amount of the property which flows in or out of the volume. The following conservation laws–conservation of mass, momentum and energy–are valid for any continuum.

2.1.1 Material Derivative

Let ϕ be a general material scalar property, such as pressure, density etc.

$$\phi = \phi(t, \mathbf{x}) \tag{2.1}$$

carried by the velocity field $\mathbf{u}$

$$\mathbf{u} = \mathbf{u}(t, \mathbf{x}) \tag{2.2}$$

in time t and position $\mathbf{x}$.

The time variation of the material property ϕ following the motion of its volume is then known as a *total derivative* or a *material derivative*

$$\frac{d\phi}{dt} = \frac{\partial \phi}{\partial t} + \mathbf{u} \cdot \nabla \phi \tag{2.3}$$

2.1.2 Reynolds Transport Theorem

Let V_M be a material volume bound by its surface ∂V_M with $\mathbf{n}$ being an outward-pointing unit normal vector on the boundary ∂V_M.

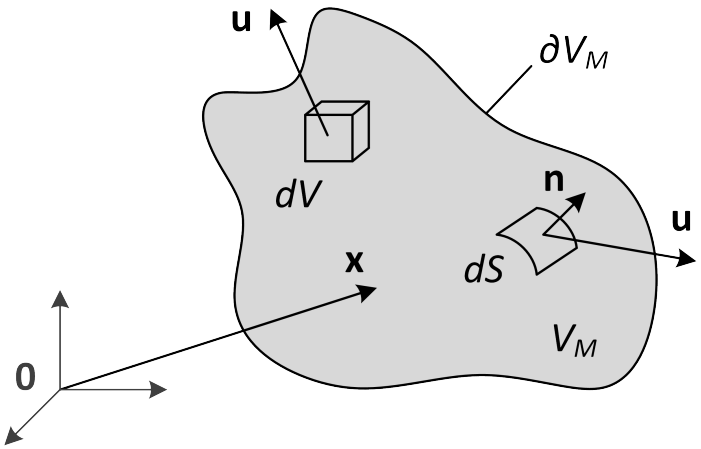

Figure 2.1: Material body

The *Reynolds transport theorem* states the rate of change of the scalar material property ϕ in time

$$\frac{d}{dt}\int_{V_M(t)} \rho\phi(t,\mathbf{x})\, dV = \frac{\partial}{\partial t}\int_{V_M(t)} \rho\phi\, dV + \oint_{\partial V_M(t)} (\rho\mathbf{u}\phi)\cdot\mathbf{n}\, dS \tag{2.4}$$

Because the rate of change of the scalar material property ϕ in the material volume V_M is equal to its volume sources S_V and surface sources $\mathbf{S}_S$

$$\begin{aligned}\frac{\partial}{\partial t}\int_{V_M(t)} \rho\phi\, dV + \oint_{\partial V_M(t)} (\rho\mathbf{u}\phi)\cdot\mathbf{n}\, dS = \\ \int_{V_M(t)} S_V(\phi)\, dV + \oint_{\partial V_M(t)} \mathbf{S}_S(\phi)\cdot\mathbf{n}\, dS\end{aligned} \tag{2.5}$$

applying the Gauss' divergence theorem, Appendix B.2.1, one can write in the differential form

$$\frac{\partial\rho\phi}{\partial t} + \nabla\bullet(\rho\mathbf{u}\phi) = S_V(\phi) + \nabla\bullet(\mathbf{S}_S(\phi)) \tag{2.6}$$

2.1.3 Conservation of Mass

The conservation of mass states that the rate of increase of mass in a volume is equal to net rate of mass flux in and out of a volume. The differential form with mass per unit volume, i.e. density ρ

$$\frac{\partial\rho}{\partial t} + \nabla\bullet(\rho\mathbf{u}) = 0 \tag{2.7}$$

is known as a *continuity equation*.

2.1.4 Conservation of Momentum

2.1.4.1 Conservation of Linear Momentum

The *Newton's second law of motion* states that a rate of change of the linear momentum is equal to the net acting force.

The net acting force can be split into body forces, e.g. gravity, electromagnetic forces, and surface forces, e.g. pressure force, viscous forces. The common practise in continuum mechanics is to keep the body forces $\mathbf{F}_b$ as separate source terms while the surface forces are being transformed into the *Cauchy stress tensor* $\mathbf{T}$.

Based on the Reynolds transport theorem one can then express the Newton's second law of motion in the differential form known as a *Cauchy momentum equation*

$$\frac{\partial \rho \mathbf{u}}{\partial t} + \nabla \bullet (\rho \mathbf{u}\mathbf{u}) = \nabla \bullet \mathbf{T} + \mathbf{F}_b \tag{2.8}$$

where expression $\rho\mathbf{u}$ is called a *momentum density*.

2.1.4.2 Conservation of Angular Momentum

Similarly a rotational analogy to the Newton's second law of motion can be defined stating that a rate of change of angular momentum is equal to the net acting torque and occurs about the same axis as that torque.

The conservation of the angular momentum is then expressed in the differential form in an analogy to the equation 2.8

$$\frac{\partial \rho(\mathbf{x} \times \mathbf{u})}{\partial t} + \nabla \bullet \left[\rho \mathbf{u}(\mathbf{x} \times \mathbf{u})\right] = (\mathbf{x} \times \nabla \bullet \mathbf{T}) + (\mathbf{x} \times \mathbf{F}_b) \tag{2.9}$$

2.1.4.3 Stress Tensor Symmetry

The conservation of the angular momentum for a continuum requires that the Cauchy stress tensor $\mathbf{T}$ has to be symmetric[3] in order to satisfy the conservation of the linear momentum

$$T_{ij} = T_{ij} : \mathbf{T} = \mathbf{T}^T \tag{2.10}$$

2.1.5 Conservation of Energy

The *first law of thermodynamics* formulates conservation law of energy as a rate of change of the energy being equal to the net rate of energy added to the volume and the net rate of work done on it.

The net rate of energy added to the volume is based on the volumetric energy sources Q and the heat flux $\mathbf{q}$ through the surface. The rate of work done on the

volume is a product of the force $\mathbf{F}$ and the velocity $\mathbf{u}$.

Using the Reynolds transport theorem, the energy equation for the total energy E is written in the differential form as

$$\frac{\partial \rho E}{\partial t} + \nabla\bullet\left(\rho \mathbf{u} E\right) = \nabla\bullet\left(\mathbf{T}\cdot\mathbf{u}\right) + \nabla\bullet\,\mathbf{q} + \mathbf{F}_b\cdot\mathbf{u} + \rho Q \tag{2.11}$$

where the expression ρE is called an *energy density*.

2.1.6 Entropy Inequality

The *second law of thermodynamics* postulates the thermodynamic process irrevesibility by stating that the specific entropy s of the system always increases. The idealised case of reversible processes allows the entropy to remain the same.

The differential form of the second law of thermodynamics for both reversible and irreversible processes is known as the *entropy inequality*

$$\frac{\partial \rho s}{\partial t} + \nabla\bullet\left(\rho \mathbf{u} s\right) \geq \nabla\bullet\left(\frac{\mathbf{q}}{T}\right) + \frac{\rho Q}{T} \tag{2.12}$$

where T is the temperature of the system.

2.2 Constitutive Relations

Unfortunately, the conservation laws of continuum mechanics presented in the section 2.1 are indeterminate. There are more unknown quantities as number of equations itself. Therefore so called *constitutive relations* which contribute to the mathematical closure of the equations system have to be introduced. These constitutive equations depend on the material properties of the matter.

2.2.1 Newtonian Fluids

One of the fundamental characteristics of the fluid is its inability to sustain shear stresses when at rest. In such a situation only hydrostatic pressure is possible. Therefore the shear stresses are directly connected to the fluid motion.

The primary cause of the stresses $\mathbf{T}$ are strain rates ϵ defined in an analogy to infinitesimal strain as

$$\epsilon = \frac{1}{2}\left[\nabla\mathbf{u} + \left(\nabla\mathbf{u}\right)^T\right] \tag{2.13}$$

Fluids are called *Newtonian* or *viscous* if the shear stress is proportional to the velocity gradient. That is the relationship between the deviatoric stress tensor τ and the rate-of-strain tensor ϵ is linear. The proportionality coefficient is the

dynamic viscosity μ.

The *Newton's law of viscosity* for isotropic[1] fluids, using the Stokes' hypothesis[2][100], written in the differential form

$$\begin{aligned}\mathbf{T} = \tau - p\mathbf{I} &= 2\mu\epsilon - \frac{2}{3}\mu(\nabla\!\bullet\,\mathbf{u})\mathbf{I} - p\mathbf{I} \\ &= -\left(p + \frac{2}{3}\mu\nabla\!\bullet\,\mathbf{u}\right)\mathbf{I} + \mu\left[\nabla\mathbf{u} + (\nabla\mathbf{u})^T\right]\end{aligned} \tag{2.14}$$

2.2.2 Internal Energy

The energy conservation equation 2.1.5 introduced the total energy E. The total energy E is understood as a sum of the internal energy e and all other energies

$$E = e + e_k + \text{other forms of energy} \tag{2.15}$$

where the internal energy e is a function of the pressure p and the temperature T

$$e = e(p, T) \tag{2.16}$$

and the kinetic energy e_k is defined as

$$e_k = \frac{1}{2}\mathbf{u} \cdot \mathbf{u} \tag{2.17}$$

Using the definition of the internal energy e, an enthalpy h is defined as

$$h = e + \frac{p}{\rho} = e + pv \tag{2.18}$$

where v is a specific volume.

There exists a useful relation which links the enthalpy h to the temperature T at constant pressure, i.e. $dp = 0$

$$\left(\frac{\partial h}{\partial T}\right)_p = \left(\frac{\partial e}{\partial T}\right)_p + p\left(\frac{\partial v}{\partial T}\right)_p = c_p \tag{2.19}$$

where c_p is the specific heat capacity at constant pressure.

[1] There is no directional preference in the isotropic material.

[2] Stokes' hypothesis neglects a bulk viscosity that is the effect of a volumetric viscosity. This simplification proved itself practical, however recent research[36, 15] shows that it is not always a valid assumption.

2.2.3 Equation of State

The equation of state links together properties of the system which depends on its current thermodynamic state.

The general form of the equation of state for the fluids binds together pressure p, temperature T and density ρ

$$\rho = \rho(p, T) \tag{2.20}$$

and specialisations exists based on the fluid material.

The most simple model is an incompressible isothermal fluid where density is constant

$$\rho = \text{const.} \tag{2.21}$$

2.2.4 Law of Heat Conduction

The *law of heat conduction* also known as *Fourier's law* states that the rate of the heat transfer through the matter is proportional to the negative temperature gradient.

Fourier's law written in the differential form

$$\mathbf{q} = -\lambda \nabla T \tag{2.22}$$

where λ is a heat conductivity coefficient.

2.3 Navier-Stokes Equations

The conservation laws together with constitutive relations form a closed system of non-linear partial differential equations called *conservative*[3] *Navier-Stokes equations* that govern the time dependent three-dimensional fluid flow and energy transfer of a compressible isotropic Newtonian fluid

- Continuity equation

$$\frac{\partial \rho}{\partial t} + \nabla \bullet (\rho \mathbf{u}) = 0 \tag{2.23a}$$

- Momentum equation

$$\frac{\partial \rho \mathbf{u}}{\partial t} + \nabla \bullet (\rho \mathbf{u}\mathbf{u}) = -\nabla \left(p + \frac{2}{3}\mu \nabla \bullet \mathbf{u} \right) + \nabla \bullet \left(\mu \left[\nabla \mathbf{u} + (\nabla \mathbf{u})^T \right] \right) + \mathbf{F}_b \tag{2.23b}$$

[3] An equation system derived from conservation laws is called conservative.

- Energy equation

$$\frac{\partial \rho\left(u+e_k\right)}{\partial t}+\nabla\boldsymbol{\cdot}\left[\rho\mathbf{u}\left(u+e_k\right)\right]=-\nabla\boldsymbol{\cdot}\left(p\mathbf{u}\right)-\nabla\boldsymbol{\cdot}\left(\frac{2}{3}\mu\left(\nabla\boldsymbol{\cdot}\,\mathbf{u}\right)\mathbf{u}\right)+\nabla\boldsymbol{\cdot}\left(\mu\left[\nabla\mathbf{u}+\left(\nabla\mathbf{u}\right)^{T}\right]\cdot\mathbf{u}\right)+\nabla\boldsymbol{\cdot}\left(\lambda\nabla T\right)+\mathbf{F}_b\cdot\mathbf{u}+\rho Q \tag{2.23c}$$

- Equation of State

$$\rho=\rho(p,T) \tag{2.23d}$$

- Transport coefficients

$$\lambda=\lambda(p,T) \tag{2.23e}$$

$$\mu=\mu(p,T) \tag{2.23f}$$

2.3.1 Internal Energy Equation

Taking a total energy equation and subtracting a dot product of the momentum equation with the velocity $\mathbf{u}$ provides an internal energy equation

$$\frac{\partial \rho e}{\partial t}+\nabla\boldsymbol{\cdot}\left(\rho\mathbf{u}e\right)=\underbrace{\nabla\mathbf{u}\,\boldsymbol{:}\left[\mu\left[\nabla\mathbf{u}+\left(\nabla\mathbf{u}\right)^{T}\right]-\left(\frac{2}{3}\mu\nabla\boldsymbol{\cdot}\,\mathbf{u}\right)\mathbf{I}\right]}_{\text{viscous dissipation}}-p\nabla\boldsymbol{\cdot}\,\mathbf{u}+\nabla\boldsymbol{\cdot}\left(\lambda\nabla T\right)+\rho Q \tag{2.24}$$

2.3.2 Incompressible Isothermal Fluids

The compressible formulation of the Navier-Stokes equations can be further simplified for a category of incompressible isothermal fluids where the density ρ is constant

- Continuity equation

$$\nabla\boldsymbol{\cdot}\,\mathbf{u}=0 \tag{2.25a}$$

- Momentum equation

$$\rho\left[\frac{\partial\mathbf{u}}{\partial t}+\nabla\boldsymbol{\cdot}\left(\mathbf{u}\mathbf{u}\right)\right]=-\nabla p+\nabla\boldsymbol{\cdot}\left(\mu\nabla\mathbf{u}\right)+\mathbf{F}_b \tag{2.25b}$$

- Energy equation

$$\rho c_p\left[\frac{\partial T}{\partial t}+\nabla\boldsymbol{\cdot}\left(\mathbf{u}T\right)\right]=\nabla\boldsymbol{\cdot}\left(\lambda\nabla T\right)+\rho Q \tag{2.25c}$$

is based on the internal energy equation 2.24, the enthalpy-temperature relationship 2.19 and neglecting of the viscous dissipation.

while the rest of equations closure remains the same.

The constant density assumption decouples the continuity and the momentum equation from the energy equation. As a result only a solution of the continuity and the momentum equation is necessary, the energy equation can be solved a posteriori using the velocity field solution to find the energy distribution.

The numerical solution of the incompressible flow is considered more difficult compared to the compressible flows. The main difficulty is hidden in the pressure as it cannot be related to density or temperature through the equation of state. In fact the pressure establishes itself instantaneously in a flow field so that the velocity field always remains divergence free. There is no pressure term in the continuity equation and there are only pressure derivatives in the momentum equation. Thus value of pressure itself in the incompressible flow solution is secondary to the changes of pressure in the space.

2.4 General Transport Equation

The previous equations have similar structure that can be captured into a general transport equation[50] for a tensorial flow property χ

$$\underbrace{\frac{\partial \rho\chi}{\partial t}}_{\text{temporal term}} + \underbrace{\nabla\bullet\left(\rho\mathbf{u}\chi\right)}_{\text{convective term}} = \underbrace{\nabla\bullet\left(\rho\Gamma_\chi\nabla\chi\right)}_{\text{diffusive term}} + \underbrace{S_\chi(\chi)}_{\text{source term}} \tag{2.26}$$

where Γ_χ is a tensorial property coefficient and S_χ is a tensorial property source.

Applying the Gauss' divergence theorem, Appendix B.2.1, on the general transport equation and integrating over a small time interval Δt with respect to time t the most general integral form[107] can be written

$$\begin{aligned}\underbrace{\int_t^{t+\Delta t}\left(\frac{\partial}{\partial t}\int_{V_M(t)}\rho\chi\,dV\right)dt}_{\text{temporal term}} + \underbrace{\int_t^{t+\Delta t}\left[\oint_{\partial V_M(t)}(\rho\mathbf{u}\chi)\cdot\mathbf{n}\,dS\right]dt}_{\text{convective term}} \\ = \underbrace{\int_t^{t+\Delta t}\left[\oint_{\partial V_M(t)}\left(\rho\Gamma_\chi\nabla\chi\right)\cdot\mathbf{n}\,dS\right]dt}_{\text{diffusive term}} + \underbrace{\int_t^{t+\Delta t}\left[\int_{V_M(t)}S_\chi(\chi)\,dV\right]dt}_{\text{source term}}\end{aligned} \tag{2.27}$$

The general transport equation is a usual starting point for a discretisation of equations for a numerical simulation.

2.4.1 Species Concentration Equation

A continuum can be a mixture of various *species* which are mixed together at the molecular level. Such a mixture share the same velocity, pressure and temperature and there can exist a mass transfer between phases by convection and diffusion.

A species concentration c_i of the i^{th} species of the mixture, also called a *mass fraction*, is defined as

$$c_i = \frac{m_i}{m} \tag{2.28}$$

where m_i is a mass of the i^{th} species and m is the mass of the mixture.

The species transport equation of the i^{th} species of the mixture, utilising the general transport equation 2.26, has the differential form

$$\frac{\partial \rho c_i}{\partial t} + \nabla\bullet\left(\rho \mathbf{u} c_i\right) = \nabla\bullet\left(\rho D_{c_i} \nabla c_i\right) + S_{c_i} \tag{2.29}$$

where D_{c_i} represents the i^{th} species concentration diffusion coefficient and S_{c_i} is the i^{th} species concentration source.

It follows out of the species concentration definition 2.28 that

$$\sum_{i=0}^{\mathcal{N}} c_i = 1 \tag{2.30}$$

and it is necessary to solve the species transport equation only for $\mathcal{N} - 1$ species as the species with index 0 is called a *background* or a *carrier fluid*.

2.5 Statistical Modelling

Most fluid flows are in a state of continuous instability called *turbulence* and can be considered steady only on an average basis as small fluctuations of all flow quantities are always present. If a flow exhibits these instabilities and fluctuations in the macroscopic scale it is called a *turbulent flow*. A flow free of these fluctuations in the macroscopic scale, a well ordered flow, is called *laminar flow*.

As this thesis is focused on the laminar flows, only the relevant idea of *Reynolds averaging* used in the turbulence modelling, namely Reynolds Averaged Navier-Stokes (RANS) equations, will be presented.

2.5.1 Reynolds Averaging

The RANS equations are obtained through a statistical description of the turbulent flow based on the averaging of the flow quantities.

The idea behind Reynolds averaging is to express every dependent variable as the sum of its mean, or time averaged, value $\overline{\phi}$ and its fluctuating component, also called *perturbation*, ϕ'

$$\phi(\mathbf{x}, t) = \overline{\phi}(\mathbf{x}) + \phi'(\mathbf{x}, t) \tag{2.31}$$

where

$$\overline{\phi}(\mathbf{x}) = \lim_{\mathcal{N}\to\infty} \frac{1}{\mathcal{N}} \sum_{i=1}^{\mathcal{N}} \phi_i(\mathbf{x}, t) \tag{2.32}$$

and $\mathcal{N}$ is a number of repeated experiments.

The time averaged quantities are then substituted into Navier-Stokes equations 2.23. The transformation yields RANS equations which are nearly identical with the original equations but they introduce a new term in the general form of a mean value of a product of perturbations

$$\rho\overline{\phi'\mathbf{u}'}$$

As the fluctuations themselves are unknown, a supporting model has to be supplied that expresses these terms as a correlation of the fluctuations in terms of the mean quantities.

In the case of the RANS the supporting model is the turbulence model and one of the most popular are, for example, *eddy-viscosity models* that relate an analogy between the turbulent and viscous diffusion.

Chapter 3

Volume-of-Fluid Simulations

Numerical investigations of thin films are usually based on techniques for simulation of free-surface flows. The most frequently used one is the Volume-of-Fluid (VoF) method. The VoF approach is very straightforward; however, in 3D cases it may become computationally intensive. This chapter starts with the series of numerical investigations based on 2D axisymmetric VoF method implemented in the open-source software toolbox OpenFOAM®. The investigated test cases are selected from the experiments of Ozar et al.[76], Thomas et al.[101] and Charwat et al.[22]. 3D VoF simulations for specific cases are also presented in order to get an idea on computational expenses of a full 3D simulation. The chapter shows limitations of the VoF method and provides a motivation for a new approach.

3.1 Free-Surface Flows

Before the choice of simulation method is made, it is important to think about the free-surface behaviour of two immiscible fluids. Based on the interfacial behaviour of involved phases three general cases exist–segregated, transitional and dispersed flows.

In order to better describe the three groups an example from the Comet manual[19] is taken. One can consider a closed volume partially filled with a liquid where a gas is filling up the rest. The *segregated flow* class is present when the closed volume will oscillate with a low frequency and amplitude, so that both phases will stay separated with a single well defined interface. The *mixed* or *transitional* flow occurs when the oscillation frequency and amplitude increases enough so that the surface waves of the liquid become unstable and break. That leads to situation where the interface breaks into small bubbles of liquid trapped in the gas and vice versa. The *dispersed flow*, the last class, happens when the closed volume is shaken aggressively and both phases mix together forming a suspension[1].

[1]A suspension is a heterogeneous mixture containing particles that are sufficiently large for

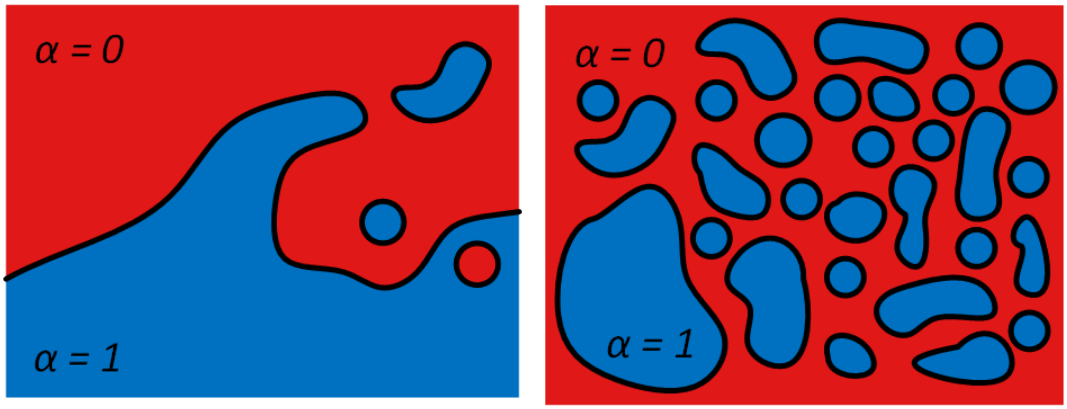

(a) Transitional flow (b) Dispersed flow

Figure 3.1: Flow classes

Two main methods for treatment of free-surface problems–front-tracking and front-capturing–exist.

3.1.1 Front-Tracking Method

The continuum concept is not holding across the free surface as the physical properties of fluid phases do not change continuously across it. However, the governing equations can be applied to each phase separately as phases are immiscible. The front-tracking, also called *surface-tracking*, method does this by dividing the solution domain into separated sub-domains where every sub-domain contains only a single phase. The interface between the phase sub-domains forms the free-surface.

The free-surface is thus known whole time and changes its shape based on the phase interactions. That inherently enforces computational domains with moving boundaries and respective boundary conditions–kinematic and dynamic–at the phase interface.

The kinematic boundary condition forbids the convective mass transfer through the phase interface

$$(\mathbf{u} \cdot \mathbf{n})_{fs} = 0 \tag{3.1}$$

where $\mathbf{n}$ is the normal of the free-surface that is denoted by fs.

The dynamic condition describes the force balance acting on the phase interface. In other words the forces–surface tension, viscous effects and pressure–acting on both fluids at the free-surface are in equilibrium.

The major advantage of the method is knowledge about the interface shape and position whole time what simplifies an inclusion of surface tension forces. The disadvantage of the method is connected to a complexity of the free-surface tracking should the phase interface become too complex or more domains exist.

a sedimentation. Thus suspension will eventually settle separating its phases.

3.1.2 Front-Capturing Method

The front-capturing method requires a two-phase model. Instead of keeping a separate homogeneous continuum model for each phase, an effective continuum fluid model of the mixture in a single computational domain is constructed. The properties of the effective fluid are based on the properties of its constituent phases and a newly introduced scalar volume fraction α

$$\phi = \alpha\phi_0 + (1 - \alpha)\phi_1 \tag{3.2}$$

where subscripts 0 and 1 denotes phases. The volume fraction value 0 and 1 tracks the phases respectively and values in between mark the presence of the interface.

The volume fraction α allows to properly resolve transport of the phase masses in the domain. This is achieved by linking of the volume fraction α with the mass fraction c of the fluid 1

$$c = \alpha\frac{\rho_1}{\rho} \tag{3.3}$$

under assumption that both phases have the same velocity, pressure and temperature at the interface. This transforms the front-capturing method on the multi-species flow modelling, see Subsection 2.4.1, where fluid 1 can be treated as species and fluid 0 become the carrier fluid.

The major advantage is no computational overhead with increasing amount of phase domains. The major disadvantage is certain level of a numerical diffusion in regard to the shape and position of the interface. That spells problems with modelling of the surface tension effects.

3.1.3 Surface Tension

An important force, especially in the case of liquid and gas, acting on the interface of two fluids is the surface tension. The surface tension is a force normal to the curved interface

$$\mathbf{F}_\sigma = \sigma\kappa\mathbf{n} \tag{3.4}$$

where σ is the surface tension coefficient, κ is the surface curvature and $\mathbf{n}$ is the free-surface unit normal vector pointing outward into the gas.

The tangential surface tension effects

$$\begin{aligned} \mathbf{F}_{\sigma,x} &= \frac{\partial\sigma}{\partial x}\mathbf{x} \\ \mathbf{F}_{\sigma,y} &= \frac{\partial\sigma}{\partial y}\mathbf{y} \end{aligned} \tag{3.5}$$

where $\mathbf{x}$ and $\mathbf{y}$ are together with $\mathbf{n}$ orthogonal unit vectors at the free-surface,

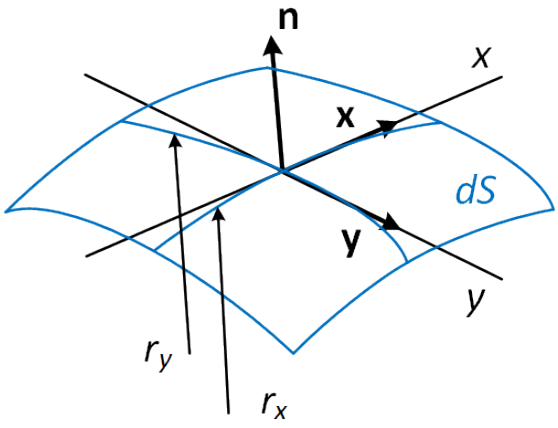

Figure 3.2: Interface between two immiscible fluids

diminish assuming the surface tension coefficient is constant.

The surface curvature κ is then defined as

$$\kappa = \frac{1}{r_x} + \frac{1}{r_y} \tag{3.6}$$

with r_x and r_y denoting the radii of curvature of the free-surface.

In the case of the front-tracking method, the surface tension force is applied as a part of boundary conditions at the boundaries of sub-domains. Considering that the interface of the front-tracking method is well defined, the surface curvature κ can be evaluated based on the boundary geometry.

The challenging problem emerges in the case of the front-capturing method. Because both fluids are modelled as an effective continuum in a single domain, the surface tension effects have to be realised by a body force that is modelled as a continuous function of the volume fraction α, so called Continuum Surface Force (CSF) model.

The free-surface normal vector $\mathbf{n}$ is then evaluated using the smooth volume fraction α

$$\mathbf{n} = \nabla\alpha \tag{3.7}$$

The gradient of the volume fraction α has a zero value everywhere but the interface.

The surface curvature κ can than be expressed as a divergence of the unit normal vector

$$\kappa = -\nabla\bullet\left(\frac{\mathbf{n}}{\|\mathbf{n}\|}\right) \tag{3.8}$$

Substituting the free-surface normal vector $\mathbf{n}$ and the surface curvature κ into the

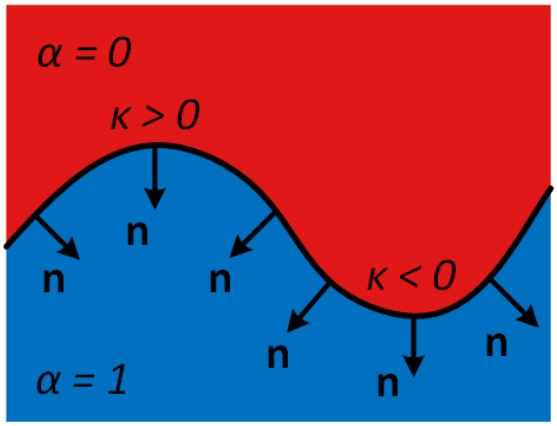

Figure 3.3: Front-capturing interface and curvature κ

surface tension definition 3.4 yields the CSF model of surface tension

$$\mathbf{F}_\sigma = -\sigma \left[\nabla \bullet \left(\frac{\nabla \alpha}{\|\nabla \alpha\|} \right) \right] \nabla \alpha \tag{3.9}$$

where the surface tension coefficient σ is assumed constant.

3.2 VoF-Method

Due to complex wave patterns that can easily develop in the case of the thin films the front-tracking method are generally less appealing as the tracking of the sharp phase interface becomes very expensive. A droplet formation at the disc edge can be closed out of the simulation in order to keep the amount of phase domains under control. However it is unsure if the droplets are being formed in the inlet area especially in the case of an impinging jet. Therefore it seems natural to use some of the front capturing techniques with an effective continuum model, for example VoF method.

The VoF-method for two-phase flows uses the volume fraction α as a phase marker

$$\alpha(t, \mathbf{x}) = \begin{cases} 0 < \alpha < 1 & \text{two-phase flow} \\ 0 & \text{first phase} \\ 1 & \text{second phase} \end{cases} \tag{3.10}$$

The volume fraction α is being transported along the flow by an advection equation

$$\frac{\partial \alpha}{\partial t} + \nabla \bullet (\alpha \mathbf{u}) = 0 \tag{3.11}$$

To avoid the smearing of the free-surface interface, the transport equation has to be solved with as little diffusion as possible. Thus the key part of the VoF method

is the discretisation scheme used for the advective term.

Generally speaking, there are three categories of treatment of the advection discretisation–donor-acceptor formulations, higher order differencing schemes and line techniques.

The donor-acceptor scheme was introduced by Hirt and Nichols[46] and is based on two main characteristics of the volume fraction marker–its boundedness and availability criterion. The boundedness keeps the value of the volume fraction α in the interval $\langle 0, 1\rangle$. The availability criterion controls the amount of the fluid convected across the control volume surface into acceptor cell is less or equal to amount that is available in the neighbouring donor cells.

The higher order differencing schemes are usually either pure higher order or blended differencing schemes and their design is usually based on the Normalised Variable Diagram (NVD) diagram by Leonard[62]. Notable schemes are Compressive Interface Capturing Scheme for Arbitrary Meshes (CISCAM) by Ubbink and Issa[103], High Resolution Interface Capturing (HRIC) by Muzaferija et al.[70] and Quadratic Upwind Interpolation for Convective Kinematics (QUICK) by Leonard[61], all implemented in ANSYS Fluent software, and especially Inter-Gamma differencing scheme by Jasak and Weller[49] that is implemented in OpenFOAM® and is used in all following VoF-simulations of the thesis[2].

The VoF discretisation schemes behaviour can be described with a help of NVD, see the figure 3.4. The normalised variables of NVD diagram are defined as

$$\begin{aligned} \tilde{\phi}_f &= \frac{\phi_f - \phi_U}{\phi_A - \phi_U} \\ \tilde{\phi}_D &= \frac{\phi_D - \phi_U}{\phi_A - \phi_U} \end{aligned} \tag{3.12}$$

where ϕ_U, ϕ_D and ϕ_A are property values in upwind, donor and acceptor cells respectively and ϕ_f is the property face value between donor and acceptor cell. The boundedness criterion is represented by the shaded area in the diagram.

The downwind differencing used in the blended differencing schemes ensures a compressive behaviour. In other words it makes the phase interface sharper. The upwind differencing scheme is diffusive and smears the interface but ensures the boundedness.

The line techniques determine the fluid distribution in a cell by using the volume fraction distribution of neighbouring cells thus avoiding the tracking of the interface in the single cell explicitly. Usually relatively simple geometric methods are used in the interface reconstruction. One of the most used is Piecewise Linear

[2]Comparisons of ANSYS Fluent and OpenFOAM® blended differencing schemes conducted by Prieling et al.[83] shows nearly identical behaviour for the investigated thin films. The differences stand out first in specific situations like dispersed flows as reported, for example, by Waclawczyk and Koronowicz[111].

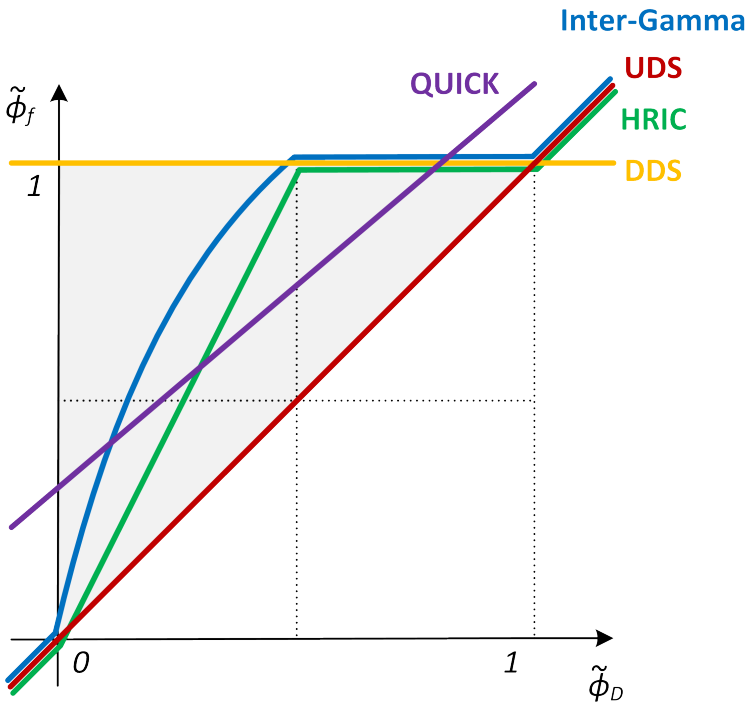

Figure 3.4: NVD diagram of the selected VoF-schemes: HRIC, QUICK, Inter-Gamma, Upwind Differencing Scheme (UDS) and Downwind Differencing Scheme (DDS)

Interface Calculation (PLIC) by Youngs[28].

The surface tension effects are usually implemented using the CSF model.

3.3 Disc with Collar

The first series of numerical investigations was based on the experimental works by Thomas et al.[101] and Ozar et al.[76]. Both conducted thin film measurement on a stationary and rotating disc with a radially injected liquid through a co-rotating collar. The collar was used to regulate the film height at the inlet. While different measurement methods were used, a capacitance sensor and a laser light reflection, the experiments used very similar same setup, see figure 3.5.

Both experiments had the same disc radius $r = 203\text{mm}$ and the collar, or the inlet, radius of $r_{\text{inlet}} = 50.8\text{mm}$.

Differences were hidden in the collar height and the fluid used. The collar height of $h_{\text{inlet}} = 0.267\text{mm}$ and water with the viscosity $\nu = 1 \times 10^{-6}\text{m}^2\,\text{s}^{-1}$ was used in the case of Thomas et al. The collar height was set to one inch, that is $h_{\text{inlet}} = 0.254\text{mm}$, and deionised water with the viscosity $\nu = 0.66 \times 10^{-6}\text{m}^2\,\text{s}^{-1}$ was used by Ozar et al.

Rotation speeds in both experiments varied from $\omega = 0\text{rpm}$ to $\omega = 300\text{rpm}$ and

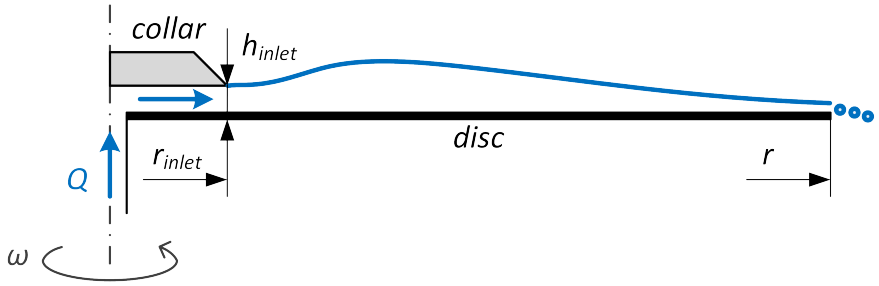

Figure 3.5: Disc with collar: $r_{\text{inlet}} = 50.8\text{mm}$, $r = 203\text{mm}$; ω, Q and h_{inlet} vary between experiments

Case	h_{inlet} [mm]	ν [$\text{m}^2\,\text{s}^{-1}$]	Q [lpm]	Re [-]	ω [rpm]
1a	0.267	1×10^{-6}	7	366	0
1b	0.254	0.66×10^{-6}	3	238	200
1c			7	555	
1d	0.254	0.66×10^{-6}	3	238	0
1e			7	555	

Table 3.1: Case definitions for the disc with collar

flow rates from $Q = 3\text{lpm}$ to $Q = 15\text{lpm}$.

The Reynolds number for the given setup is defined based on the flow rate and the inlet radius of the collar as

$$\text{Re} = \frac{Q}{2\pi\nu r_{\text{inlet}}} \tag{3.13}$$

and the maximum achieved value was $\text{Re} = 1187$ indicating laminar flow regime.

There were selected three basic simulation cases, see the table 3.1, for numerical investigations. The case 1a is a stationary case with a pronounced hydraulic jump. The case 1b is a rotating disc case that develops distinct spiral waves. The case 1c has the same rotational speed as the case 1b and an increased flow rate.

Additional two stationary cases in the given disc-collar setup, the cases 1d and 1e, were added for demonstrations of the hydraulic jump.

3.3.1 2D Axisymmetric VoF-Simulations

Two-dimensional simulations conducted in OpenFOAM® are always using a three-dimensional mesh that is just one row thick in the reduced dimension. As the mesh for the axisymmetric simulations has a very simple topology, an OpenFOAM® `blockMesh` utility was used for its creation. The resulting intermediate mesh was transformed into a 5° wedge using a `makeAxialMesh` utility. The mesh contains only 8550 cells and features simple cell grading toward the patch representing the

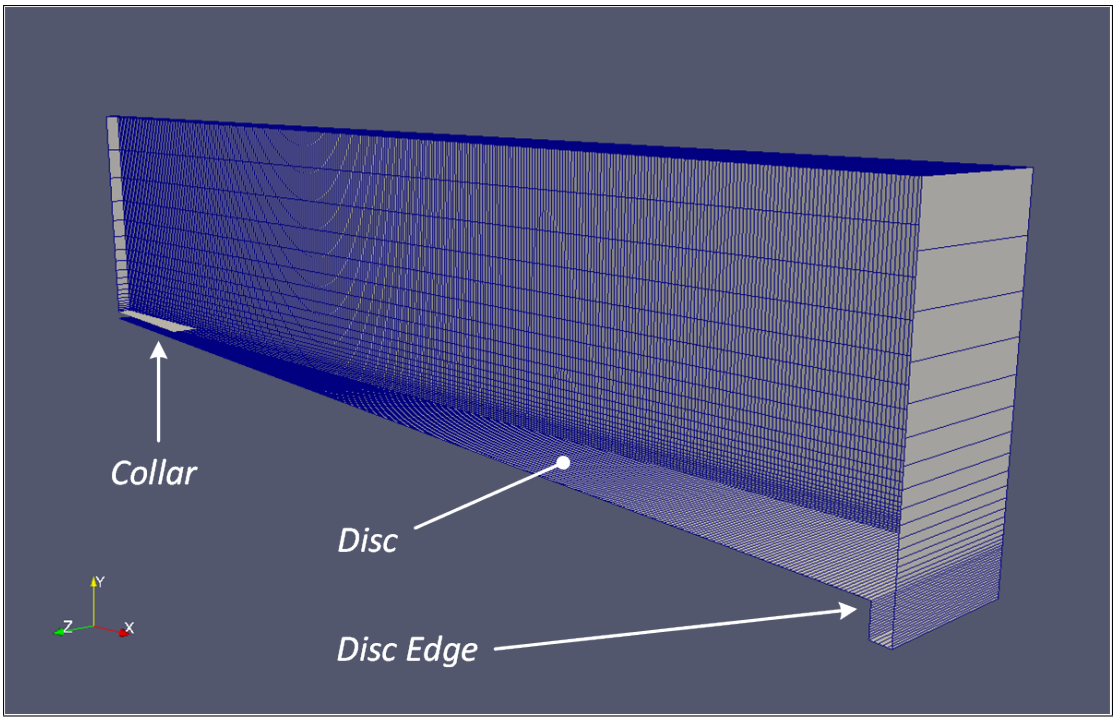

Figure 3.6: 2D axisymmetric mesh for the disc with collar: y-axis scaled 5×, internal mesh cells hidden

disc, see figure 3.6.

The OpenFOAM® solver selected for the 2D axisymmetric VoF-simulations was a stock solver `interFoam` from the OpenFOAM® distribution foam-1.6-extend[75]. The solver `interFoam` is a multi-phase solver for two incompressible isothermal immiscible fluids using the VoF-method with the higher order differencing Inter-Gamma scheme. The `interFoam` supports generic turbulence modelling that unifies solver code for both laminar and turbulent flows.

The first case, the case 1a, is a stationary case with a significantly developed hydraulic jump. The 2D axisymmetric VoF-simulation, see figure 3.7, predicts the hydraulic jump fairly well. The mean film height measurement conducted by Thomas et al. compared with the instantaneous film height from the simulation shows a very good prediction of the hydraulic jump onset around radius of 100mm. The height of the hydraulic jump is underpredicted by approximately 1mm.

The second simulation, the case 1b, has a rotating disc with velocity 200rpm and the volumetric flow rate of 3lpm. The simulated flow on the disc does not form a visible hydraulic jump due to the stronger centrifugal forces. Instead the thin film tearing is observed in the 2D axisymmetric simulation, see figure 3.8. Torn off film elements are then transported away toward the disc outer edge. Comparisons of the instantaneous from the VoF-simulation and the measurements by Ozar et al. shows that film height is overpredicted especially in the collar vicinity.

The last simulation is essentially the same setup as the previous case showing

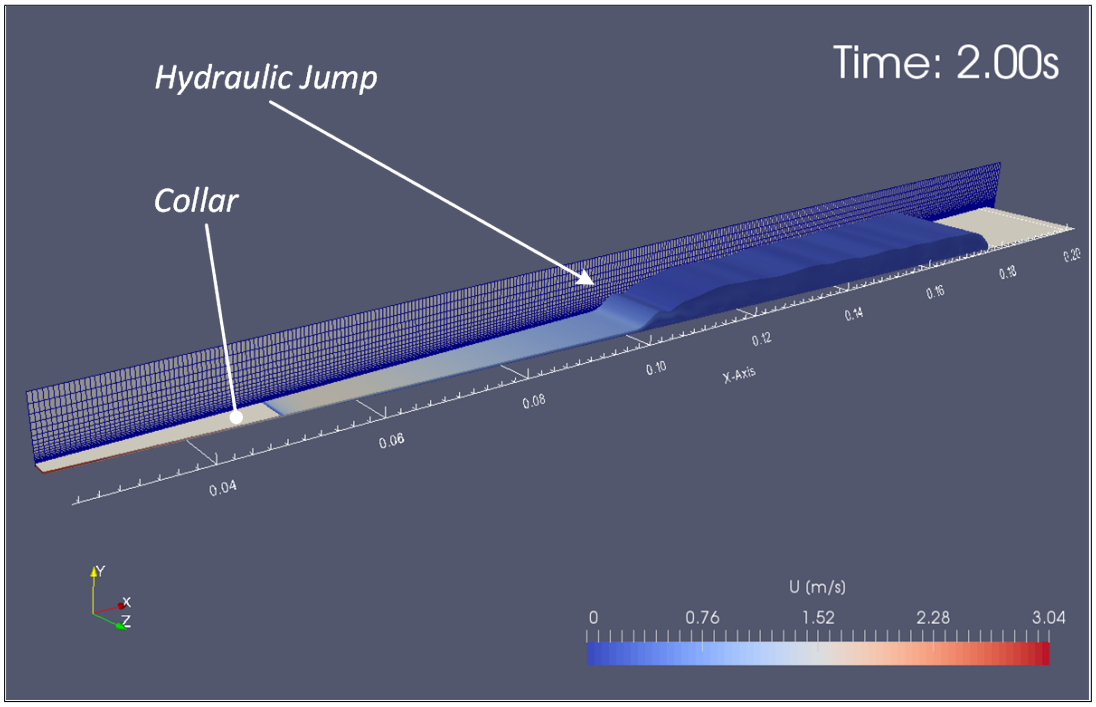

(a) 2D axisymmetric VoF-simulation

Film height at $t = 2$s

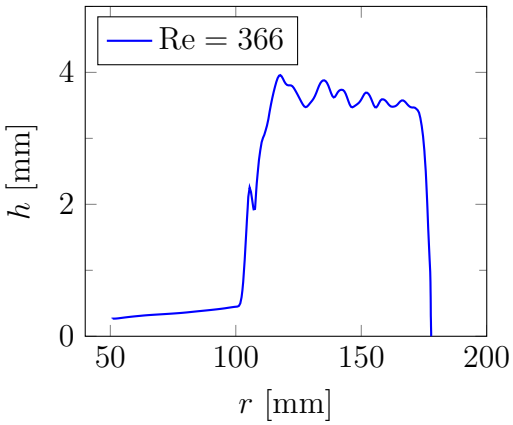

(b) Instantaneous film height

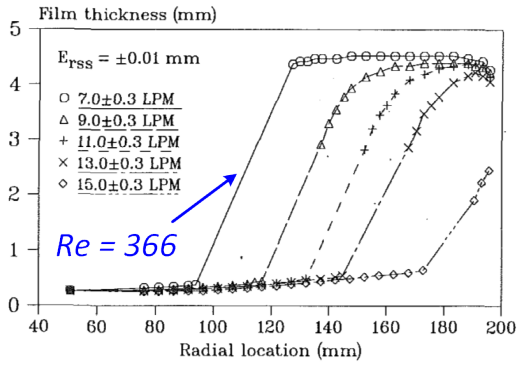

(c) Mean film height by Thomas et al.[101]

Figure 3.7: Case 1a (2D VoF): $Q = 7$lpm ($Re = 366$), $\omega = 0$rpm

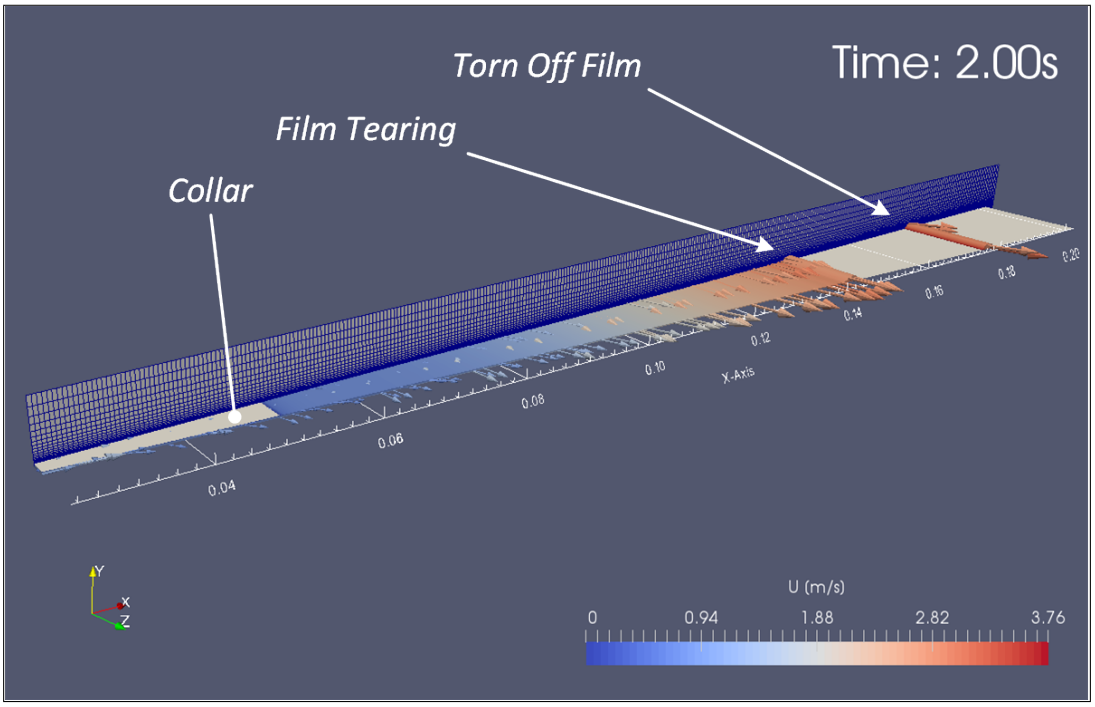

(a) 2D axisymmetric VoF-simulation

Film height at $t = 2$s

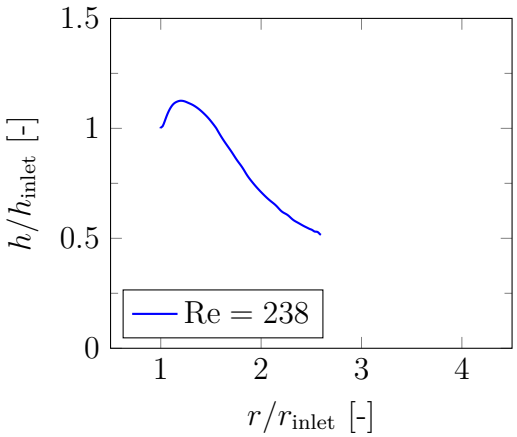

(b) Instantaneous film height

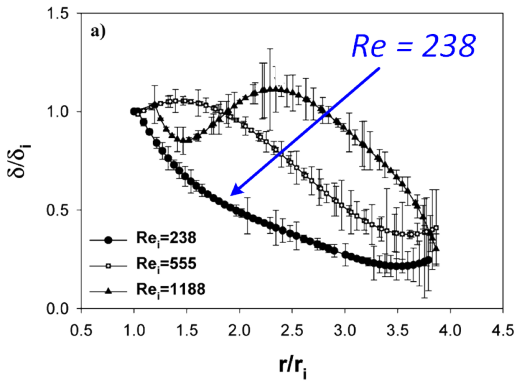

(c) Mean film height by Ozar et al.[76]

Figure 3.8: Case 1b (2D VoF): $Q = 3$lpm ($Re = 238$), $\omega = 200$rpm

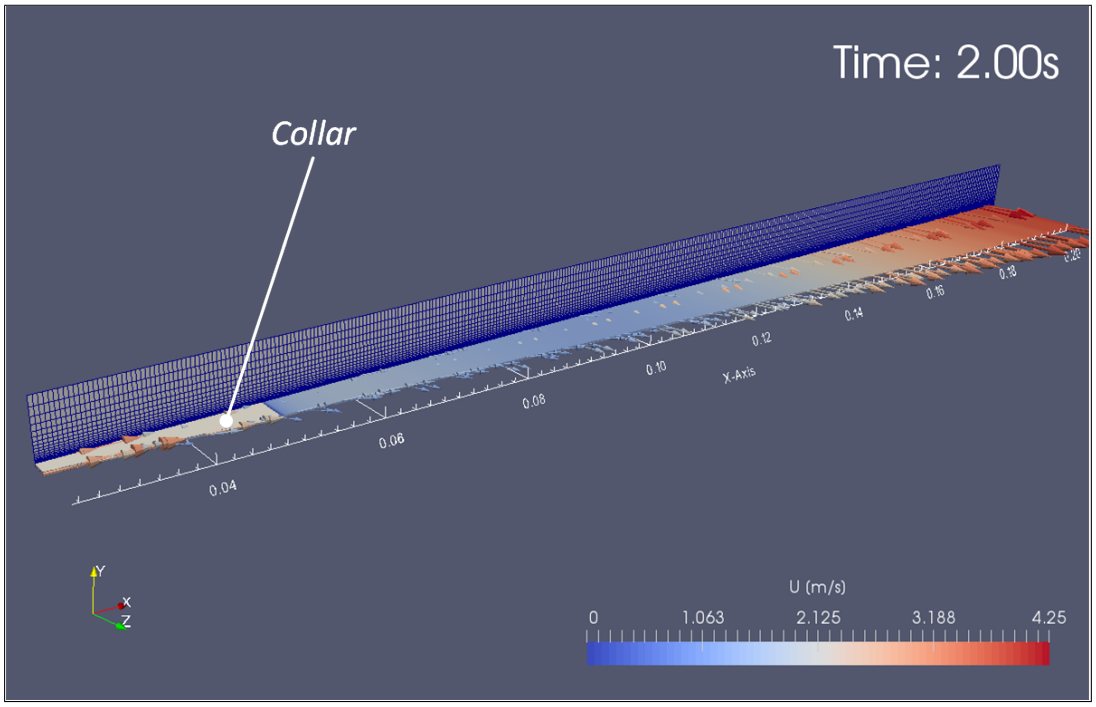

(a) 2D axisymmetric VoF-simulation

Film height at $t = 2$s

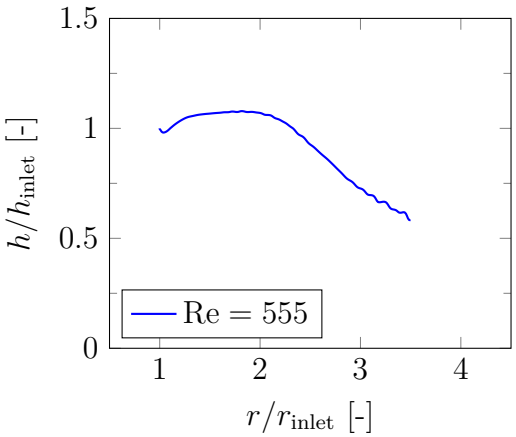

(b) Instantaneous film height

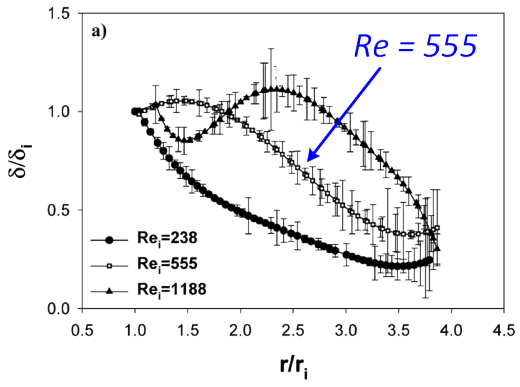

(c) Mean film height by Ozar et al.[76]

Figure 3.9: Case 1c (2D VoF): $Q = 7$lpm ($Re = 555$), $\omega = 200$rpm

the film discontinuity. However, in the case 1c the inlet flow rate is increased to 7lpm what leads to continuous wetting of the disc, see figure 3.9. Surface waves become more pronounced with increased Reynolds number and are demonstrated in not so smooth instantaneous film height curve especially in the zone close to the disc outside edge. The comparison with the experiment conducted by Ozar et al. shows a slight overprediction. The general trend of the film height is very well predicted and matches measurement from the experiment.

First interesting phenomena presented in the previous simulations was the hydraulic jump. The hydraulic jump is especially visible at the stationary cases where the film inertial forces are dominant. Generally the centrifugal forces thin the film out and push the hydraulic jump toward the outer edges. The hydraulic jump can be observed at very low rotational speeds as well; however, it is not as pronounced as in the stationary cases and with higher Reynolds numbers turns into increased surface waviness.

In order to demonstrate the onset of the hydraulic jump, two additional simulation cases–the case 1d and 1e–have been defined. The cases have lower and higher Reynolds number as the case 1a. The lower Reynolds number of 238 is then connected to the very early onset of the hydraulic jump, while the higher Reynolds number of 555 delays the hydraulic jump appearance. The high-velocity photographs taken by Ozar et al. correspond nicely with the results of the 2D axisymmetric simulation, see fig 3.11.

The second finding, the film tearing, is very interesting and led to further investigations concerning an influence of a surface tension σ and a contact angle θ on the disc wetting. It shows up that both, the surface tension and the contact angle, have an influence on the disc coverage with the fluid film and on the shape of the frontal wave especially during the disc flooding at the start. Once the disc is covered with the film the influence is usually merely visible at the disc outer areas. An open question exists regarding the transport of the teared off film elements.

It turns out that the behaviour of the film discontinuity in the case 1b is actually a projection of a spiral wave pattern, see figure 3.10, into the 2D axisymmetric simulation. The torn off film elements, the parts of spiral waves, are influenced by the contact angel and surface tension. The conservative contact angle[3] of 90° that was used in the simulation due to the lack of data[4] leads to the discontinuity of the fluid film at the spiral wave front.

The demonstration of the spiral wave pattern can be considered a weak spot of the 2D simulation as it is next to impossible to recognise wave patterns based

[3]Strong *hydrophilic* surfaces have the contact angle from 0° to 30°. *Hydrophobic*, fluid repelling, surfaces have the contact angle higher as 90°. The contact angles from 30° to 90° are associated with lesser hydrophobic surfaces.

[4]An approximate contact angle for aluminium surfaces reported by Gajewski[37] is 80°. However the given value was not measured exactly.

purely on the simulation results itself. Furthermore, a limitation of the central impingement, be it by means of the co-rotating collar or an impinging jet, due to symmetry has to be mentioned.

3.3.2 3D VoF-Simulations

The deficiency of 2D simulations to properly describe wave patterns and being bound to the central impingement naturally leads to 3D investigations. The case 1b was chosen for the 3D VoF-simulations because of its pronounced spiral waves.

The original 2D mesh, see figure 3.6, has been protruded into 3D mesh and reduced by cutting of the area behind the disc edge in the original 2D mesh. The first experiments imposed a new limitation on the mesh, a maximal cell aspect ratio. It was found that 3D simulation is very sensitive on the mesh resolution and the cell height-to-length ratio has to be 1-to-4 at the most. Higher cell aspect ratios introduce simulation artifacts which lead to crashes.

In order to improve the grid resolution while saving on the amount of the cells, a different solver was used. 3D VoF-simulations were conducted with a stock solver `interDyMFoam` from the OpenFOAM® distribution foam-1.6-extend[75]. The `interDyMFoam` solver, as its name suggests, is a special variation of the originally used `interFoam` solver with an added feature of an adaptive dynamic mesh refinement.

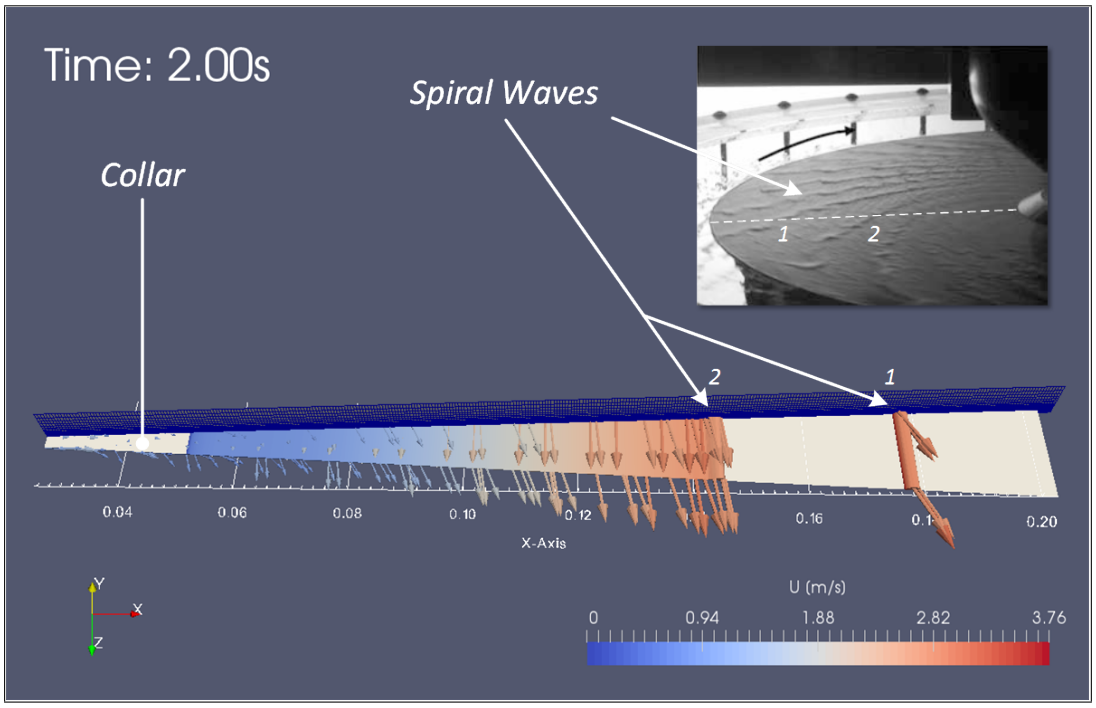

(a) Case 1b (2D VoF): Q = 3lpm (Re = 238), ω = 200rpm; photograph courtesy of Ozar et al.[76]

Figure 3.10: Spiral waves in the 2D axisymmetric VoF-simulation

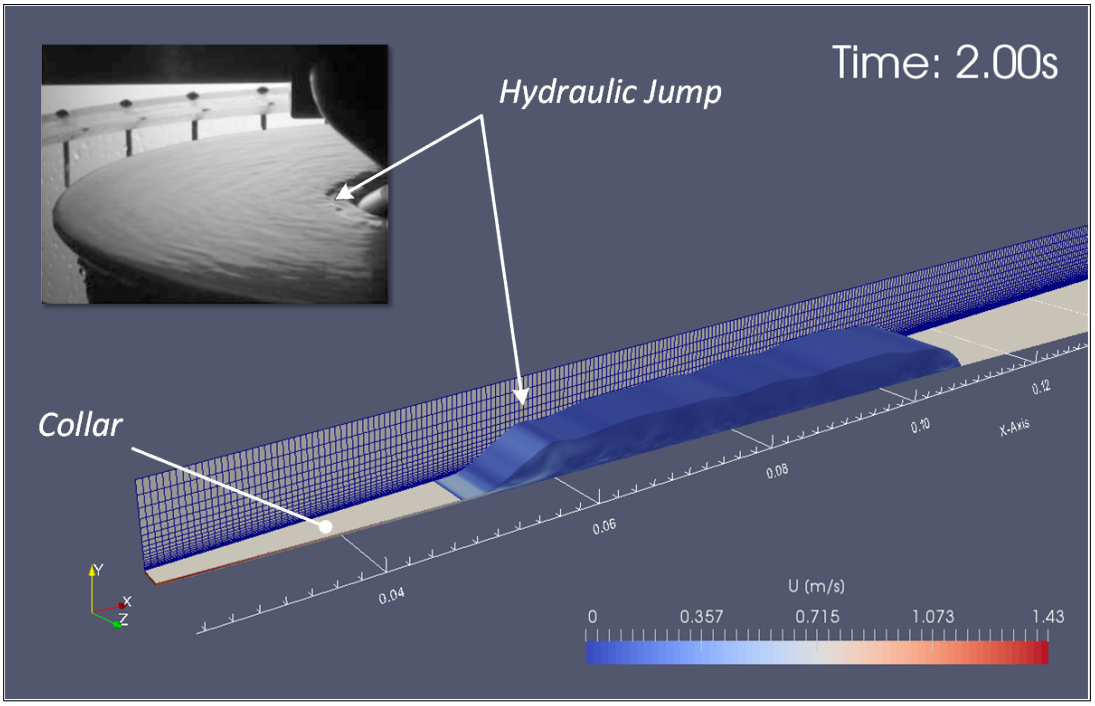

(a) Case 1d (2D VoF): $Q = 3$lpm ($Re = 238$), $\omega = 0$rpm; photograph courtesy of Ozar et al.[76]

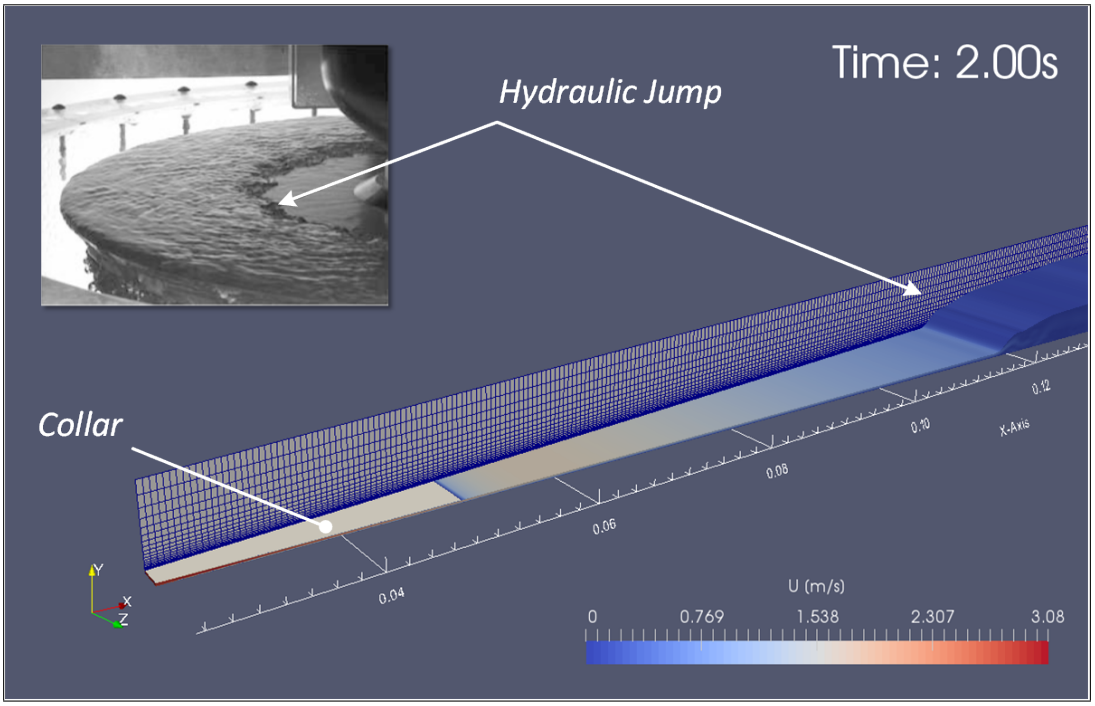

(b) Case 1e (2D VoF): $Q = 7$lpm ($Re = 555$), $\omega = 0$rpm; photograph courtesy of Ozar et al.[76]

Figure 3.11: Hydraulic jump in the 2D axisymmetric VoF-simulation

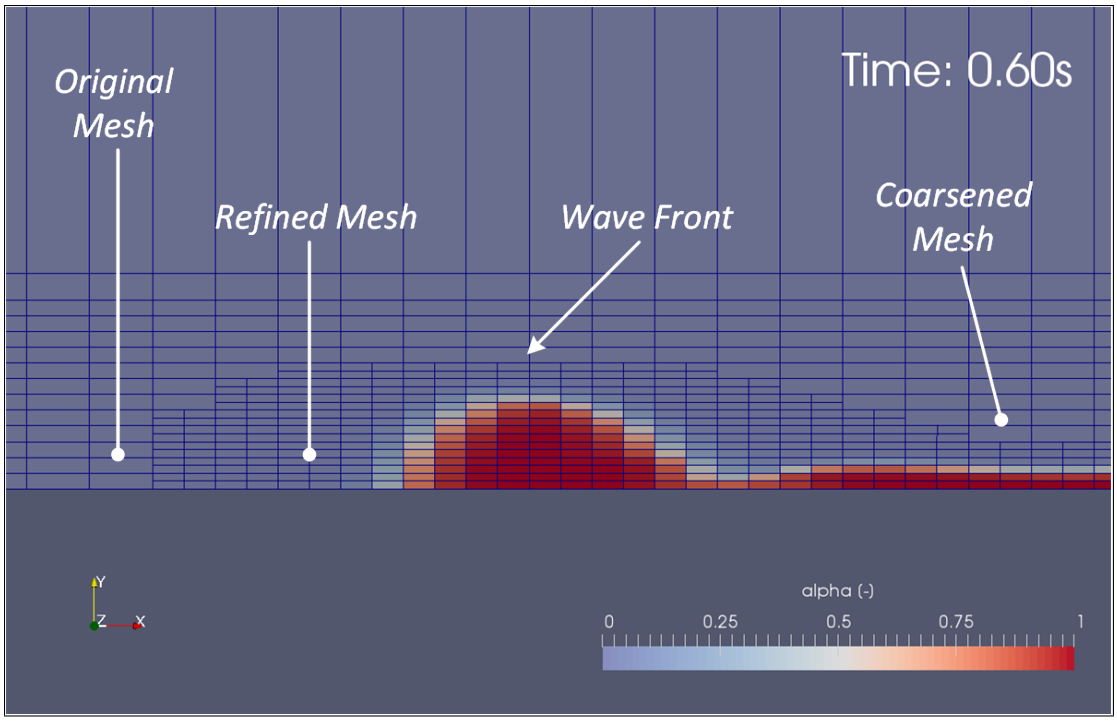

Figure 3.12: Dynamic mesh refinement: Wave front passing the mesh on a processor domain border

The adaptive mesh refinement adds an on-fly refinement of the mesh by recursive splitting of the cells in the area of the captured phase interface. The solver as well coarsens previously refined cells in the single phase areas up to the original mesh resolution. The illustration of the refinement technique can be seen on the figure 3.12 that presents the fluid frontal wave passing through the mesh.

The advantage of the technique is having a relatively coarse computational mesh at the start with an automatic increase of the amount of cells only where it is needed. The disadvantage is an additional computational overhead of the mesh manipulation. However, as long as the mesh manipulation takes less resources as the solution on the static mesh with a higher resolution, the adaptive mesh refinement is the technique of choice.

The original coarse 3D mesh had approximately 320 000 cells at start. The mesh refinement has to be strictly controlled as the splitting of the cell in half along all axes leads to 8 new cells. The amount of cells is heavily dependent on the flow behaviour during the simulation and varied, depending on the contact angle θ, from approximately 710 000 to 968 000 cells at 0.6s during the disc flooding in the case 1b.

The 3D simulation of the case 1b confirmed the observations from the 2D axisymmetric simulation. The spiral wave pattern develops and even the lesser hydrophobic contact angle 75° still causes the tearing of the film, see figure 3.13a. Changing the contact angle to the hydrophilic value of 10° shows that the tearing

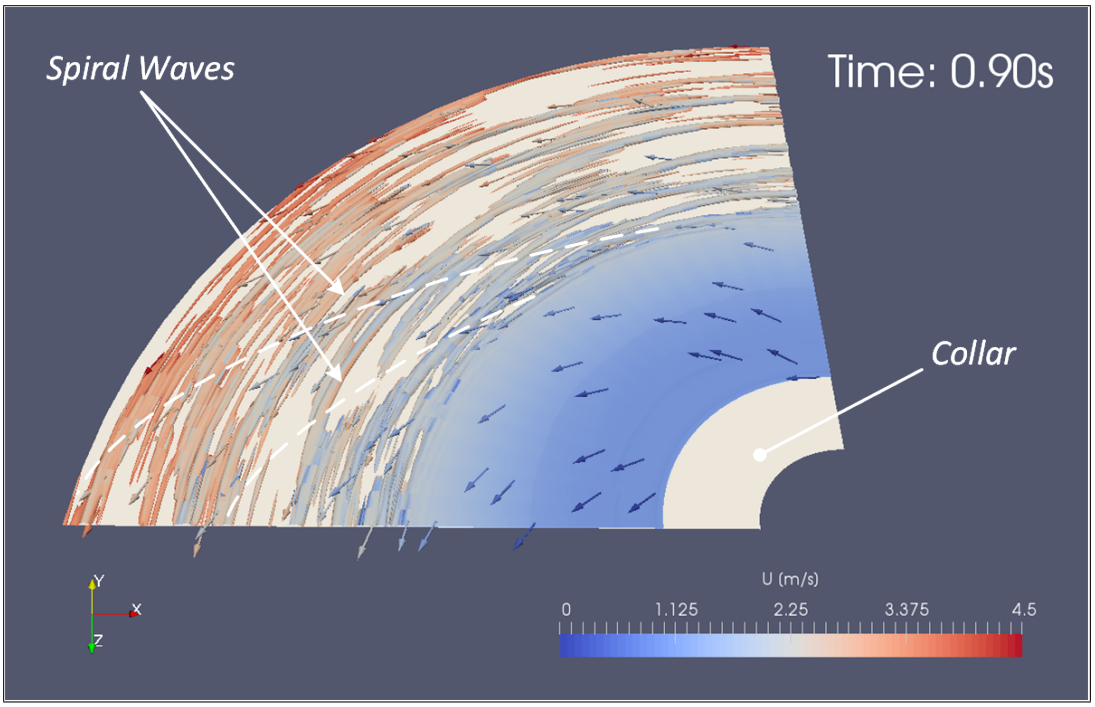

(a) Contours of fluid velocity ($\theta = 75°$): Single processor domain

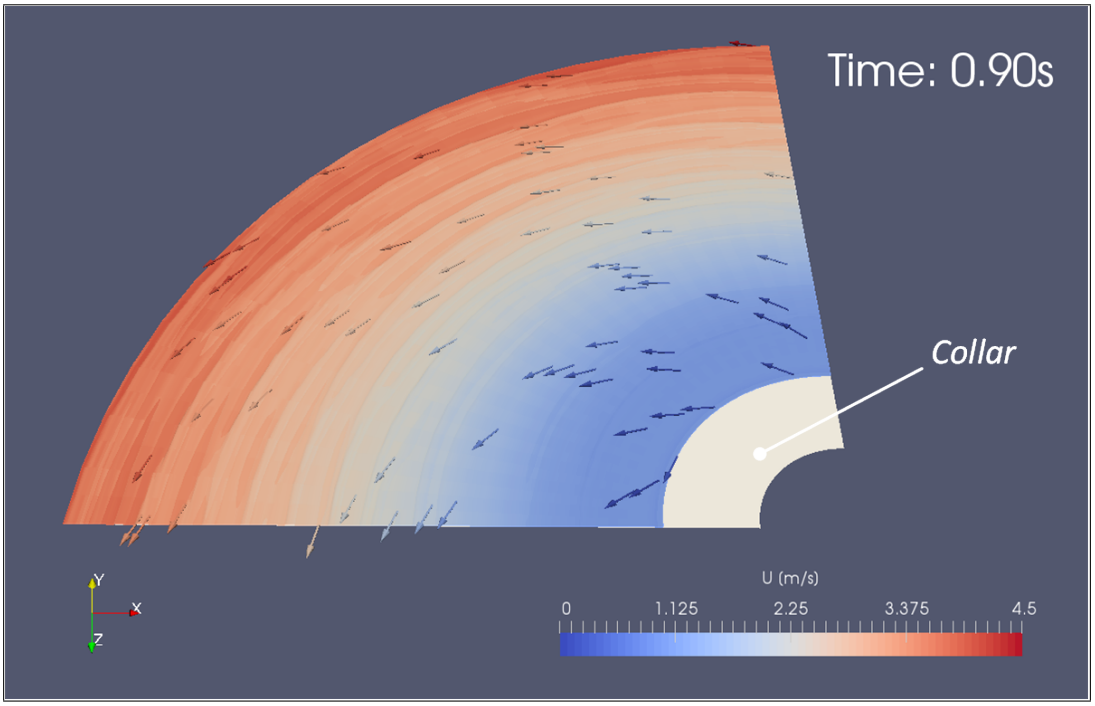

(b) Contours of fluid velocity ($\theta = 10°$): Single processor domain

Figure 3.13: Case 1b (3D VoF): $Q = 3$lpm ($Re = 238$), $\omega = 200$rpm

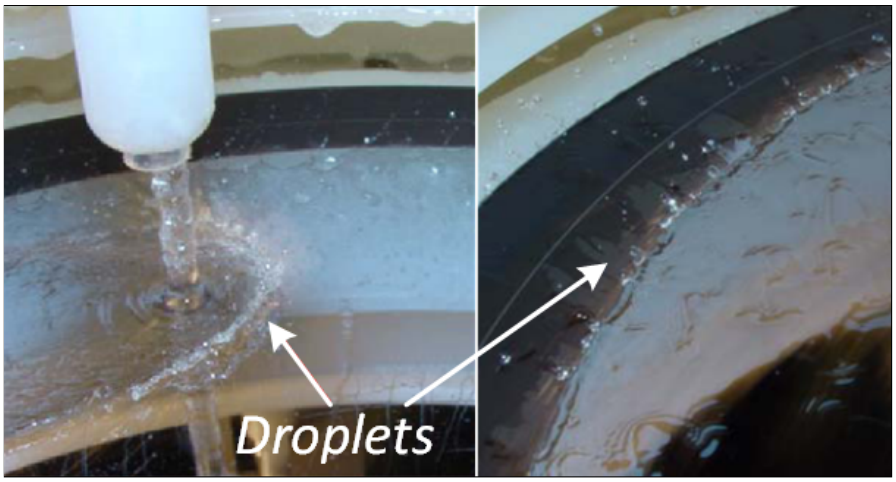

Figure 3.14: Droplets forming: Excentric impinging jet and the disc edge area; photographs courtesy of TU Graz

is indeed caused by the interaction of the fluid with the disc surface and the whole disc is coated without discontinuities, see figure 3.13b.

Both simulations were stopped at the time 0.9s as it was not economical, from the computational point of view, to continue as the observations from the 2D axisymmetric simulations were confirmed. It is important to point out that the simulation time needed for a single 3D VoF simulation with the adaptive mesh refinement of 0.9s long process that was performed in parallel on 4 CPU cores of Intel Core i7 Bloomfield-family was 30 days.

3.4 Disc with Impinging Jet

The discussed simulation cases have used central impingement through the co-rotating collar. The collar is used to control the in-flow conditions and effectively prevents formation of the droplets. Industrial applications do not usually use a collar but an impinging jet. The impinging jet is a possible source of droplets in the inlet area. The outside disc edge is the second place where droplets are formed, see figure 3.14. Generally droplets are not welcome in the industrial applications as they are connected with disturbances in the film flow and a possible contamination of the disc surrounding area.

In order to examine the central impingement with the impinging jet a configuration close to ones used in semiconductor industry was thought out. The setup has a rotating disc of the size of 300mm wafer, see figure 3.15. The inlet nozzle of 2.15mm radius is placed 35mm above the disc centre.

A single simulation case, the case 2, was defined. The flow rate $Q = 0.3$lpm at the inlet represents a laminar flow with relatively high $Re = 1156$ compared to previous cases. The disc rotational speed is relatively low $\omega = 60$rpm. The

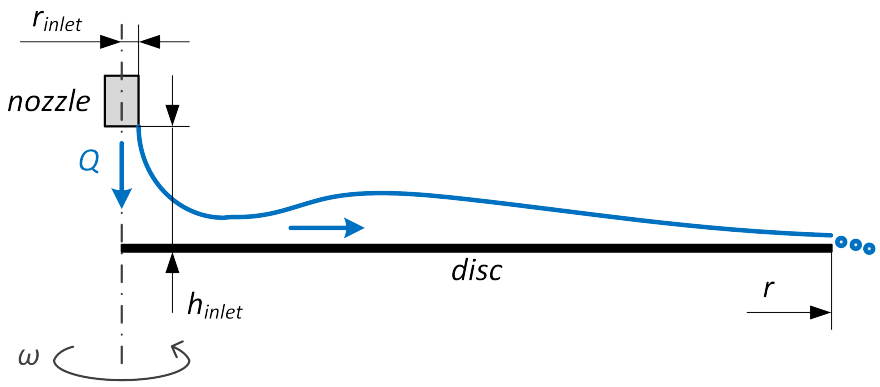

Figure 3.15: Disc with impinging jet: $r_{\text{inlet}} = 2.15\text{mm}$, $r = 150\text{mm}$, $h_{\text{inlet}} = 35\text{mm}$

simulated fluid is a water with the kinematic viscosity $\nu = 1 \times 10^{-6}\text{m}^2\,\text{s}^{-1}$. The contact angle was 30° at the disc and 90° at the inlet nozzle.

The L-shaped computational mesh, see figure 3.16, has been modelled with the Gambit pre-processor and contains approximately 71 000 cells. The mesh is graded toward the impingement area in order to increase the mesh resolution there.

The simulation had a prescribed fluid phase values in the nozzle area to maintain the numerical stability. For the given parameters 2D VoF-simulation shows no droplet formation in the inlet area, see figure 3.17. This is a positive finding as the further work does not need to consider the droplets formation in the inlet area with a reasoning that proper process parameters can avoid the problem all

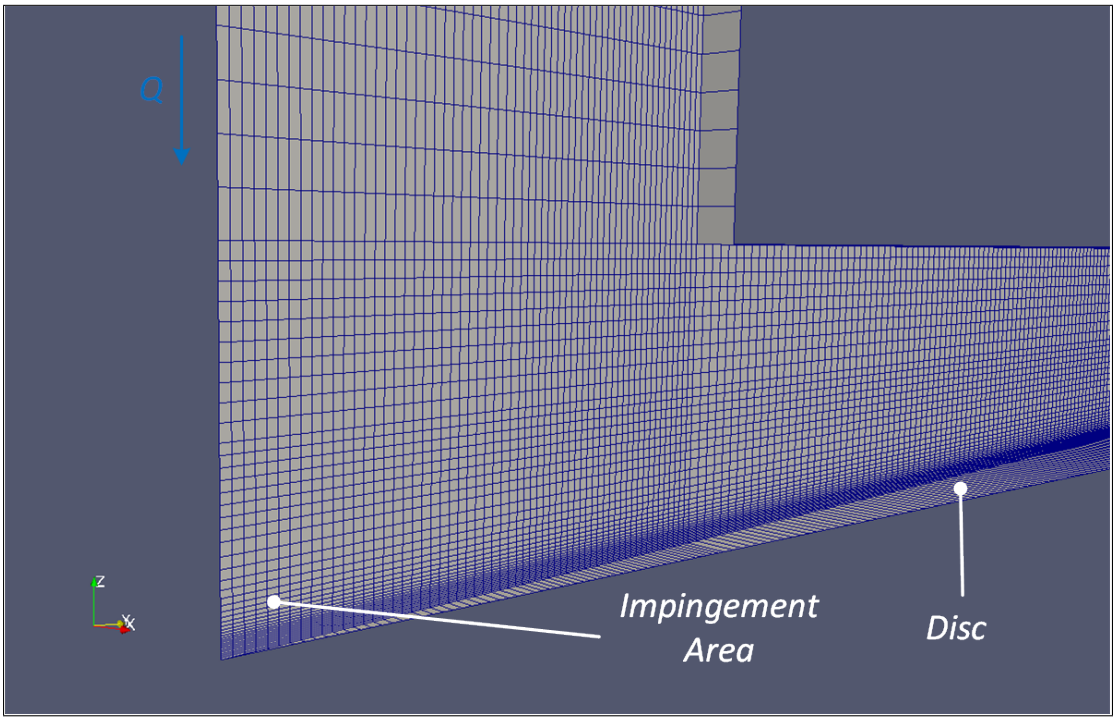

Figure 3.16: 2D axisymmetric mesh for the disc with impinging jet: y- and z-axis scaled 1.5×, internal mesh cells hidden

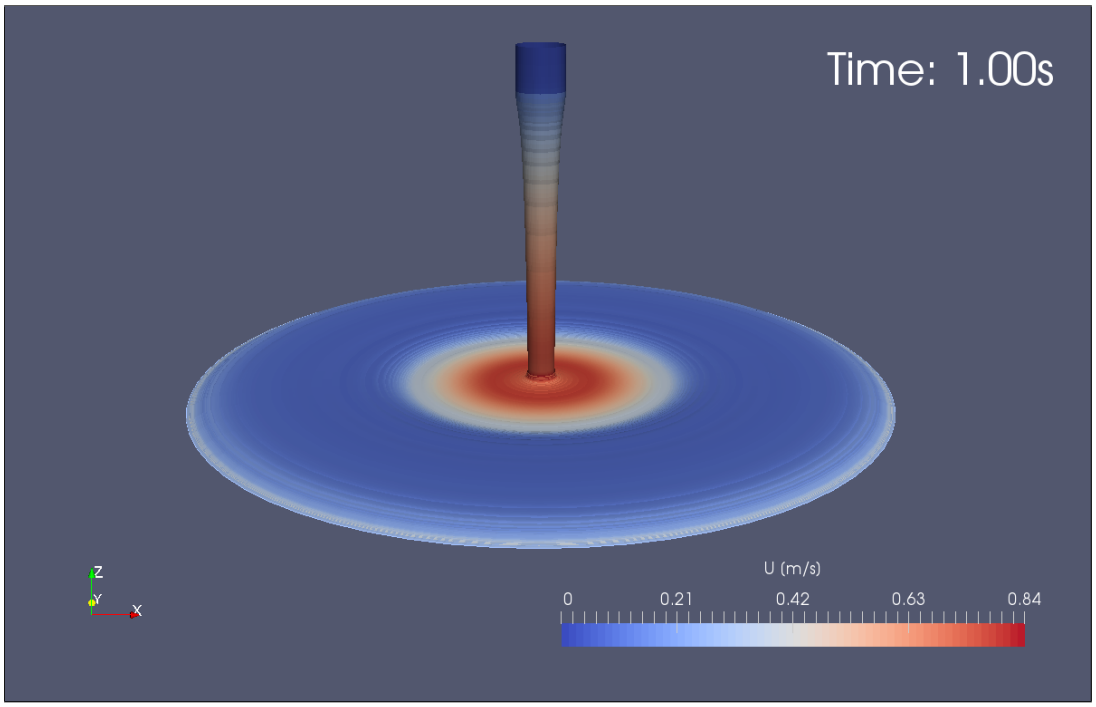

(a) Contours of fluid velocity showing the disc flooding

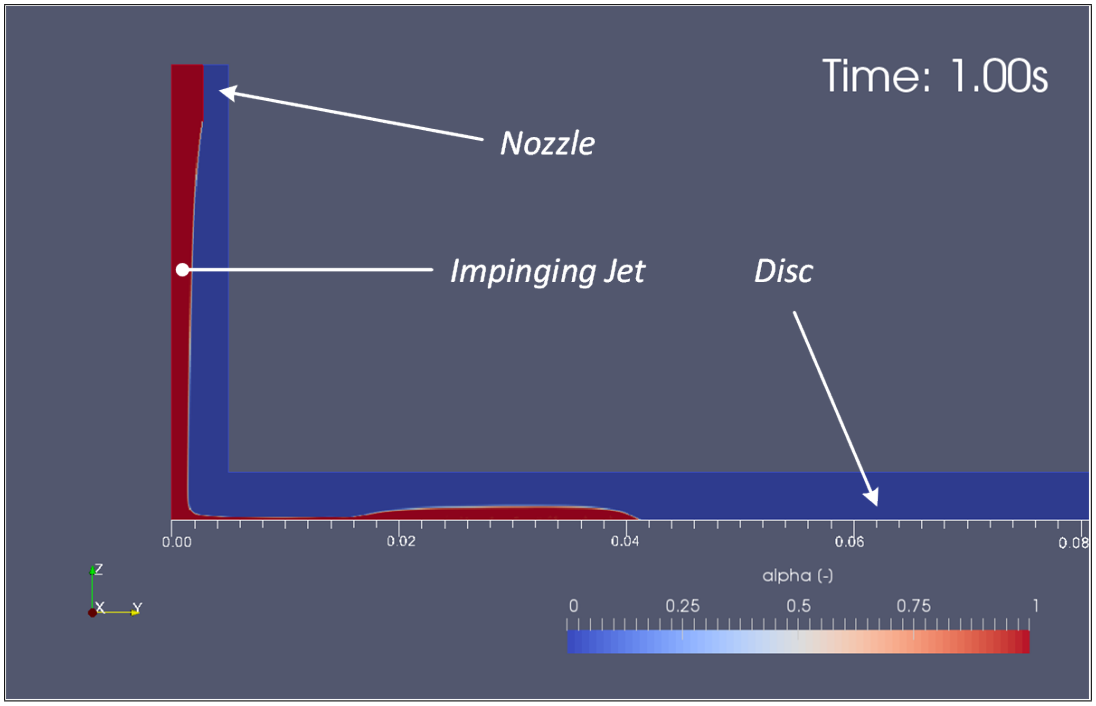

(b) Impingement in the inlet area

Figure 3.17: Case 2 (2D VoF): $Q = 0.3$lpm ($Re = 1156$), $\omega = 60$rpm

together. The fluid manages to wet barely one third of the disc in the first second of the process. The static hydraulic jump forms very close to the inlet.

3.5 Summary and Discussion

VoF-method is a popular numerical approach for solution of free-surface problems. The main appeal of the method is hidden in the lack of assumptions placed on fluid phases. Both 2D and 3D VoF-simulations are the usual first choice for investigations of fluid films on a rotating disc.

2D VoF axisymmetric simulations are especially appealing due to their relatively low computational costs. However 2D axisymmetric approach has its limitations. First of all it is suitable only for cases with the central impingement. Moreover it cannot describe complex wave patters which simply cannot be resolved in two dimensions only.

On the other side, 3D VoF simulations have no limitations placed on the problem definition. One can simulate both central or excentric impingement with easy and even complex wave patters are well captured and reproduced. However the computational costs are exponentially higher and where 2D VoF simulation needs few hours, 3D VoF simulation needs are easily in order of weeks. This renders the 3D VoF approach impractical for numerical studies of the thin films that need a very high spatial or temporal resolution.

Unfortunately as no other effective solution exists, 3D VoF method stays to be the method of choice for industrial applications simply out of necessity. This highlights a clear need for an alternative numerical approach to the simulation of the fluid films where both, the solution accuracy and the simulation computational costs, are in the focus.

Chapter 4

Thin Film Model

The previous chapter presented the 2D and 3D VoF numerical investigations of the film flow on the rotating disc. The VoF simulations showed the computational complexity of the free-surface simulation and highlighted the need for a different approach. There are generally two ways. Either more computational power, a brute force approach, or an alternative technique, a clever solution, has to be sought. Characteristics of the thin film allow a reduction of the problem dimensionality and the derivation of the resulting thin film model is given in this chapter.

4.1 Modelling Assumptions

The fluid film on the rotating disc has some characteristics that can be exploited:

- The fluid film is primarily driven by centrifugal and shear forces that define a dominant velocity component in the tangential direction while the velocity component in the normal direction, a cross flow, can be neglected

$$\mathbf{u} = (u, v, w), w \to 0 \tag{4.1}$$

- The film thickness is very small, in the order of tenth of millimetres with extremes only in the order of millimetres. Therefore pressure like in a boundary layer can be assumed constant across the film.

These two main characteristics, the non-existent cross flow and the constant pressure across the film thickness, open a way for a transformation of the three-dimensional problem into a two-dimensional one by averaging over the film height, that is by integrating the Navier-Stokes equations across the film height.

The thin film height tends to be similar to a boundary layer thickness especially in areas with strong centrifugal forces. The same idea of reducing of the dimension

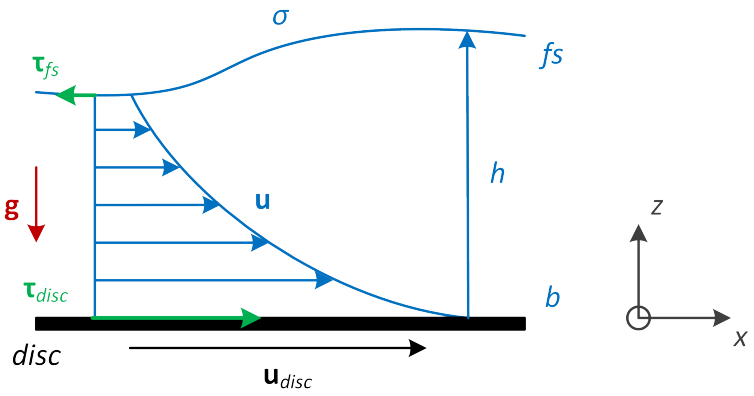

Figure 4.1: Thin film characteristics

is hidden behind many other techniques connected to modelling of boundary layer and thin films, for example Integral Boundary Layer (IBL) model[95]. Even the shallow water (SW) equations[110] are exploiting the disproportion in the vertical scaling and use the integration across the water depth.

Additional assumptions and demands are defined specifically for the thin film cases under consideration:

- The flow is assumed to be laminar[1].
- Velocity profiles across the film height in the vertical direction can be approximated by polynomial expressions.
- Inertial forces cannot be neglected.
- The interface friction between air and liquid at the film free-surface *fs* can be neglected

$$\tau_{fs} \to 0 \tag{4.2}$$

- Surface tension σ is an important factor for the formation of the hydraulic jump and has to be accounted for.
- The variation in the temperature across the film thickness is small but the temperature is not constant.
- The fluid is assumed to be Newtonian.
- The liquid forming the thin film is incompressible and due to small variations in the temperature across the film thickness the density across the film height is assumed constant

$$\rho = \text{const.} \tag{4.3}$$

[1]Turbulent regimes are not welcome in the wafer etching process.

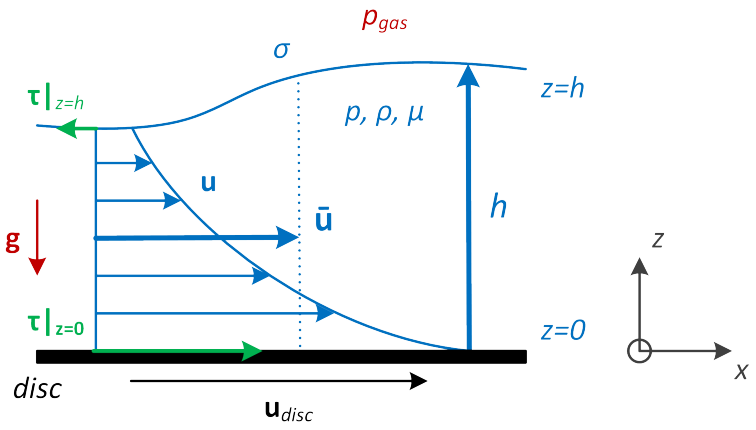

Figure 4.2: Thin film definitions

- Droplets formation is not considered. Both liquid and air are segregated with a single well defined interface.

As the main driving factor for development of the thin film model is the reduction of the computational costs, additional assumptions on the positioning of the rotating disc that simplify algebraic calculations are imposed:

- The disc itself is placed in the origin and aligned with xy-plane so that the disc normal direction is aligned with z-axis

$$\mathbf{x}_{\text{disc}} = (x, y, 0) \tag{4.4}$$
$$\mathbf{n}_{\text{disc}} = (0, 0, 1) \tag{4.5}$$

- Gravity $\mathbf{g}$ acts against the disk normal direction

$$\mathbf{g} = (0, 0, -g) \tag{4.6}$$

4.2 Definitions

4.2.1 Film Height

The thin film is enclosed at the bottom by the disc and by the free-surface between liquid and the ambient gas. There exists no flow across these two boundaries. Thus the formation of the droplets at the free-surface is not possible.

The disc placement assumptions simplify the definition of the lower boundary. Typically the bottom of the film is treated as a function that describes the bottom topology. As the disc is flat[2], placed at the origin and aligned with z-axis, the

[2]The nano-structure scales of the wafer surface are insignificant compared to the thin film height.

bottom b is described by a constant zero function

$$b = b(t, x, y) = 0 \tag{4.7}$$

The top boundary that is the free-surface fs is generally unknown and is described by a function

$$fs = fs(t, x, y) \tag{4.8}$$

The film height h that represents a new dependent variable in the thin film model is then defined as

$$h = h(t, x, y) = fs - b = fs \tag{4.9}$$

and is identical with the free-surface fs.

4.2.2 Film Velocity

The very important characteristic of the thin film is the distribution of the velocity across the film thickness. The momentum transfer across the film thickness is non-uniform and more momentum is being transported in film layers with higher velocities usually closer to the rotating disc. These differences in the momentum transport have to be carefully evaluated in order to properly capture the inertial forces in the film.

The film mean velocity $\overline{\mathbf{u}}$, the second dependent variable in the thin film model, is defined as

$$\overline{\mathbf{u}} = \frac{1}{h} \int_h \mathbf{u}\, dz \tag{4.10}$$

The averaging of the velocity across the film thickness has, however, a negative side-effect that is the loss of information in the averaged dimension. The thin film model resolves the dependent variable $\overline{\mathbf{u}}$ but it cannot resolve spatial velocity distribution. In order to overcome the problem a supporting model, a polynomial velocity profile function $\hat{\mathbf{u}}$, that mimics the velocity distribution as close as possible is introduced

$$\begin{aligned} \mathbf{u}(t, x, y, z) &= \hat{\mathbf{u}}(t, x, y, \xi) + \varepsilon_{\hat{\mathbf{u}}} \\ \hat{\mathbf{u}}(\xi) &= \mathbf{a}_0 + \mathbf{a}_1\xi + \mathbf{a}_2\xi^2 + \mathbf{a}_3\xi^3 \\ &\xi \in \langle 0, 1\rangle, z = h\xi \end{aligned} \tag{4.11}$$

where ξ is the normalised vertical coordinate and $\varepsilon_{\hat{\mathbf{u}}}$ denotes the velocity profile modelling error.

The polynomial velocity coefficients $\mathbf{a}_i$ are determined by a set of the boundary conditions:

- Relation to the mean velocity

$$\int_0^1 \hat{\mathbf{u}}(\xi)\, d\xi = \overline{\mathbf{u}} \tag{4.12}$$

- No slip boundary condition at the disc that drives the film acceleration

$$\hat{\mathbf{u}}(\xi)|_{\xi=0} = \mathbf{u}_{\text{disc}} \tag{4.13}$$

- Von Neumann boundary condition at the film free-surface

$$\left.\frac{\partial \hat{\mathbf{u}}(\xi)}{\partial \xi}\right|_{\xi=1} = 0 \tag{4.14}$$

- Influence of the pressure gradient at the film bottom

$$\left.\frac{\partial^2 \hat{\mathbf{u}}(\xi)}{\partial \xi^2}\right|_{\xi=0} = 0 \tag{4.15}$$

that lead to the following solution of the velocity profile function, Appendix A.1

$$\hat{\mathbf{u}}(\xi) = \mathbf{u}_{\text{disc}} + (\overline{\mathbf{u}} - \mathbf{u}_{\text{disc}}) \left(\frac{12}{5}\xi - \frac{4}{5}\xi^3 \right) \tag{4.16}$$

The relationship between the mean film velocity $\overline{\mathbf{u}}$ and the velocity distribution across the film thickness is depicted in the figure 4.4.

In order to describe the non-uniformity in the momentum transfer in the vertical direction, the spatial velocity fluctuations $\tilde{\mathbf{u}}$ have to be introduced

$$\mathbf{u} = \overline{\mathbf{u}} + \tilde{\mathbf{u}} \tag{4.17}$$

The technique above, the Reynolds decomposition, is well known from the statistical turbulence modelling, see Section 2.5; however, here it is applied to the spatial quantity fluctuations rather as the temporal one.

The closer look on the definition of the mean film velocity

$$\begin{aligned} \overline{\mathbf{u}} &= \frac{1}{h} \int_h (\overline{\mathbf{u}} + \tilde{\mathbf{u}})\ dz \\ &= \frac{1}{h} \int_h \overline{\mathbf{u}}\, dz + \frac{1}{h} \int_h \tilde{\mathbf{u}}\, dz \end{aligned} \tag{4.18}$$

together with a realisation that the mean value is invariant to the averaging

$$\frac{1}{h} \int_h \overline{\mathbf{u}}\, dz = \overline{\mathbf{u}} \tag{4.19}$$

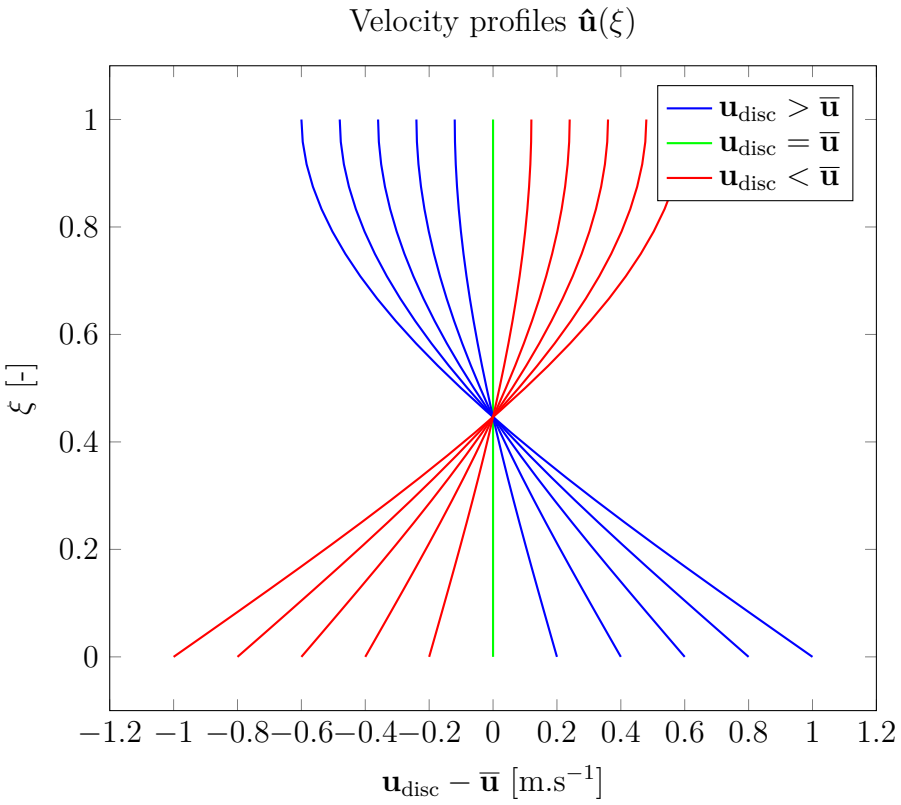

Figure 4.3: Examples of velocity profiles

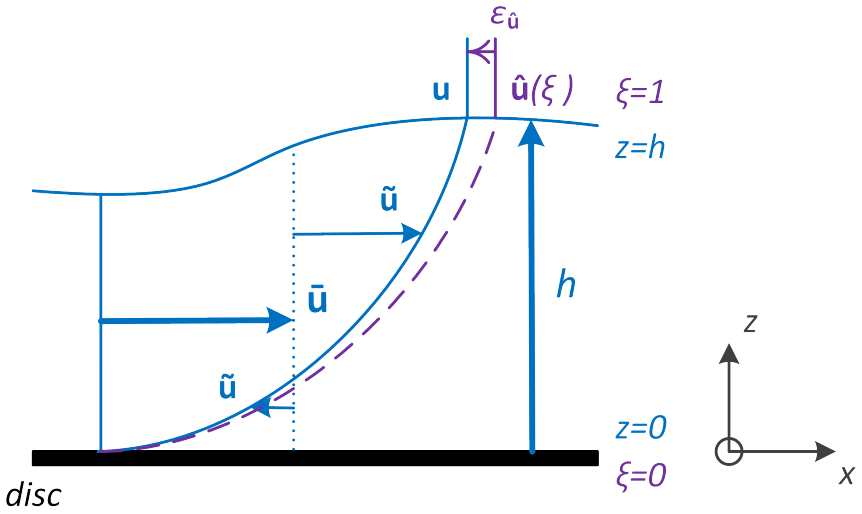

Figure 4.4: Velocity decomposition

reveals an important identity of the vertical velocity fluctuation $\tilde{\mathbf{u}}$

$$\frac{1}{h}\int_h \tilde{\mathbf{u}}\, dz = 0 \tag{4.20}$$

Finally, the generally unknown vertical velocity fluctuation $\tilde{\mathbf{u}}$ can be expressed by the help of the velocity profile function $\hat{\mathbf{u}}$

$$\tilde{\mathbf{u}} = \mathbf{u} - \overline{\mathbf{u}} = \lim_{\varepsilon_{\hat{\mathbf{u}}}\to 0} \{\hat{\mathbf{u}}(\xi) - \overline{\mathbf{u}}\} \tag{4.21}$$

provided that the modelling error $\varepsilon_{\hat{\mathbf{u}}}$ is small.

4.2.3 Film Temperature

The mean temperature $\overline{T}$ is defined as

$$\overline{T} = \frac{1}{h}\int_h T\, dz \tag{4.22}$$

The temperature distribution across the film thickness, the temperature profile, is non-uniform and can be an important factor in the etching process. The temperature distribution across the film height can be reconstructed with the help of a polynomial temperature profile function analog to the velocity profiles.

However, due to a diffusion-controlled etching model introduced later in the thesis being independent of the fluid temperature and due to the momentum and continuity equations being decoupled from the energy equation because of the constant density, only few examples of temperature boundary conditions that can be considered in a derivation of the polynomial temperature profile function are suggested:

- Prescribed disc temperature

$$T|_{z=0} = T_{\text{disc}} \tag{4.23a}$$

  or the heat flux at the disc

$$-\lambda \left.\frac{\partial T}{\partial z}\right|_{z=0} = \mathbf{q}_{\text{disc}} \tag{4.23b}$$

- Evaluation of the energy equation in the limit of the steady-state condition yields at the film bottom

$$\left.\frac{\partial^2 T}{\partial z^2}\right|_{z=0} = 0 \tag{4.24}$$

- Thermal boundary δ_T contained inside the film thickness

$$\left.\frac{\partial T}{\partial z}\right|_{z=\delta_T} = 0 \tag{4.25}$$

- No heat transfer

$$\left.\frac{\partial T}{\partial z}\right|_{z=h} = 0 \tag{4.26a}$$

or prescribed heat transfer at the free-surface

$$-\lambda\left.\frac{\partial T}{\partial z}\right|_{z=h} = \alpha(T|_{z=h} - T_{\text{gas}}) \tag{4.26b}$$

where α is the heat transfer coefficient between the liquid and the ambient gas.

4.3 Thin Film Transformation

The starting point of the thin film transformation are the incompressible isothermal Navier-Stokes equations 2.25.

4.3.1 Transformation of Continuity Equation

In order to transform the continuity equation the behaviour of the film elevation at the free-surface has to be described

$$\frac{\partial h}{\partial t} + u|_{z=h}\frac{\partial h}{\partial x} + v|_{z=h}\frac{\partial h}{\partial y} - w|_{z=h} = 0 \tag{4.27}$$

The no slip boundary condition at the disc

$$\mathbf{u}|_{z=0} = \mathbf{u}_{\text{disc}} \tag{4.28}$$

surprisingly does not have a direct influence in the transformation of the continuity equation as the constancy of the bottom b radically simplifies the kinematic boundary condition at the disc

$$\begin{gathered} u|_{z=0}\frac{\partial b}{\partial x} + v|_{z=0}\frac{\partial b}{\partial y} + w|_{z=0} = \\ w|_{z=0} = 0 \end{gathered} \tag{4.29}$$

The transformation of the continuity equation is done through the integration of the equation across the film height using the Leibniz integral rule, Appendix B.2.2

$$
\begin{aligned}
&\int_0^h \nabla_\bullet \mathbf{u}\, dz \\
&\quad = \int_0^h \left(\frac{\partial u}{\partial x} + \frac{\partial v}{\partial y} + \frac{\partial w}{\partial z} \right) dz \\
&\quad = \frac{\partial}{\partial x} \int_0^h u\, dz + \frac{\partial}{\partial y} \int_0^h v\, dz \\
&\qquad - u|_{z=h} \frac{\partial h}{\partial x} - v|_{z=h} \frac{\partial h}{\partial y} + w|_{z=h} - w|_{z=0} \\
&\quad = 0
\end{aligned}
\tag{4.30}
$$

Using the elevation of the film at the free-surface 4.27, the bottom boundary condition 4.29 and applying the definition of the mean velocity 4.10 then yields the thin film continuity equation

$$
\frac{\partial h}{\partial t} + \nabla_\bullet (h \overline{\mathbf{u}}) = 0 \tag{4.31}
$$

4.3.2 Pressure Solution

The important aspect of the thin film transformation is the pressure solution. In order to solve the pressure, the z-momentum equation of the Navier-Stokes equations under the consideration of the Newton's law of viscosity 2.14 has to be investigated

$$
\begin{aligned}
&\rho \left[\frac{\partial w}{\partial t} + \frac{\partial uw}{\partial x} + \frac{\partial vw}{\partial y} + \frac{\partial w^2}{\partial z} \right] \\
&\qquad = \frac{\partial \tau_{zx}}{\partial x} + \frac{\partial \tau_{zy}}{\partial y} + \frac{\partial (\tau_{zz} - p)}{\partial z} + F_{b_z}
\end{aligned}
\tag{4.32}
$$

where F_{b_z} represents the body force contribution in the z-direction.

Using the assumption of non-existent cross flow 4.1 and a scaling argument that the shear stress terms are small compared to the pressure derivative and gravity, the whole equation collapses into

$$
\frac{\partial p}{\partial z} = -\rho g \tag{4.33}
$$

Considering the pressure boundary condition at the free-surface

$$
p|_{z=h} = p_{\text{gas}} + \sigma \kappa \tag{4.34}
$$

the pressure solution for the thin film can be obtained

$$p = p_{\text{gas}} + \rho g(h - z) - \sigma\kappa \tag{4.35}$$

where the surface curvature κ is approximated by

$$\kappa \approx \nabla_\bullet \nabla h \tag{4.36}$$

The solution represents a hydrostatic pressure distribution and the effect of the surface tension.

Considering the fluid incompressibility, the ambient gas pressure is irrelevant as only the change of pressure exists in the equations and can be neglected.

The pressure solution can than be used to derive the pressure gradient under assumption of the constant pressure across the film

$$\nabla p = \nabla \left(\rho \left\|\mathbf{g}\right\| h - \sigma\kappa\right) \tag{4.37}$$

4.3.3 Transformation of Momentum Equation

First the left hand side (LHS) of the momentum equation is investigated where a special care is taken of the convective term. The convective term is expanded using the velocity decomposition 4.17 in order to disclose the non-uniform momentum transport across the film thickness

$$\begin{aligned}
&\int_0^h \rho \left[\frac{\partial \mathbf{u}}{\partial t} + \nabla_\bullet (\mathbf{u}\mathbf{u})\right] dz \\
&\quad = \int_0^h \rho \frac{\partial \mathbf{u}}{\partial t}\, dz + \int_0^h \rho \nabla_\bullet \left[(\overline{\mathbf{u}} + \tilde{\mathbf{u}})(\overline{\mathbf{u}} + \tilde{\mathbf{u}})\right] dz \\
&\quad = \rho \frac{\partial}{\partial t} \int_0^h \mathbf{u}\, dz + \rho \nabla_\bullet \left[\int_0^h \left(\overline{\mathbf{u}}\overline{\mathbf{u}} + \overline{\mathbf{u}}\tilde{\mathbf{u}} + \tilde{\mathbf{u}}\overline{\mathbf{u}} + \tilde{\mathbf{u}}\tilde{\mathbf{u}}\right) dz\right] \\
&\quad = \rho \frac{\partial}{\partial t}(h\overline{\mathbf{u}}) + \rho \nabla_\bullet (h\overline{\mathbf{u}}\overline{\mathbf{u}}) + \rho \nabla_\bullet \left(\int_0^h \tilde{\mathbf{u}}\tilde{\mathbf{u}}\, dz\right)
\end{aligned} \tag{4.38}$$

The boundary terms after application of the Leibniz integral rule diminish due the film elevation boundary condition 4.27 and the bottom boundary condition 4.29.

The expanded convective term contains four correlations. The correlations of the mean velocity and its spatial fluctuating component in the product forms $\overline{\mathbf{u}}\tilde{\mathbf{u}}$ and $\tilde{\mathbf{u}}\overline{\mathbf{u}}$ reduce to zero with the help of identities 4.19 and 4.20. The convective term is as the result formed by the product of the mean velocities $\overline{\mathbf{u}}\overline{\mathbf{u}}$ and a new term, the product of the spatial velocity perturbations $\tilde{\mathbf{u}}\tilde{\mathbf{u}}$. This illustrates the fact that an average of the product of two functions is not the product of the their averages only.

Applying the velocity profile $\hat{\mathbf{u}}$ and its solution 4.16 into the modelling of the spatial velocity fluctuation $\tilde{\mathbf{u}}$ than yields

$$\begin{aligned}
&\rho\nabla\bullet\left(\int_0^h \tilde{\mathbf{u}}\tilde{\mathbf{u}}\,dz\right)\\
&\qquad=\lim_{\varepsilon_{\hat{\mathbf{u}}}\to 0}\left\{\rho\nabla\bullet\left[\int_0^1\left(\hat{\mathbf{u}}(\xi)-\overline{\mathbf{u}}\right)\left(\hat{\mathbf{u}}(\xi)-\overline{\mathbf{u}}\right)h\,d\xi\right]\right\}\\
&\qquad=\rho\nabla\bullet\left[\frac{213}{875}h(\overline{\mathbf{u}}-\mathbf{u}_{\text{disc}})(\overline{\mathbf{u}}-\mathbf{u}_{\text{disc}})\right]
\end{aligned}\tag{4.39}$$

The right hand side (RHS) of the momentum equation integrated across the film thickness under the assumptions of the constant pressure through the film height and no interface friction and using the pressure solution 4.37 yields

$$\begin{aligned}
&\int_0^h\left[-\nabla\bullet p+\nabla\bullet\tau\right]dz+\mathbf{F}_b\\
&\qquad=-h\nabla\bullet p+\nabla\bullet\left(h\mu\nabla\overline{\mathbf{u}}\right)-\tau_z|_{z=0}+\mathbf{F}_b\\
&\qquad=-h\nabla\left(\rho\left\|\mathbf{g}\right\|h-\sigma\kappa\right)+\nabla\bullet\left(h\mu\nabla\overline{\mathbf{u}}\right)-\tau_z|_{z=0}+\mathbf{F}_b
\end{aligned}\tag{4.40}$$

In order to express the shear stress at the film bottom the polynomial velocity profile function $\hat{\mathbf{u}}$ and its solution 4.16 are used

$$\begin{aligned}
&\tau_z|_{z=0}\\
&\qquad=\mu\frac{\partial\mathbf{u}}{\partial z}\bigg|_{z=0}\\
&\qquad=\lim_{\varepsilon_{\hat{\mathbf{u}}}\to 0}\left\{\mu\frac{\partial\hat{\mathbf{u}}(\xi)}{\partial h\xi}\bigg|_{\xi=0}\right\}\\
&\qquad=\frac{12}{5}\frac{\mu}{h}(\overline{\mathbf{u}}-\mathbf{u}_{\text{disc}})
\end{aligned}\tag{4.41}$$

provided the modelling error $\varepsilon_{\hat{\mathbf{u}}}$ is small.

4.4 Summary and Discussion

The final form of the conservative incompressible Thin Film Model (TFM) is summarised as

- Continuity equation

$$\frac{\partial h}{\partial t}+\nabla\bullet\left(h\overline{\mathbf{u}}\right)=0\tag{4.42a}$$

- Momentum equation

$$\rho\left[\frac{\partial}{\partial t}(h\overline{\mathbf{u}}) + \nabla_{\bullet}\left(h\overline{\mathbf{u}}\overline{\mathbf{u}} + \mathbf{K}\right)\right] = -h\nabla\left(\rho\,\|\mathbf{g}\|\,h - \sigma\nabla_{\bullet}\nabla h\right) + \nabla_{\bullet}\left(h\mu\nabla\overline{\mathbf{u}}\right) - \tau_z|_{z=0} + \mathbf{F}_b \tag{4.42b}$$

  where the convective term $\mathbf{K}$ and the shear-stress at the film bottom are expressed with the help of the polynomial velocity profile function $\hat{\mathbf{u}}$ as

$$\mathbf{K} = \frac{213}{875}h(\overline{\mathbf{u}} - \mathbf{u}_{\text{disc}})(\overline{\mathbf{u}} - \mathbf{u}_{\text{disc}})$$
$$\tau_z|_{z=0} = \frac{12}{5}\frac{\mu}{h}(\overline{\mathbf{u}} - \mathbf{u}_{\text{disc}})$$

  and body force $\mathbf{F}_b$ has to be determined on the case-to-case basis.

- Equation of State

$$\rho = \text{const.} \tag{4.42c}$$

- Transport coefficient

$$\mu = \mu(p) \tag{4.42d}$$

The important factor in the precision of the thin film model is the modelling error of its velocity profiles $\varepsilon_{\hat{\mathbf{u}}}$. The resulting solution of the presented thin film model will be close to the real thin film, if the velocity profile function $\hat{\mathbf{u}}$ is closely resembling the real velocity distribution $\mathbf{u}$. And vice versa, the solution of the thin film model will show a discrepancy from the real thin film should the modelling error of the velocity profiles $\varepsilon_{\hat{\mathbf{u}}}$ be significant. However the modelling error has in the given formulation only a local influence. The mass and the momentum within the system will always be properly conserved.

Chapter 5

Thin Film Approximation

The Thin Film Model (TFM) derived in the previous chapter is used to solve efficiently fluid flow problems on rotating discs with an impinging jet being either static or dynamically moving over the disc surface. As some of the assumptions placed on TFM in such configurations are invalidated, the resulting approach is called Thin Film Approximation (TFA). The implementation is carried out in the open-source software toolbox OpenFOAM® using the Finite Area (FA) method. The validation is done by comparison of the TFA results with VoF simulations performed with the ANSYS Fluent software. The chapter presents the TFA, its implementation details and the validation.

5.1 Model and Reality

The TFM model assumptions can be applied on the majority of the film flow on the rotating disc. There however exists few typical areas where the TFM assumptions, especially the main assumption of negligible flow in the disc normal direction, are not valid.

The first problem zone is the hydraulic jump. The phenomenon was presented already during the VoF investigations. Its true nature is an abrupt increase of the film height as a supercritical flow[1] is slowed down. This is directly connected to the transformation of the kinetic energy into static one and the flow separation as there exists a region in which the flow is reversed with respect to the mean flow direction in the hydraulic jump. The reversed flow forms an eddy, also called a *separation bubble*, at the hydraulic jump bottom as reported by Yokoi and Xiao[121]. The presence of the separation bubble clearly disregards the assumption of non-existent cross flow as there happens a momentum transport in the normal direction.

The polynomial velocity profile function $\hat{\mathbf{u}}$ is not properly describing the real

[1] A supercritical flow has a higher velocity than the propagation speed of the wave.

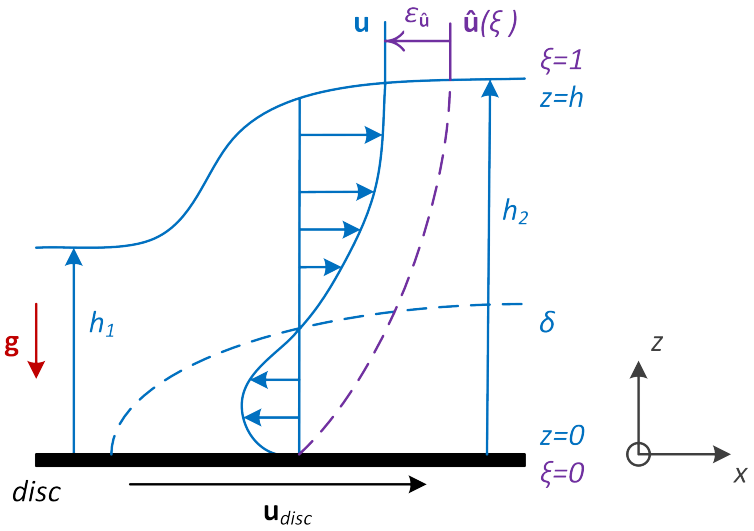

Figure 5.1: Hydraulic jump in TFA

velocity distribution in the hydraulic jump and introduces a huge velocity profile modelling error $\varepsilon_{\hat{\mathbf{u}}}$, see figure 5.1, as the separation boundary δ is not accounted for. As a result, the shear stress contribution to the momentum equation is wrongly evaluated what has a direct influence on the film height in the given location.

The impinging jet forms the second problem zone. The free-falling jet has a dominant z-momentum component that is being transformed into x- and y-momentum component in the impingement area. The flow in the impingement area thus hides complex flow structures that are further enhanced by an influence of the surrounding film flow.

The TFM model cannot deal with such a situation and the solution directly under the jet is invalid and has to be prescribed by other means, for example based on a 3D VoF solution. The solution in the jet vicinity, that is in the impingement area, can be understood only as a coarse approximation. Farther away from the jet the more precise the film solution gets.

The application of the TFM model on real problems that include above mentioned problem zones has to be carefully evaluated. The resulting approach is being called Thin Film Approximation (TFA) due to accepted errors in the film solution.

5.2 Finite Area Method

The classical numerical method used for the solution of the partial differential equations of the fluid dynamics is the FV method. The method, as described by Eymard et al.[30] or Versteeg and Malalasekera[107], is particularly suited for the solution of various conservation laws as it can be used on arbitrary geometries, structured and unstructured meshes and it possess a local conservativity of

numerical fluxes.

The local conservativity means, that using the divergence theorem, Appendix B.2.1, volume integrals of the partial differential equations are converted into surface integrals, that is the integral formulation of the fluxes over the discretisation cells boundary. The numerical flux is then conserved from one discretisation cell to its neighbour. The fluxes on the boundary are discretized with respect to the discrete unknowns.

The FV method could be used for the simulation of the film flow on a surface, namely the rotating disc. However, the three-dimensional nature of the FV method applied on two-dimensional thin film problem would pose some technical problems. Thus more suitable is an application of two-dimensional specialisation of the FV method for surface flows called Finite Area (FA) method developed by Tuković[102].

The FA method can be seen as a dimensional reduction of the FV method where control volumes are reduced to control areas. The balance equations are written as usual around the discretisation cells utilising the divergence theorem, however this time surface integrals of the partial differential equations are transformed into line integrals over the control area boundary edges.

The FA method is implemented in the foam-1.6-extend[75] distribution of the OpenFOAM® the implementation environment of the TFA solver itself. Therefore a brief primer on the FA discretisation in OpenFOAM® is given. Considering the link between FA and FV method, the fundamental description of the FV discretisation in the OpenFOAM® by Jasak[50] is not just a valuable complement but the source of majority skipped details such as an implementation of differencing schemes, a flux calculation, a discussion of non-orthogonality decompositions, an implementation of boundary conditions etc.

5.2.1 Discretisation of the Solution Domain

The FA space discretisation in the OpenFOAM® divides the solution domain into control areas A, see figure 5.2. Control areas do not overlap and completely fill the solution domain.

The computational point P is located at the centroid of the control area A so that following equation holds

$$\int_{A_P} (\mathbf{x} - \mathbf{x}_P)\, dA = 0 \tag{5.1}$$

where A_P denotes the control area around the point P and $\mathbf{x}_P$ denotes the centroid position.

The control area boundary is defined by the set of edges e. For simplicity, the edge symbol e represents as well the edge centre point.

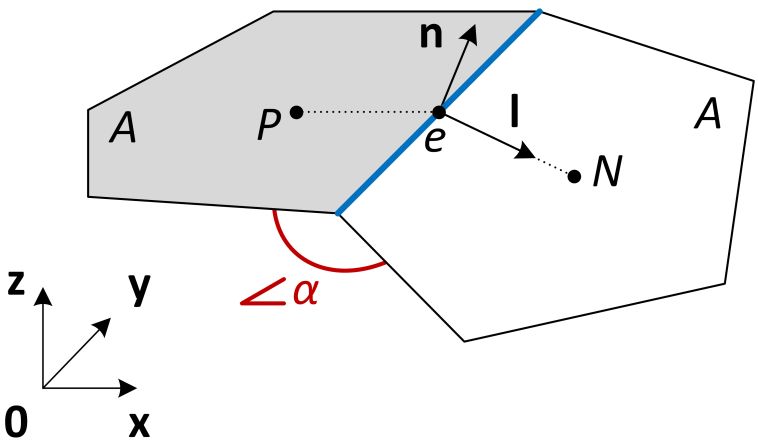

Figure 5.2: Finite Area: Control area

Two control areas–the owner cell with centre P and the neighbour cell with centre N–share a single edge e. The edge length vector $\mathbf{l}$ is pointing outward from the owner cell, is normal to the edge e and has the magnitude of the edge length.

Specific to the FA is the surface curvature due to an angle α between neighbouring control areas. Thus FA spatial domain forms an arbitrary three-dimensional surface.

The time discretisation is identical with FV discretisation. It is sufficient to define a time step Δt as the solution evolves in discrete time increments from the prescribed initial condition.

5.2.2 Discretisation of Transport Equation

The general transport equation 2.26 is a second-order equation due to the second derivative of the transported property in space inside of the diffusive term. Thus the discretisation has to be of an equal or a higher order as the order of the equation itself to maintain a good accuracy.

The order of discretisation is directly connected to the assumed variation of the solution ϕ around the point P. The resulting discretisation will have the second-order accuracy if we assume the linear solution variation

$$\begin{aligned} \phi(\mathbf{x}) &= \phi_P + (\mathbf{x} - \mathbf{x}_P) \cdot (\nabla\phi)_P \\ \phi(t + \Delta t) &= \phi^t + \Delta t \left(\frac{\partial \phi}{\partial t}\right)^t \end{aligned} \tag{5.2}$$

where ϕ_P and ϕ^t denote the scalar property at the point P and time t respectively.

The proof is done by a comparison of the linear solution variation with a general form of Taylor series expansion of the solution function ϕ around position $\mathbf{x}$ fol-

lowed by an evaluation of the truncation error scaling. The similar analysis can be done for the temporal accuracy. The proof details and discussion can be found in the works of Damián[24] or Jasak[50].

The FA method requires that the general transport equation 2.26 is satisfied over the control area A around the point P in the integral scalar form

$$\begin{aligned}\int_t^{t+\Delta t}\left(\frac{\partial}{\partial t}\int_{A_P}\rho\phi\,dA\right)dt+\int_t^{t+\Delta t}\left[\int_{A_P}\nabla\bullet\left(\rho\mathbf{u}\phi\right)\,dA\right]dt\\ =\int_t^{t+\Delta t}\left[\int_{A_P}\nabla\bullet\left(\rho\Gamma_\phi\nabla\phi\right)\,dA\right]dt+\int_t^{t+\Delta t}\left(\int_{A_P}S_\phi(\phi)\,dA\right)dt\end{aligned} \tag{5.3}$$

5.2.3 Temporal Term

The assumed linear variation of ϕ along the time step described by equation 5.2 can be used to directly express the time derivative

$$\begin{aligned}&\frac{\partial}{\partial t}\int_{A_P}\rho\phi\,dA\\ &\qquad=\frac{\partial}{\partial t}(\rho_P\phi_P A_P)\\ &\qquad=\frac{(\rho_P^n\phi_P^n A_P^n)-(\rho_P^o\phi_P^o A_P^o)}{\Delta t}\end{aligned} \tag{5.4}$$

where superscripts n and o denote the new and old time time level respectively. The expression can be further simplified if the computational mesh and/or density are assumed constant.

From the same linear solution variation follows the calculation of time integrals utilising the Generalised Trapezoidal Method described by Hirsch[45] as

$$\int_t^{t+\Delta t}\phi(t)\,dt=\left[\gamma\phi^n+(1-\gamma)\phi^o\right]\Delta t \tag{5.5}$$

where γ decides about time discretisation method. The value of $\gamma=0$ represents the *Forward Euler* explicit scheme. The value of $0<\gamma\leq 1$ selects an implicit scheme. The *Backward Euler* temporal scheme is connected to the value $\gamma=1$ and the *Crank-Nicholson* scheme to the value $\gamma=1/2$.

5.2.4 Spatial Terms

The selection of the computational point P in the centroid of the discretisation cell is not random. Using the assumption of the solution linear variation 5.2 and definition of the centroid 5.1, following applies for the control area A around the

point P

$$\begin{aligned}
&\int_{A_P} \phi(\mathbf{x})\, dA \\
&\qquad = \int_{A_P} \left[\phi_P + (\mathbf{x}-\mathbf{x}_P)\cdot(\nabla\phi)_P\right]\, dA \\
&\qquad = \phi_P \int_{A_P} dA + \underbrace{\left[\int_{A_P} (\mathbf{x}-\mathbf{x}_P)\, dA\right]}_{\text{area centroid}} \cdot(\nabla\phi)_P \\
&\qquad = \phi_P A_P
\end{aligned} \tag{5.6}$$

The discretized divergence operator is a powerful tool necessary for the discretisation of convective and diffusive terms. The transformation is based on the Gauss divergence theorem, Appendix B.2.1. Considering that the control area A is bounded by the set of edges e and using the linear variation assumption 5.2, the discretisation of the divergence operator follows

$$\begin{aligned}
&\int_{A_P} \nabla_\bullet(\mathbf{a})\, dA \\
&\qquad = \oint_{\partial A_P} \mathbf{a}\cdot\mathbf{l}\, ds \\
&\qquad = \sum_e \left(\int_e \mathbf{a}\cdot\mathbf{l}\, ds\right) \\
&\qquad = \sum_e \left\{ \left[\int_e \mathbf{l}\, ds\right]\cdot\mathbf{a}_e + \underbrace{\left[\int_e (\mathbf{x}-\mathbf{x}_e)\mathbf{l}\, ds\right]}_{\text{line centroid}} : (\nabla\mathbf{a})_e \right\} \\
&\qquad = \sum_e \mathbf{l}\cdot\mathbf{a}_e
\end{aligned} \tag{5.7}$$

where $\mathbf{a}$ is a general vector value and the subscript e denotes the value in the middle of the edge.

The discretisation of the gradient operator, needed for example by the pressure gradient, follows the same method as the discretisation of the divergence operator and yields

$$\begin{aligned}
&\int_{A_P} \nabla(\mathbf{a})\, dA \\
&\qquad = \oint_{\partial A_P} \mathbf{a}\,\mathbf{l}\, ds \\
&\qquad = \sum_e \left\{ \left[\int_e \mathbf{l}\, ds\right]\mathbf{a}_e + \underbrace{\left[\int_e (\mathbf{x}-\mathbf{x}_e)\mathbf{l}\, ds\right]}_{\text{line centroid}} \cdot(\nabla\mathbf{a})_e \right\} \\
&\qquad = \sum_e \mathbf{l}\,\mathbf{a}_e
\end{aligned} \tag{5.8}$$

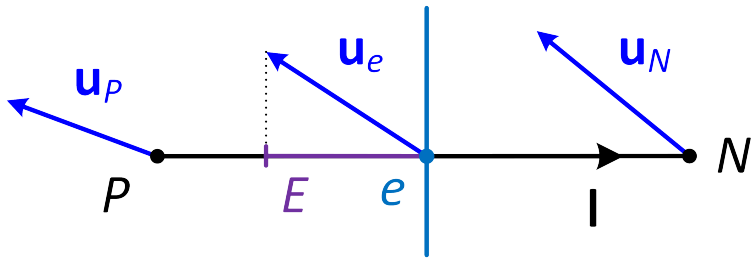

Figure 5.3: Edge flux

5.2.4.1 Convective Term

The convective term is discretized with the help of the discretized divergence operator 5.7

$$\begin{aligned}\int_{A_P} \nabla\bullet\left(\rho\mathbf{u}\phi\right) dA \\ &= \sum_e \mathbf{l}\cdot\left(\rho\mathbf{u}\phi\right)_e \\ &= \sum_e \mathbf{l}\cdot\left(\rho\mathbf{u}\right)_e\phi_e \\ &= \sum_e E\phi_e\end{aligned} \tag{5.9}$$

where E denotes the mass flux through the edge e.

The edge flux E defined as

$$E = \mathbf{l}\cdot\left(\rho\mathbf{u}\right)_e \tag{5.10}$$

can be geometrically interpreted as a projection of $(\rho\mathbf{u})_e$ on the length edge vector $\mathbf{l}$, see figure 5.3. Thus the edge flux describes a net flow through the edge and its sign decides between an inflow and an outflow.

The flux calculation is using the Flux Corrected Transport (FCT) technique by Boris and Book[12] with improvements by Zalesak[122].

The calculation of the edge value ϕ_e depends on convective differencing schemes. The FA differencing schemes have to pay a special attention to the surface curvature between neighbouring control areas, see figure 5.4.

Assuming the linear variation of ϕ between owner cell centre P and neighbour cell centre N, the edge value ϕ_e can be calculated using the mid-point rule as

$$\phi_e = e_x\phi_P + (1 - e_x)\phi_N \tag{5.11}$$

where the edge interpolation factor e_x is defined as the ratio of distances $\overline{eN}$ and $\overline{PeN}$

$$e_x = \frac{\overline{eN}}{\overline{PeN}} \tag{5.12}$$

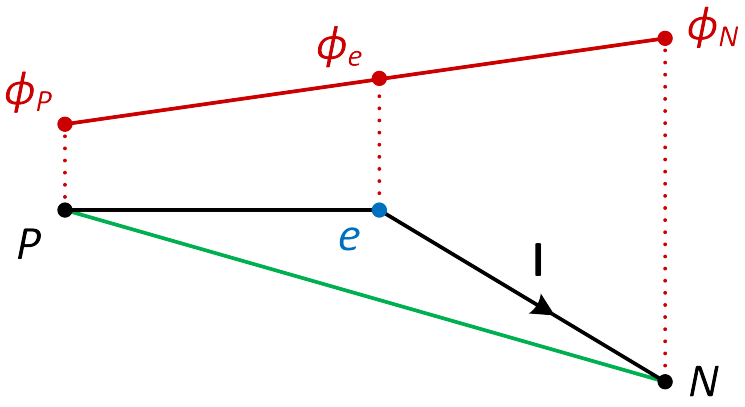

Figure 5.4: Finite Area: Edge interpolation

Note that denominator distance is accounting for the curvature opposite to the denominator distance $\overline{PN}$, depicted in the green colour, used in the FV discretisation. However, it should be mentioned that the curvature treatment has no influence in the case of the rotating disc that is placed in a single plane.

The differencing scheme using the equation 5.11 for the edge values is called *Central Differencing*.

On other side not every differencing scheme is influenced by the surface curvature. As an example can be mentioned the *Upwind Differencing* where the edge value depends on the flow direction described by the edge flux E

$$\phi_e = \begin{cases} \phi_P & \text{for } E \geq 0 \\ \phi_N & \text{for } E < 0 \end{cases} \tag{5.13}$$

5.2.4.2 Diffusive Term

The transformation of the diffusive term follows the convective one. Applying the discretized Gauss divergence theorem 5.7, the diffusive term is discretized as

$$\begin{aligned} &\int_{A_P} \nabla \bullet \left(\rho \Gamma_\phi \nabla \phi\right) \, dA \\ &\quad = \sum_e \mathbf{l} \cdot (\rho \Gamma_\phi \nabla \phi)_e \\ &\quad = \sum_e (\rho \Gamma_\phi)_e \mathbf{l} \cdot (\nabla \phi)_e \end{aligned} \tag{5.14}$$

The challenging part of the discretized diffusive term is the evaluation of the term $\mathbf{l} \cdot (\nabla \phi)_e$. The calculation is straightforward for the orthogonal meshes

$$\mathbf{l} \cdot (\nabla \phi)_e = \|\mathbf{l}\| \frac{\phi_N - \phi_P}{\overline{PeN}} \tag{5.15}$$

where $\overline{PeN}$ describes the distance along the curved surface between owner and neighbour control areas. The curvature as such is not present in the FV method where the distance would be just $\overline{PN}$ along the straight line.

Unfortunately the orthogonality is not guaranteed in the most cases and specific treatment is necessary. The main idea in dealing with non-orthogonal meshes is splitting the orthogonal and non-orthogonal contributions into separate terms. Many possibilities exists for the contribution decomposition.

5.2.4.3 Source Term

The source contains all other terms which could not be expressed as temporal, convective or diffusive. The discretisation of the source terms have to be done on the case-to-case basis. In every case, the source term has to be linearised

$$\begin{aligned} \int_{A_P} S_\phi(\phi)\, dA &= \int_{A_P} \left[S_a(\phi) + S_b(\phi)\phi\right]\, dA \\ &= S_a(\phi)A_P + S_b(\phi)\phi_P A_P \end{aligned} \tag{5.16}$$

5.2.5 Solving of Discretized Equations

The presented discretisation applied on partial differential equations of a real problem leads to complex algebraic expressions based on present terms and selected differencing schemes. However, the main purpose of the numerical solution is the calculation of a new value of the scalar property at the centroid of the discretisation cell, that is ϕ_P^n. The terms connected to edges between control areas, the edge values ϕ_e and the edge gradients $(\nabla\phi)_e$, are all dependent on the value of the edge owner cell ϕ_P and its neighbour ϕ_N. Therefore the discretisation of the general transport equation has for every single discretisation cell A_P a general form

$$a_P\phi_P^n + \sum_N a_N\phi_N^n = R_P \tag{5.17}$$

where a_P and a_N are the cell and its neighbours coefficients and R_P is the cell source term.

As the value of discretisation cell ϕ_P itself is dependent on the values of its surrounding ϕ_N, a linear system of equations

$$A\boldsymbol{\phi} = \mathbf{R} \tag{5.18}$$

where A is a sparse matrix with the diagonal coefficients a_P and the off-diagonal coefficients a_N, $\boldsymbol{\phi}$ is the vector of unknowns and $\mathbf{R}$ is the source term vector, can be formed.

The linear equation system is usually asymmetric in the presence of the non-linear

convective term, but can as well be symmetric if the non-linear convective term is missing or it is using centred differencing scheme.

The solution of the linear equation system in OpenFOAM® is found by iterative linear equation solvers. The solvers provided in the OpenFOAM® for symmetric systems are, for example, the Preconditioned Conjugate Gradient (PCG) and the Diagonal Incomplete-Cholesky (DIC) solvers. The Preconditioned Bi-Conjugate Gradient (PBiCG) solver or the Gauss-Seidel smoother can be applied on the asymmetric systems. Lately, the Geometric-Algebraic Multi-Grid (GAMG) solver is catching a lot of attention especially in the solution of problems in the order of hundred thousands unknowns[2].

5.3 Solver Implementation

The TFA solver was implemented in the `foam-1.6-extend` OpenFOAM® distribution using the FA code base. The base stock solvers used as implementation starting points were `surfactantFoam`, that demonstrates the FA technique, and `shallowWaterFoam`, that has a roughly similar underlaying albeit FV model.

The TFA solver code ultimately grown up into full-fledged object-oriented transient incompressible solver for the thin film simulations on the rotating disc. For an illustration, the resulting TFA solver contains 2298 lines of C/C++ code while `shallowWaterFoam` has 221 and `surfactantFoam` encompasses only 131 lines of the C/C++ code.

The discretisation of the TFM equations in the OpenFOAM® will be presented at first. The discussion of the important topics that are either specific to the FA method or to the TFA solver, namely the non-linearity of the momentum equation, the calculation of edge flux, the pressure-velocity coupling and the inlet implementation and treatment, follows.

5.3.1 Discretisation of the Thin Film Model

The discussed FA discretisation technique has to be applied on the TFM equations in order to transform them into linear equation systems suitable for the numerical solution.

Recalling the TFM equations

$$\frac{\partial h}{\partial t} + \nabla_{\bullet}\left(h\overline{\mathbf{u}}\right) = 0 \tag{5.19a}$$

[2]Solution unknowns are connected to the centroids of the discretisation cells thus one can link their amount to the number of the mesh cells.

$$\frac{\partial}{\partial t}(h\overline{\mathbf{u}}) + \nabla\bullet\ (h\overline{\mathbf{u}}\overline{\mathbf{u}} + \mathbf{K}) = -\frac{h}{\rho}\nabla p + \nabla\bullet\ (h\nu\nabla\overline{\mathbf{u}}) - \tau_z|_{z=0} \tag{5.19b}$$

where $\mathbf{K}$ is the advective term dependent on the velocity profile and p being the pressure solution, the discretisation is effectively performed by the OpenFOAM® as presented in the following code fragments:

TFA solver: `continuityEqn.H`; some variable names changed

```
// continuity equation
faScalarMatrix hEqn
(
      fam::ddt(h)
    + fam::div(E, h)
);
⋮
solve(hEqn);
```

TFA solver: `momentumEqn.H`; some variable and function names changed

```
// momentum equation
faVectorMatrix UEqn
(
      fam::ddt(h, U)
    + fam::div(fac::interpolate(h) * E, U)
    + velocityProfile->convectionK()
    ==
      fam::laplacian(nu * h, U)
    - (nu / (h + SMALL_LENGTH)) *
        velocityProfile->zDerivative(0)
);
⋮
solve(UEqn == -(h / rho) * fac::grad(p));
```

The OpenFOAM® code surprises by its elegance and a powerful connection to the original partial differential equation.

Note the temporal derivative of the film height h in the continuity equation stemming from the TFM transformation. The film height h naturally links the pressure solution into the continuity equation.

5.3.2 Non-Linearity of the Convective Term

The non-linearity of the convective term in the momentum equation 5.19b poses a problem. The discretisation of the term using equation 5.9 would yield squares of mean velocities[3] and therefore would be non-linear. The non-linear terms cannot

[3]The term velocity and mean velocity might be interchanged freely in the context of the TFA solver.

be solved by linear equation solvers. Two options suggest themselves–a computationally expensive non-linear equation solver or a linearisation of the term prior to numerical solution.

The linearisation treatment is focused on the dealing with the edge flux E so that the squares of unknown mean velocities are avoided. This can be achieved by use of the already known edge flux from the previous time step under assumption that mean velocity solution does not change much

$$\overline{\mathbf{u}} \approxeq \overline{\mathbf{u}}^o \tag{5.20}$$

so that the convective term discretisation follows

$$\begin{aligned} &\int_{A_P} \nabla\bullet\,(h\overline{\mathbf{u}}\overline{\mathbf{u}})\,dA \\ &\qquad \approxeq \sum_e \mathbf{l}\cdot(h\overline{\mathbf{u}}^o\overline{\mathbf{u}})_e \\ &\qquad = \sum_e \mathbf{l}\cdot(h\overline{\mathbf{u}}^o)_e\overline{\mathbf{u}}_e \\ &\qquad = \sum_e E^o\overline{\mathbf{u}}_e \end{aligned} \tag{5.21}$$

It is obvious that using edge flux delayed in time by the time step Δt has no effect on steady-state solutions. The situation is a bit different for transient solutions though. If the size of the time step induces changes in the mean velocity solution, either an increased number of iterations over the linearised non-linear terms or the smaller time step will improve the solution accuracy.

5.3.3 Calculation of the Edge Flux

The calculation of the edge fluxes of TFA solver is slightly different due to the TFM momentum equation form containing the film height h.

The derivation of the flux expression starts with a semi-discretized form of the momentum equation as suggested by Rhie and Chow[88]

$$a_P\overline{\mathbf{u}}_P = \mathbf{H}(\overline{\mathbf{u}}) - \frac{h}{\rho}\nabla p \tag{5.22}$$

where the pressure gradient is not discretized yet. The equation is achieved by discretisation of the integral form of the momentum equation and dividing by the discretisation cell areas so the cell coefficients can be interpolated to the cell edges.

The operator $\mathbf{H}$ accounts for the convective term, the diffusive term and all source

terms including the source part of the transient term

$$\mathbf{H}(\overline{\mathbf{u}}) = -\sum_N a_N \overline{\mathbf{u}}_N + \frac{\overline{\mathbf{u}}^o}{\Delta t} \tag{5.23}$$

The mean velocities at the discretisation cell edges can be expressed as the edge interpolates of the manipulated equation 5.22

$$\overline{\mathbf{u}}_e = \left(\frac{\mathbf{H}(\overline{\mathbf{u}})}{a_P}\right)_e - \left(\frac{h}{\rho a_P}\right)_e (\nabla p)_e \tag{5.24}$$

The edge flux E defined by 5.10 is then be evaluated as

$$E = \mathbf{l} \cdot \overline{\mathbf{u}}_e = \mathbf{l} \cdot \left[\left(\frac{\mathbf{H}(\overline{\mathbf{u}})}{a_P}\right)_e - \left(\frac{h}{\rho a_P}\right)_e (\nabla p)_e\right] \tag{5.25}$$

and can be seen in the following code fragment in-between the momentum equation solution and the continuity equation solution:

TFA solver: `continuityEqn.H`; some variable names changed

```
const areaScalarField ap = UEqn.A();
const areaVectorField HU = UEqn.H();

U = UH / ap; // momentum approximation

E =  (fac::interpolate(U) & aMesh.Le())
   - fac::interpolate(h / (rho * ap)) * fac::lnGrad(p)
       * aMesh.magLe();
```

5.3.4 Pressure-Velocity Coupling

The TFM equations show a dependency of the film height h on the mean velocity $\overline{\mathbf{u}}$ and vice versa. Considering that the pressure solution 4.37 is a function of the film height, the classic naming *pressure-velocity coupling* will be used. The coupling between continuity and momentum equations requires a special treatment.

The first option is a *simultaneous solution* of coupled equations as presented in the works of Caretto et al.[18] or Vanka[106]. The second option, called a *segregated approach*, solves the coupled equations sequentially one after another and gained huge popularity as it needs much less computational resources. The typical segregated algorithm for steady-state problems is the Semi-Implicit Method for Pressure Linked Equations (SIMPLE) by Patankar[79] and its derivations. Transient problems are better served with the segregated Pressure Implicit Split of Operator (PISO) algorithm introduced by Issa[47, 48]. Further details on the PISO algorithm can be found in the work of Oliveira and Issa[80].

The TFA solver structure is a projection of the pressure-velocity coupling. Because TFA solver is oriented on transient problems, the PISO algorithm modified for the TFM equations was selected for its implementation:

Algorithm: PISO algorithm in TFA solver

begin *Momentum predictor*

Solve the momentum equation using the previous time step pressure solution p^o and the previous time step edge flux E^o. The result is an approximation of the mean velocity $\overline{\mathbf{u}}$.

for *number of corrections* **do**

begin *Pressure solution*

Calculate edge fluxes E using the mean velocity $\overline{\mathbf{u}}$ to assemble the $\mathbf{H}(\overline{\mathbf{u}})$ term.

Solve continuity equation. The result is the film height estimate h.

Calculate the pressure solution p based on the film height estimate h.

begin *Explicit velocity corrector*

Correct the mean velocity $\overline{\mathbf{u}}$ using the pressure solution.

The velocity correction consists of two parts–the explicit correction based on the pressure gradient $\nabla(p)$ and the implicitly transported influence of corrections of neighbouring mean velocities, the $\mathbf{H}(\overline{\mathbf{u}})$ term.

The later, $\mathbf{H}(\overline{\mathbf{u}})$ term, contains coefficients dependent on the velocity fluxes due to the linearisation of the convection term. It would be possible to additionally recalculate these coefficients as the new set of conservative fluxes is obtained during the pressure solution. But this is not done in OpenFOAM® and coefficients are recalculated first in the next momentum predictor step. The reasoning behind is the higher emphases on the pressure-velocity coupling as on the non-linear coupling.

The algorithm is not under-relaxing solution of the solved equations and is bound to small Courant number, Appendix B.1.3, ($C < 1$). The number of correction loops suggested by Issa is 2.

The algorithm has an additional feature in avoiding the pressure checker-board patterns present in the collocated meshes, reported by Versteeg and Malalasekera[107] or Ferziger and Perić[31], due to the film height h being solved at the centroid of the control area while the velocity fluxes E are solved at control area interfaces, the edges.

5.3.5 Outlet

The physical domain boundary coincides with the edges of the computational domain. These edges form a computational domain boundary. It is here, at the computational boundary edges, where the boundary conditions have to be prescribed.

The *physical boundary condition* at the outside edge of the disc is an *outlet*. The associated *numerical boundary condition* for both continuity and momentum equations at the outlet is a Neumann, or fixed gradient, boundary condition prescribing a zero gradient value.

The fixed gradient boundary condition is implemented as an inner product of the gradient and the outward pointing unit normal at the boundary edge b

$$\left(\frac{\mathbf{l}}{\|\mathbf{l}\|} \cdot \nabla\phi\right)_b = g_b \tag{5.26}$$

where g_b represents the gradient value at the boundary edge b.

5.3.6 Inlet

So far the other physical boundary condition, an *inlet*, was not mentioned. The inlet brings the fluid flow on the disc. Two options for the inlet implementation were considered in the case of the TFA solver due to the requirement of the dynamic inlet.

The first possibility is a classic approach of the inlet implementation in the form of the computational domain border, typically associated with a Dirichlet, or fixed value, numerical boundary condition prescribing the velocity. That would require an introduction of the computational domain border in the inlet shape of the inlet, basically a cut-out, into the computational mesh. The advantage would be an alignment of border edges with the inlet shape. However, the disadvantage would be a huge computational overhead of the mesh manipulation imposed on the solver as the inlet will change its position.

The second option is a direct manipulation of the solution in the selected discretisation cells of the inlet area prescribing the solution achieved by other means. The disadvantages are an non-sharp inlet resolution and reliance on others means for the inlet solution, for example 3D VoF simulation. The advantage is a dynamic inlet implementation without mesh manipulation.

Considering that the TFA solver is focusing on the high-performance, the second option was selected for the implementation. Therefore there is no numerical boundary condition at the inlet in the classical sense.

An important detail has to be pointed out yet, the influence of the surrounding

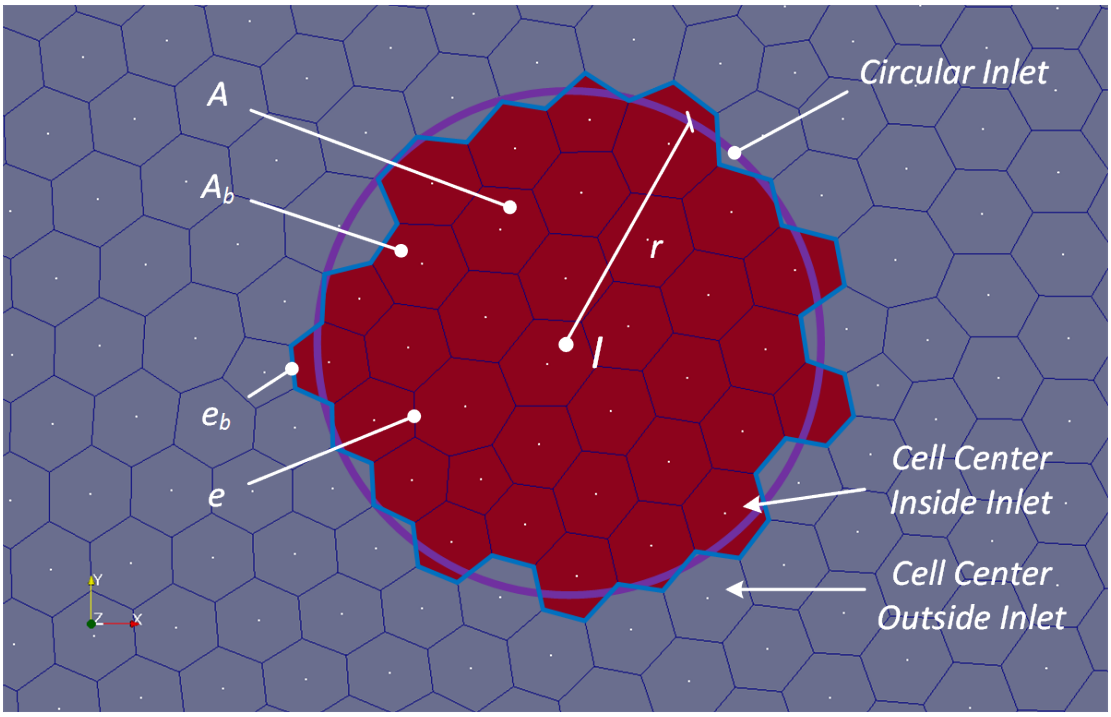

Figure 5.5: Inlet: Real inlet geometry

fluid film on the inlet flow. In reality there is a feedback from the film flow into the inlet as both flows interact in the impingement area. However, that is not the case in the current implementation. It is assumed that the inlet influence is dominant and the film flow influence on the inlet can be neglected.

5.3.6.1 Inlet Discretisation

The inlet is thought to have a circular shape, an approximation of the impinging jet contact area or a disc collar, defined by its centre point I and radius r, see figure 5.5.

The inlet area is a set of inlet control areas A_P whose centre points P lay within the inlet circle

$$\|P - I\| < r \tag{5.27}$$

The inlet control areas are a subset of the existing FA solution domain discretisation and can be easily selected or deselected during the runtime.

The edge that is connected to only one inlet control area is called a *border edge* e_b. The inlet border is a set of all border edges. The control area that contains at least one border edge is called a *border control area* A_b.

5.3.6.2 Prescribed Inlet Solution

The solution in the inlet area has to be prescribed by other means, for example by the 3D VoF simulation of the impingement or by measurements, as it cannot be resolved by the TFM model.

In order to prescribe the solution ϕ at the inlet control area A_P to the inlet value ϕ_I, the discretized general transport equation 5.17 of every discretisation cell A_P in the inlet area is manipulated into the form

$$\begin{aligned} a_P \phi_P^n &= R_P \\ R_P &= a_P \phi_I \end{aligned} \tag{5.28}$$

where a_P is the diagonal coefficient of the A matrix in the linear system of equations 5.18 and R_P is the cell source term.

Because the value of the discretisation cell ϕ_P itself depends on the values of its surrounding ϕ_N, the discretisation cells A_P at the inlet cells surrounding are corrected by removal of the inlet cells' influence

$$a_P \phi_P^n + \sum_N a_N \phi_N^n = R_P - \sum_I a_I \phi_I \tag{5.29}$$

where I denotes the neighbouring cells belonging to the inlet and a_I is the inlet cell coefficient.

The procedure effectively sets the value of the solution in the control area centroid and removes the control area corresponding equations out of the linear equation system. As a result, only the inlet border control areas A_b have an influence on the solution. The inner inlet cells are for the film solution irrelevant.

5.3.6.3 Mass Flow Rate Correction

One of the disadvantages of the selected inlet implementation is the non-sharp inlet border. The circumference of the circular inlet differs from the inlet border length along the border edges e_b what leads to the discrepancy between expected and effective mass flow.

The mass flow rate through the inlet border Q_I is given by a sum of mass flow rates through the inlet border edges

$$Q_I = \sum_{e_b} E(h)_{e_b} \tag{5.30}$$

where film height h is interpolated on the border edge.

The mass flow rate correction factor corr_Q in the inlet area is then a ratio of the

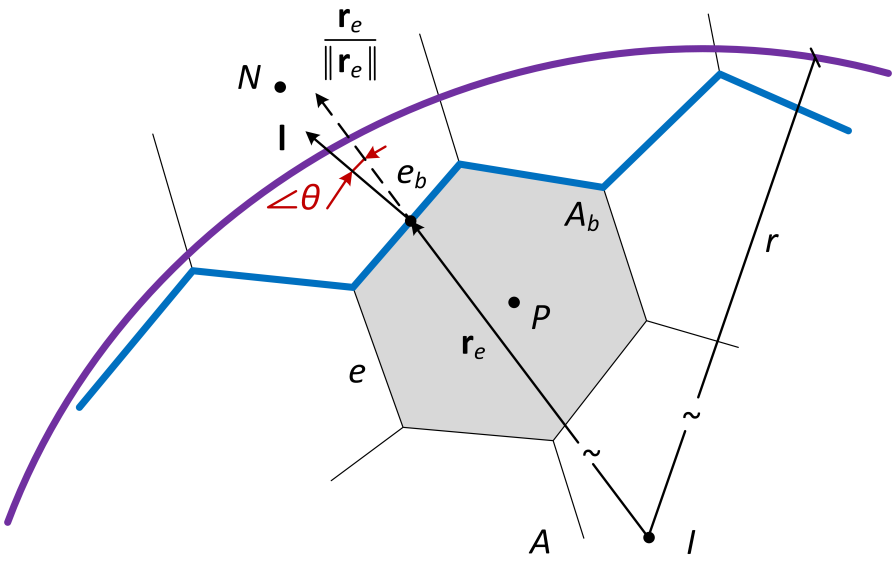

Figure 5.6: "Crown cap"

expected mass flow rate Q and the effective inlet flow rate Q_I

$$\text{corr}_Q = \frac{Q}{Q_I} \tag{5.31}$$

The correction factor is 1, if the expected and effective flow rates are equal. If the effective flow rate is higher as the expected one, the correction factor is < 1, otherwise it is > 1.

The flow rate correction factor corr_Q is applied to the mean velocity $\overline{\mathbf{u}}$ in all control areas A_P in the inlet area

$$\overline{\mathbf{u}}_P^{\text{corr}} = \text{corr}_Q \, \overline{\mathbf{u}}_P \tag{5.32}$$

where the superscript corr denotes the corrected value in the same time level.

5.3.6.4 "Crown Cap"

Another negative effect stemming from the non-sharp inlet border is a misalignment of the inlet border edges e_b against the circular inlet. The inlet border misalignment contributes to a higher non-orthogonality in the numerically sensitive area and introduces an additional radial displacement error, see figure 5.6. The non-sharp inlet border resemblance to a crown cap named the problem.

The edge correction factor corr_r of the radial displacement error is defined by a ratio of the circular inlet radius r and the distance, also called *edge-to-inlet radius*, between the edge centre and the inlet centre I as

$$\text{corr}_r = \frac{r}{\|\mathbf{r_e}\|} = \frac{r}{\|e - I\|} \tag{5.33}$$

If the edge centre is placed on the inlet circle, the correction factor is 1. The edge centre outside of the circular inlet has the correction factor < 1 and inside > 1.

The edge correction factor corr_θ of the edge non-orthogonality evaluates the angle θ between the edge length vector $\mathbf{l}$ and the edge-to-inlet vector $\mathbf{r}_e$

$$\mathrm{corr}_\theta = \left| \frac{\mathbf{r}_e}{\|\mathbf{r}_e\|} \cdot \frac{\mathbf{l}}{\|\mathbf{l}\|} \right| \tag{5.34}$$

The correction factor is 1, if the edge is orthogonal toward the inlet outflow, otherwise it is < 1.

The edge correction factors evaluated at the border edges e_b have to be applied to the mean velocities $\overline{\mathbf{u}}$ stored at the centroids P of the inlet border control areas A_b. Further it has to be remembered that every border control area A_b has at least one border edge e_b.

Therefore, the edge correction factors are applied proportionally to the number of the border edges e_b to the every border control area A_b in the inlet

$$\overline{\mathbf{u}}_P^{\mathrm{corr}} = \left[1 + \frac{\sum_{e_b} (\mathrm{corr}_r \, \mathrm{corr}_\theta \, \mathrm{bvf} - 1)}{N_{e_b}} \right] \overline{\mathbf{u}}_P \tag{5.35}$$

where the superscript corr denotes the corrected value in the same time level, N_{e_b} is the border edge count of the corrected border area A_b and the correction is scaled by an empirical boundary velocity factor bvf.

An uncorrected flow around the inlet is full of inhomogeneities in the flow field, see figure 5.7. The higher velocities at the inlet boundary areas are directly connected to the increased downwind film heights. The inhomogeneity in the inlet border velocities along the inlet edge can be clearly observed. These numerical artifacts strongly distort the solution and lead to an unrealistic form of the hydraulic jump.

The application of the border edge misalignment correction improves the situation a little bit, see figure 5.8. In this case the empirical velocity boundary factor bvf was set to neutral value of 1, what leaves the correction only on the correctors corr_r and corr_θ. The velocities around the inlet border are more homogeneous as before and some of the flow artifacts, especially on the inlet right side, are nearly gone. The hydraulic jump still shows strong distortion but its peak value is already lower opposite to the uncorrected flow.

The “crown cap” correction is going the right direction; however, its magnitude is not fitting the problem. The two presented cases illustrate the motivation for the introduction of the empirical factor bvf that represents an unknown dependency in the correction scaling.

Increasing the boundary velocity factor bvf to value 2.5 removes the majority of the artifacts, see figure 5.9. The hydraulic jump has no unrealistic peaks anymore and

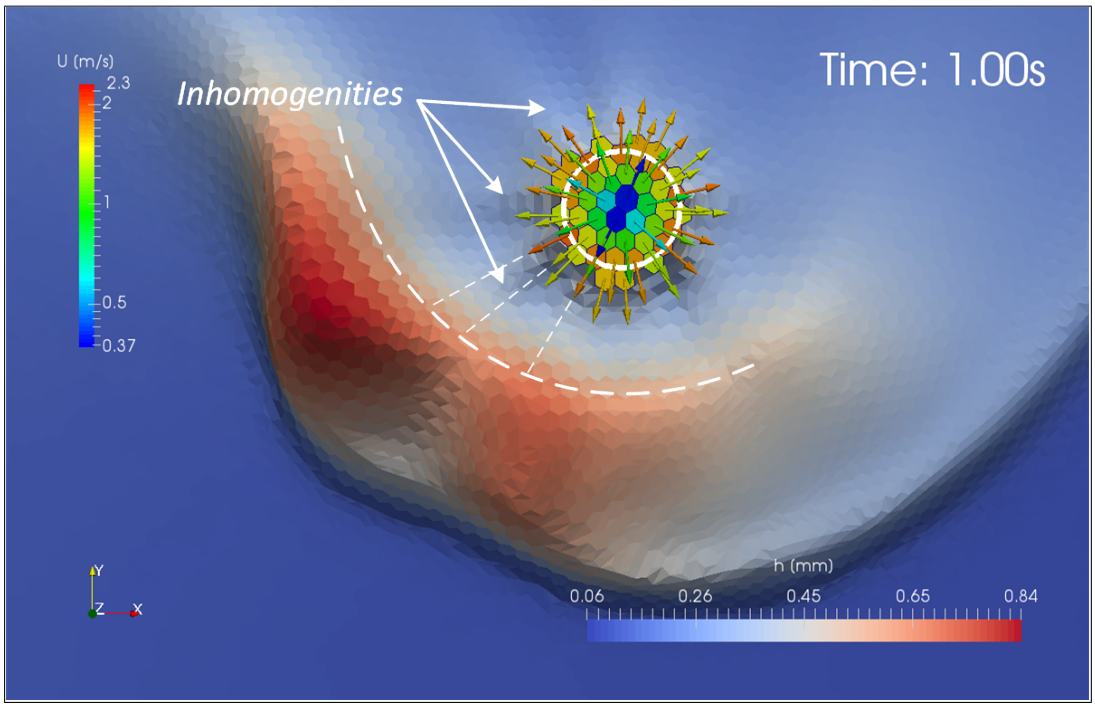

Figure 5.7: "Crown cap" (uncorrected): Strong flow artifacts and inhomogeneities induced by the misalignment of the inlet border edges against the circular inlet in its uncorrected form

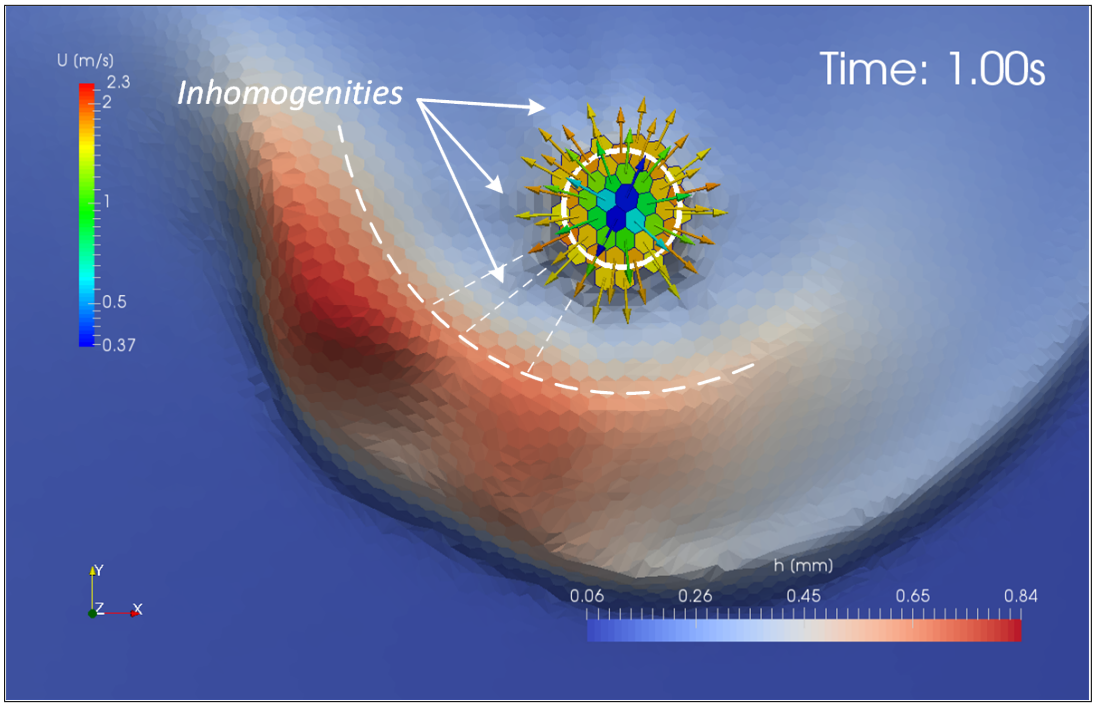

Figure 5.8: "Crown cap" (undercorrection): Neutral value of bvf = 1 leaves the correction only on the non-orthogonal and radial correction factors; artifacts and flow inhomogeneities are still present albeit weaker

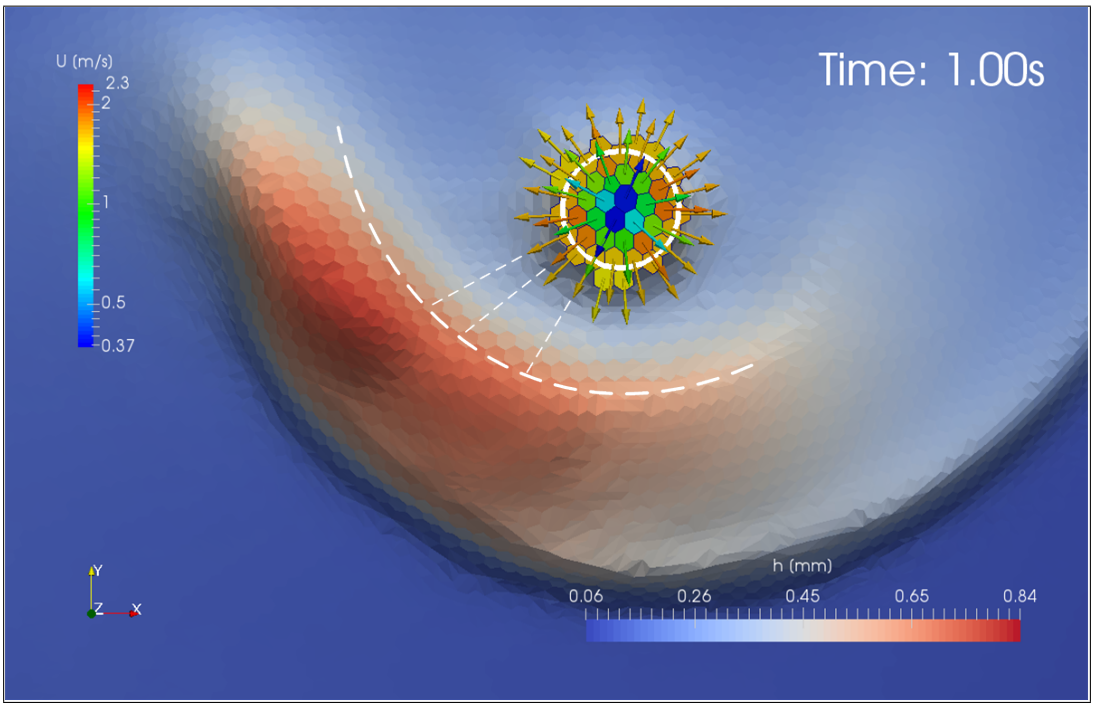

Figure 5.9: "Crown cap" (correction): Balanced correction factor bvf = 2.5 properly corrects the flow rate of misaligned border edges and removes the majority of flow artifacts

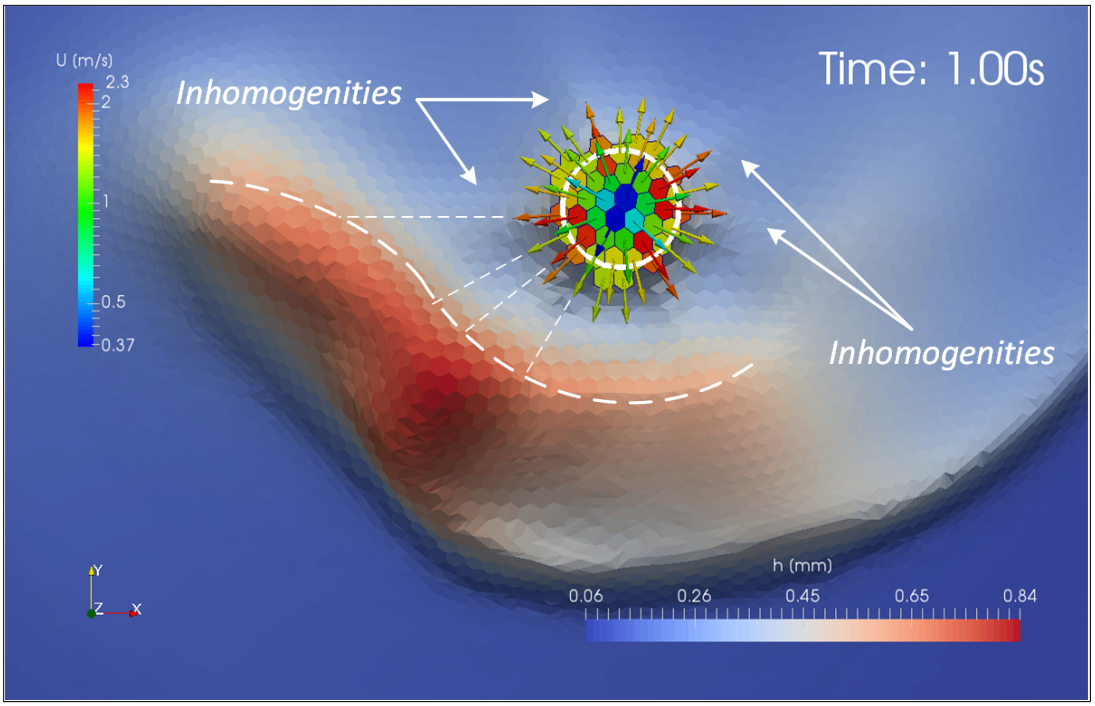

Figure 5.10: "Crown cap" (overcorrection): High correction factor bvf = 5 introduces new extremes into the inlet border area and induces new artifacts and inhomogeneities back into the flow

forms a rather uniform wave in the flow. The inlet surrounding has uniform film height without induced flow arms. Very noticeable is the change of the inlet border velocities which are very even. Note the sudden increase in the velocities of the second inlet cell row just behind the inlet border cells. It should be remembered that only the cells in the inlet border area influence the outside solution as the inner cells are removed from the linear equation system.

A further increase of the empirical factor bvf to value of 5 does not bring an improvement but new artifacts. The inlet border area suddenly contains new velocity extremes and the second row of the cells just behind the inlet border cells shows an amplification of the previous extreme velocity values. The hydraulic jump develops a new peak in the location of the hydraulic jump low point in the uncorrected case. The inlet surrounding shows new clearly visible flow arms.

The observations suggest that the boundary velocity factor bvf might be connected to the mesh cell size or there is a missing scaling factor in the radial error corrector corr_r that manifests itself through the pulling of extremes towards the inlet centre. The bvf factor could be, for example, linked to the ratio of inlet radius and diameter of a circular approximation of the mean cell size. However, for the time being the boundary velocity factor bvf is realised as a case parameter only.

5.3.6.5 Inlet Profiles

In reality, the inlet solution varies dependent on the real inlet flow. The inlet flow is never regular. It is influenced by interactions with the film flow and its irregularities are further enhanced by the inlet's physical imperfections. Thus the real distribution of the inlet solution values ϕ_I would have to be generally prescribed in every inlet control area individually.

However due to the implementation of the fixed solution values in the inlet area, the inner inlet control cells have no influence on the film solution. The film flow is effectively controlled only by the prescribed solution values in the inlet border control areas A_b. The distribution of the inlet values ϕ_I along the inlet border is then called an *inlet profile*. The numerical studies can often use a simplification of the real velocity distribution, an *inlet profile model*.

The inlet profile models always calculate the expected inlet values ϕ on the circular inlet and map them on the the inlet values ϕ_I through the inlet area, both in the border and the inner cells. Due to the displacement of the centroids P of the inlet control areas A_P against the circular inlet, the calculated values ϕ are simply scaled by their control area centroid relative radial position to the inlet centre I

$$\phi_I = \left(\frac{\|P - I\|}{r} \right) \phi \tag{5.36}$$

The scaling is applied, out of simplicity, to all inlet control areas. As a result of the scaling, the centroid coincident with the inlet centre point will have prescribed the value 0 and values linearly increase towards the circular inlet, where they have the calculated value ϕ.

In fact, the handling of the inlet values ϕ_I in the inlet area could already caught an attention in the figures illustrating the "crown cap" problem, where the most simple inlet profile model with the constant inlet value along the inlet border, so called *constant inlet profile*, is used.

The constant inlet profile model is defined by the expected flow rate Q and the film height h, the velocity at the circular inlet is given by

$$\overline{\mathbf{u}} = \frac{Q}{2\pi r h} \tag{5.37}$$

The model is suitable especially for central impingement cases where a solution can be prescribed based upon a 2D axisymmetric VoF simulation. Surprisingly enough, such a simplification is often sufficient even for general cases with an excentric impingement.

The inlet profiles can have more complicated forms and even mimic an influence of the film flow on the inlet border area by varying the inlet solution values along the inlet border.

A *linear inlet profile* family varies either the expected inlet film height h or the expected inlet mean velocity $\overline{\mathbf{u}}$ values while keeping the other expected inlet value constant. The implementation of the linear inlet profile takes the constant inlet profile as a starting point. A tilting axis t passing through the inlet centre I with a defined offset angle against the x-axis is placed in the constant inlet value plane. The plane of the constant inlet values is then tilt around the tilting axis t by predefined slope from the interval $\langle -1, 1 \rangle$.

An example of the *linear height inlet profile* is given in the figure 5.11. The expected mean velocity inlet value $\overline{\mathbf{u}}$ is kept constant and calculated via equation 5.37. The tilting axis t is passing through the inlet centre point and is parallel to the x-axis having offset angle of 0°. The expected inlet film height values laying on the intersection of the tilting axis and the circular inlet have the prescribed value of the film height h and are linearly rising along the plane toward the inlet south to the inlet value of $(1 + \text{slope})h$ and falling along the plane toward the inlet north to the inlet value $(1 - \text{slope})h$. The inlet values plotted along the circular inlet circumference illustrate the linearity of the inlet value scaling.

The *linear velocity inlet profile* is presented in the figure 5.12. It is the expected film height h that is kept constant along the circular inlet in the case of the linear velocity profile. The tilting axis t is placed as in the example before passing through the circular inlet centre while being parallel to the x-axis, that is the offset

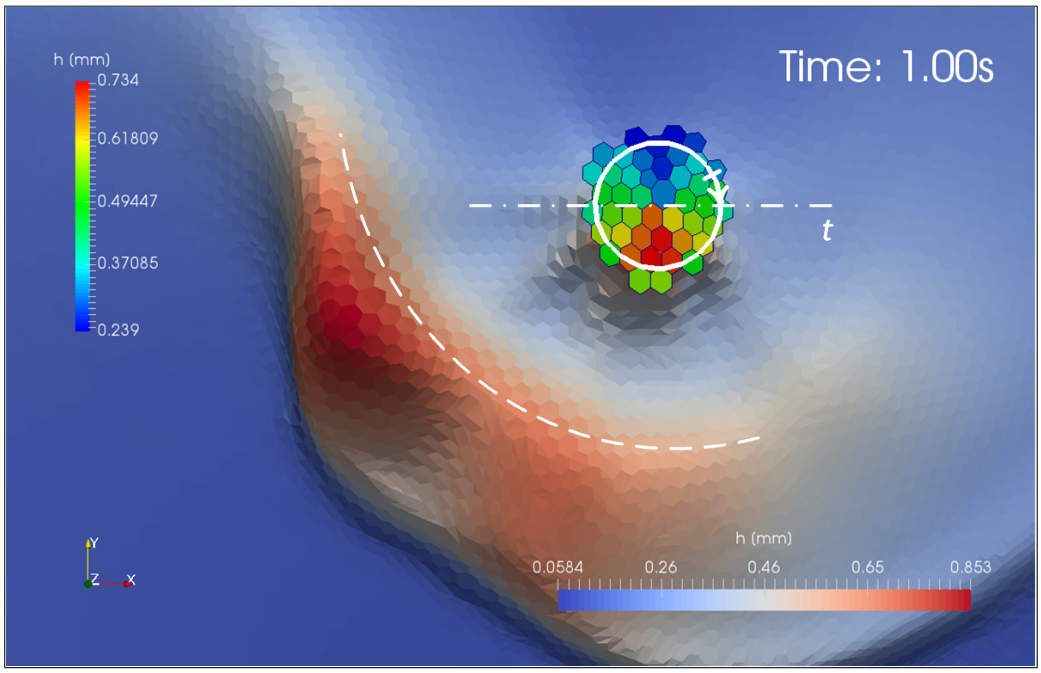

(a) Linear inlet height profile: $Q = 1.5$lpm, $h = 0.5$mm, offset $= 0°$, slope $= 0.5$

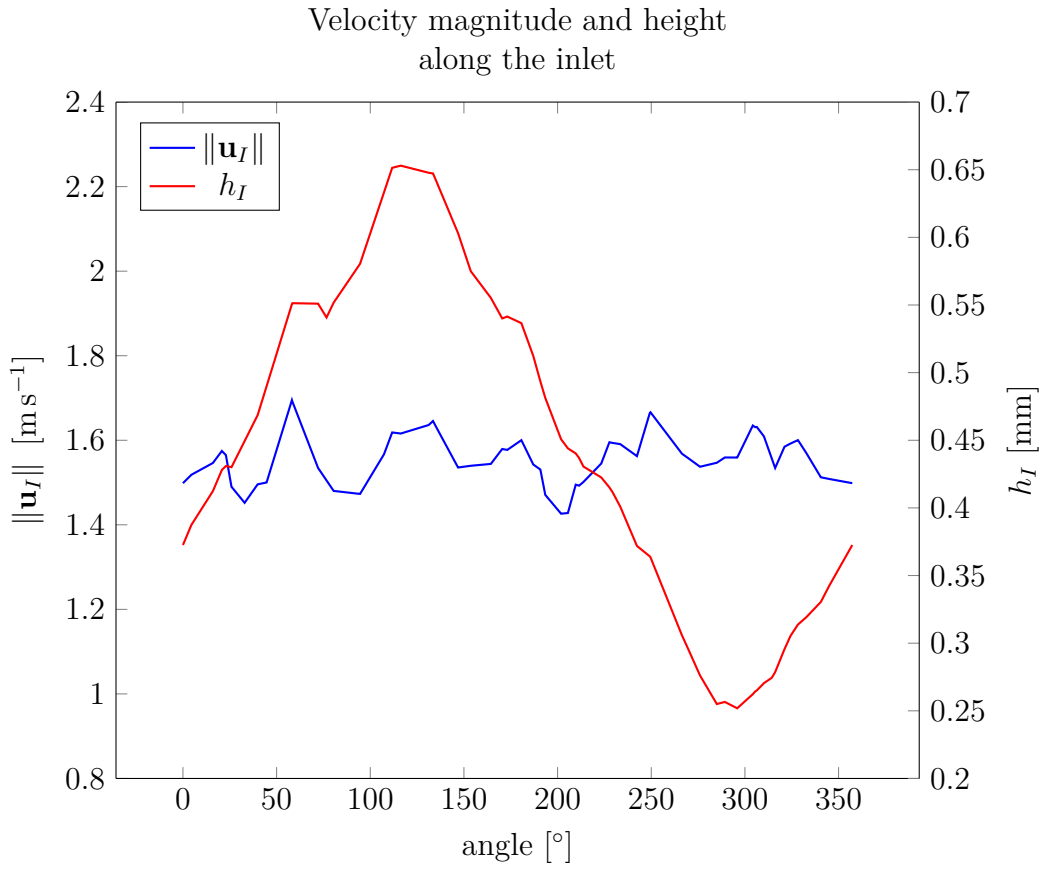

Figure 5.11: Linear inlet height profile

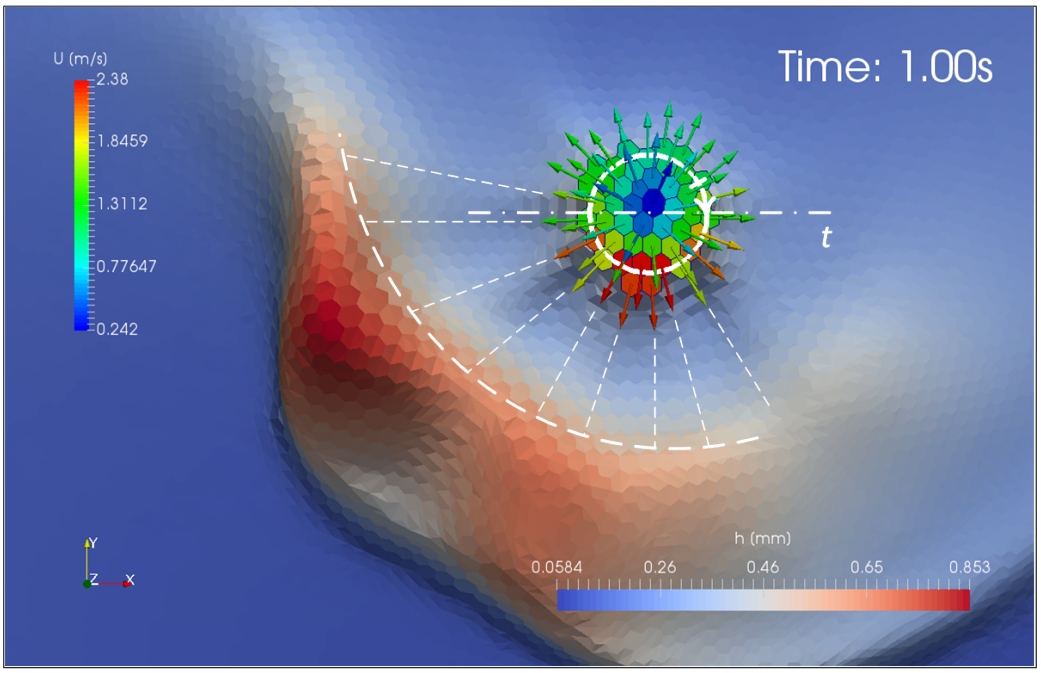

(a) Linear inlet velocity profile: $Q = 1.5$lpm, $h = 0.5$mm, offset $= 0°$, slope $= 0.5$

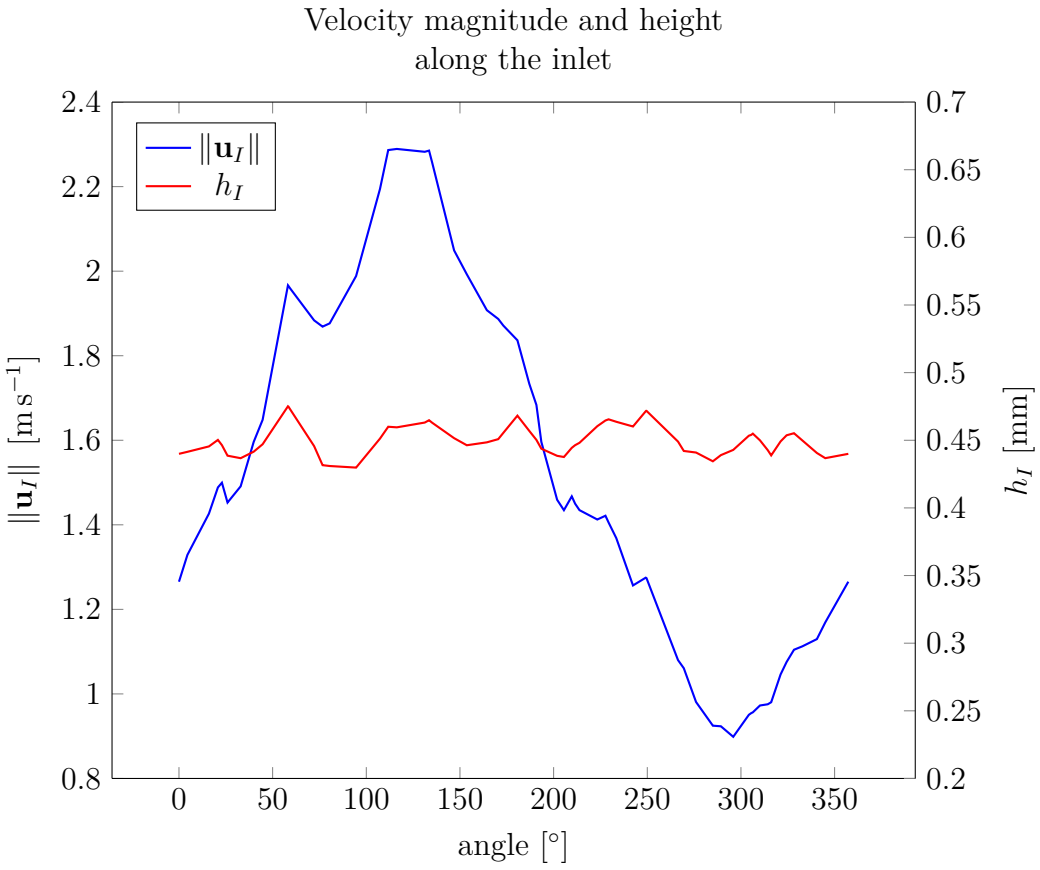

Figure 5.12: Linear inlet velocity profile

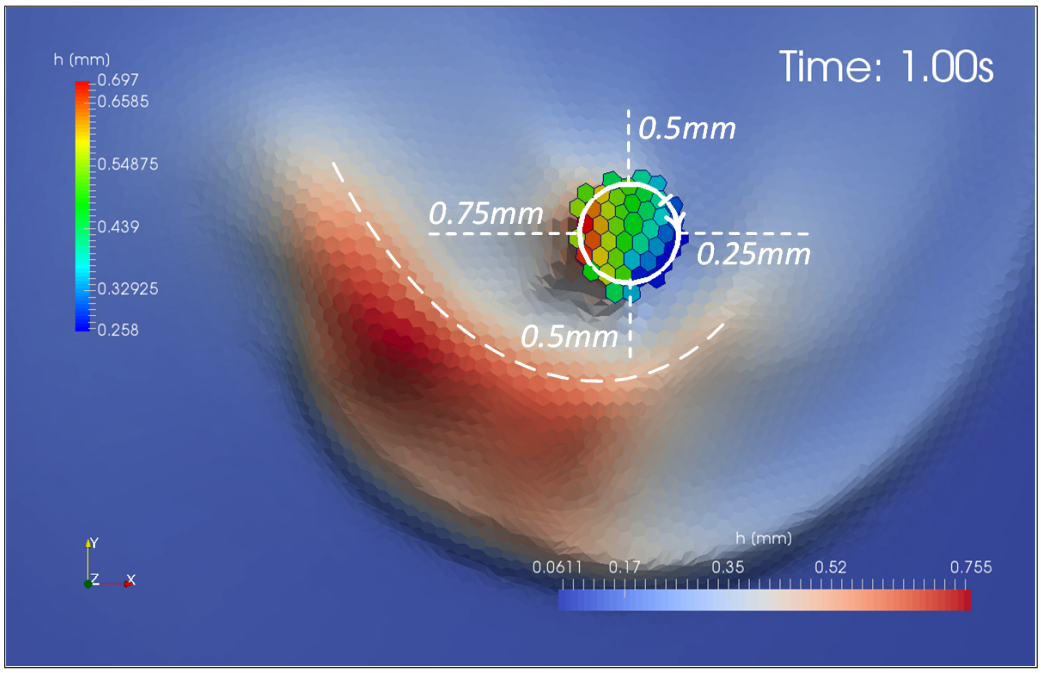

(a) Radial inlet height profile: $Q = 1.5\text{lpm}$, $h = 0.5\text{mm}$

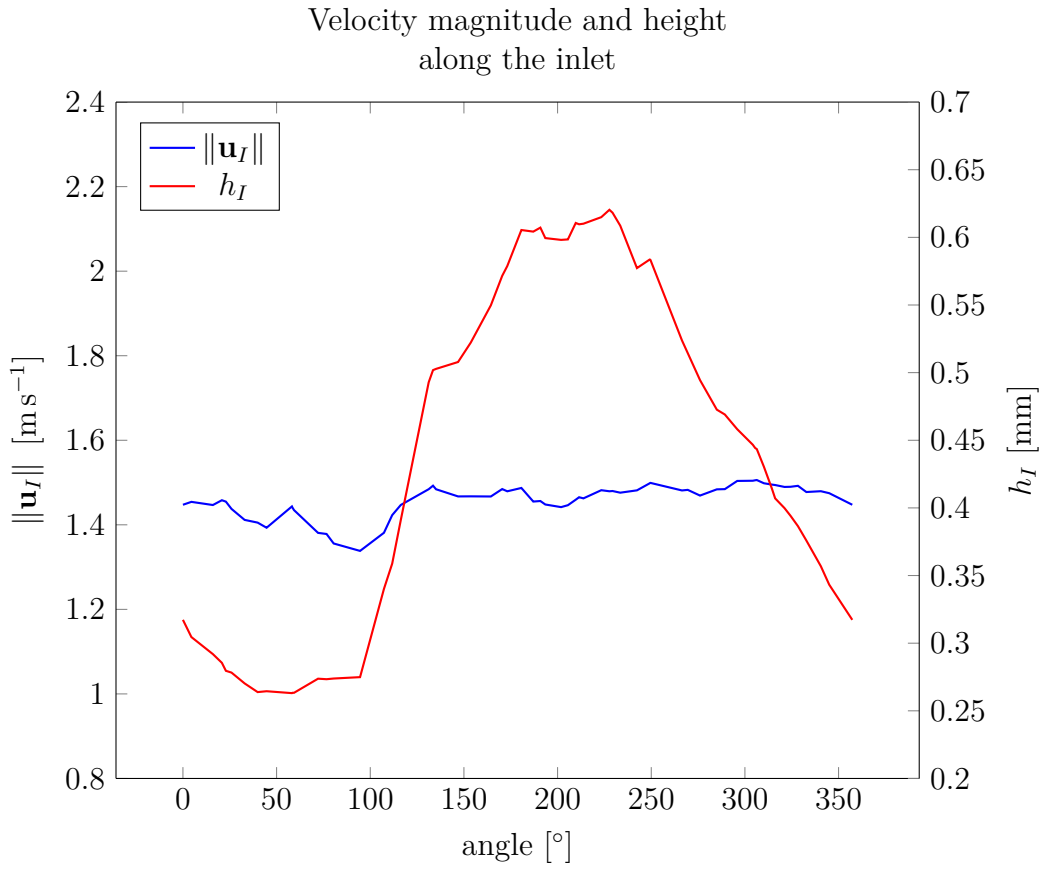

Figure 5.13: Radial inlet height profile

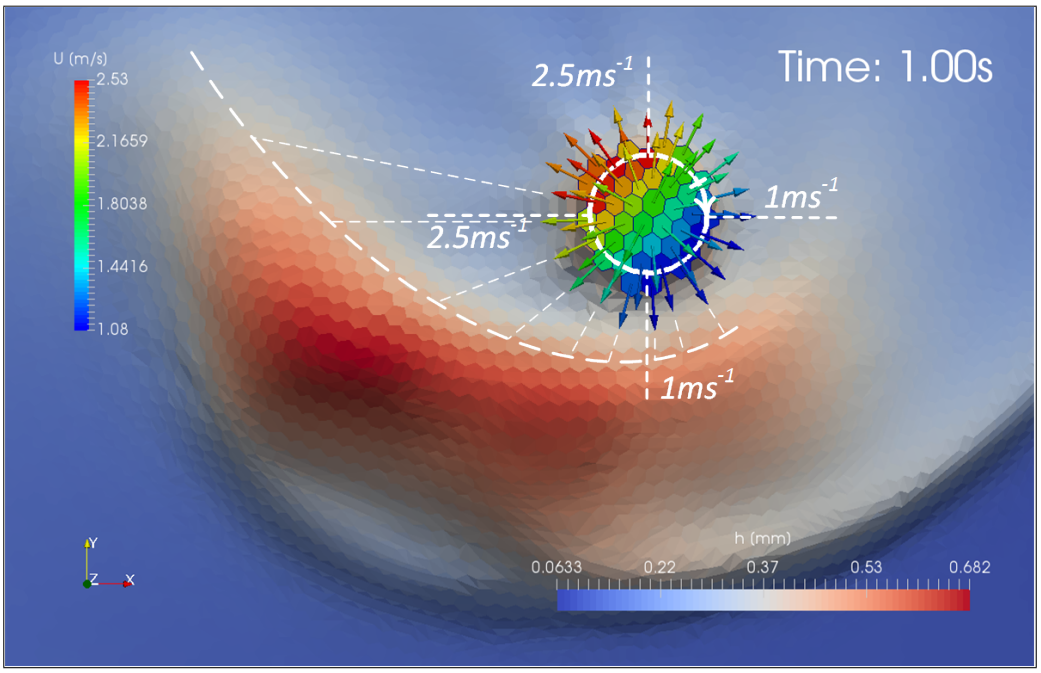

(a) Radial inlet velocity profile: $Q = 1.5\text{lpm}$, $h = 0.5\text{mm}$

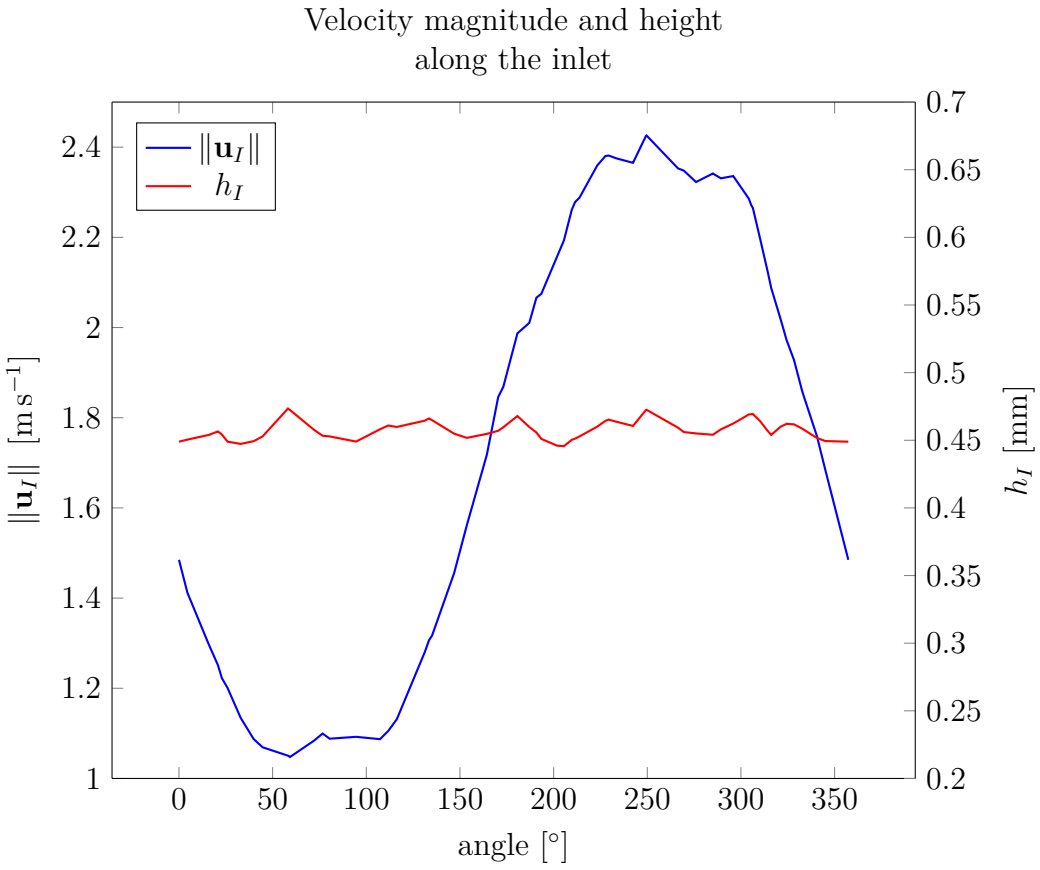

Figure 5.14: Radial inlet velocity profile

angle is 0°. The expected mean velocity $\overline{\mathbf{u}}$ varies along the circular inlet with its maximum at the inlet south and the minimum in the north. The expected mean velocity $\overline{\mathbf{u}}$ values at the intersection of the tilting axis t with the circular inlet are calculated using the equation 5.37.

The last implemented inlet profile is a *radial inlet profile*. The radial inlet profile model allows to prescribe arbitrary expected values ϕ along the inlet border in the form of a table of tuples (<angle>, <value>). The table inlet values are then interpolated by a piecewise linear interpolation. It is important to note that both expected inlet values, the mean velocity $\overline{\mathbf{u}}$ and the film height h, are prescribed simultaneously, thus the expected inlet flow rate Q has to be calculated.

There is an example of the *radial height inlet profile* at the figure 5.13. The expected mean velocity $\overline{\mathbf{u}}$ is constant with the value of $1.5\mathrm{m\,s^{-1}}$. The table values for the expected inlet film height h are marked in the picture along the inlet border. The north and south film height h share the value of 0.5mm. The maximal film height h of 0.75mm is in the west of the inlet and the minimum is on the opposite side at the east with the value of 0.25mm. There is a noticeable deformation of the film flow height connected to the inlet height variation, especially in the western half of the inlet area.

The last example, see the figure 5.14, presents a *radial velocity inlet profile* that is mimicking the interaction of the fluid flow with the inlet. The expected film height h is kept constant, the expected mean velocity $\overline{\mathbf{u}}$ is being varied along the circular inlet with the table values marked in the picture. Note the lower mean velocity $\overline{\mathbf{u}}$ in the south-east inlet area as the inlet outflow gets slowed down in the hydraulic jump while in the north-west of the inlet the outflow is having its maximum. The shape and the position of the hydraulic jump is clearly influenced by the inlet outflow, confirming that the inlet profiles can be used to model the film flow influence in the inlet area.

5.4 Computational Mesh

An influence of a computational mesh selection cannot not be underestimated. Unfortunately, it is not easy nor straightforward task. It is much more simple to recognise a bad mesh as to judge a good one. The bad mesh is usually a black-white decision. The judgement of a good mesh is connected to all shades of grey. There exist good meshes and better meshes.

Four different Cartesian computational meshes have been tested during the TFA solver development. The meshes have been created on the basis of a volumetric geometry model. This is a necessary evil as the FA code base uses a surface patch of a volumetric mesh in order to construct its native FA computational mesh. The mesh construction itself is therefore dictated by the need of a single high-quality

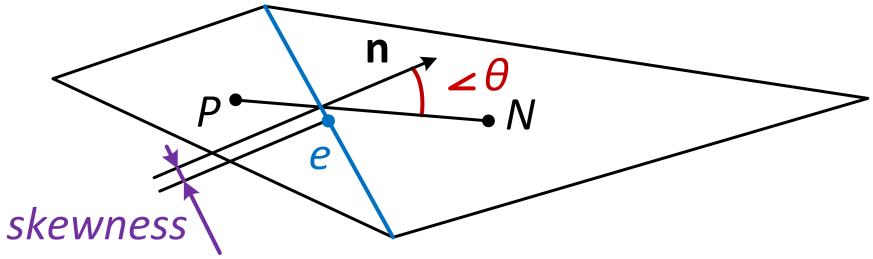

Figure 5.15: Mesh metrics

Mesh	Cell count [4]	Non-Orthogonality		Skewness
		Average	Maximal	Maximal
Circle	7168	7.6	36.02	0.565
Pave	15 423	2.952	19.25	0.554
Delaunay	14 471	23.374	61.05	1.521
Polyhedral	7605	9.668	27.077	0.276

Table 5.1: Mesh topologies and their quality criteria

surface patch and only the selection of the surface mesh topology is of importance.

A restricting side-effect of the FA workflow in the OpenFOAM® are limited tools for the evaluation of a priori *geometric mesh quality* of the FA meshes. The only real option is a utility `checkMesh` that works with the volumetric meshes and reported criteria have to be filtered out to those one relevant to the surface meshes. The selected criteria to describe the geometric mesh quality are the mesh *non-orthogonality* and *skewness*, see figure 5.15.

The mesh non-orthogonality measures the angle between the line connecting two cell centres and the normal of their common interface. The mesh non-orthogonality introduces an error into the evaluation of the cell interface gradients. Two non-orthogonality measures were taken, the average and the maximal mesh non-orthogonality.

The skewness criterion measures the distance between the intersection of the line connecting two cell centres with common interface and the common interface centre point. Large skewness negatively influences the accuracy of the interpolation.

The used surface meshing topologies–a structured *circle* topology, a non-structured *pave* topology and a *Delaunay* triangulation–gave the name to the resulting meshes. The fourth mesh, a *polyhedral* mesh, was created from the hexahedral mesh by forming polygons around its nodes using the `polyDualMesh` utility. The resulting polyhedral mesh has a honeycomb like structure. The computational meshes and their selected geometric properties are summarised in the table 5.1. The meshes characteristic features are illustrated in the figure 5.16.

[4]The cell count differences between meshes are caused by equalising of an edge size used by meshing algorithm.

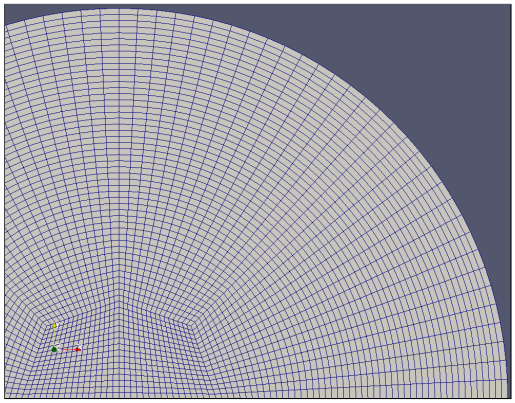

(a) Circle topology

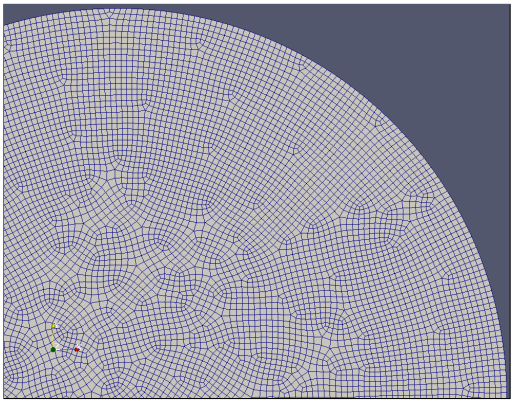

(b) Pave topology

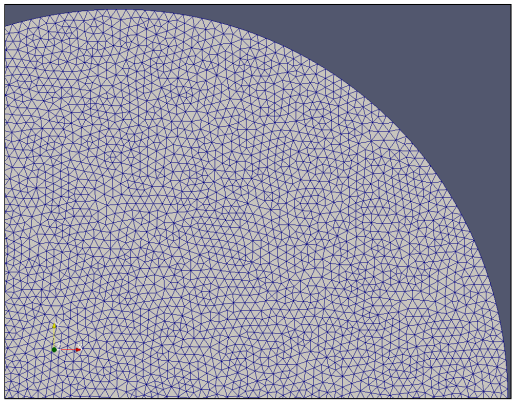

(c) Delaunay triangulation

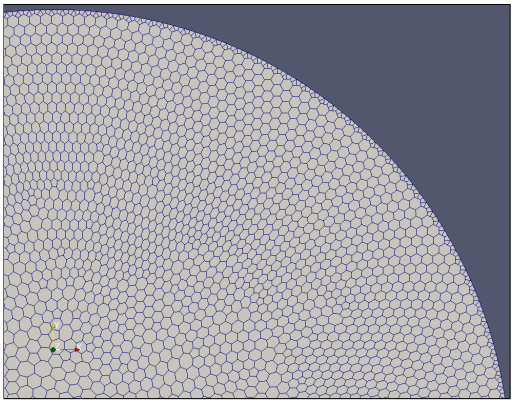

(d) Polyhedral mesh

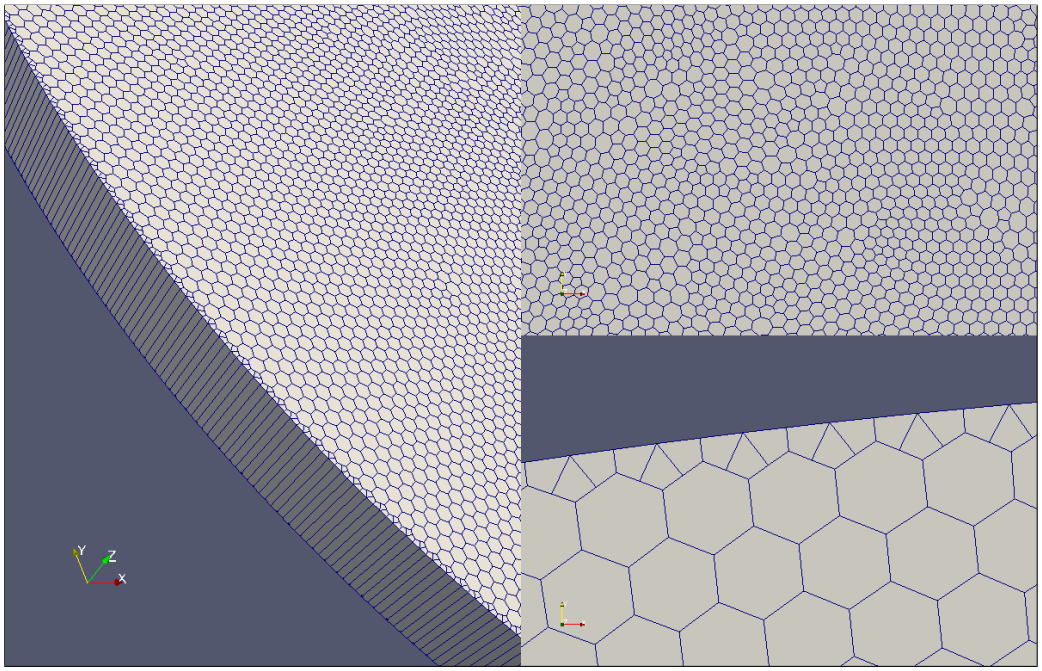

(e) Polyhedral mesh in detail

Figure 5.16: Meshes

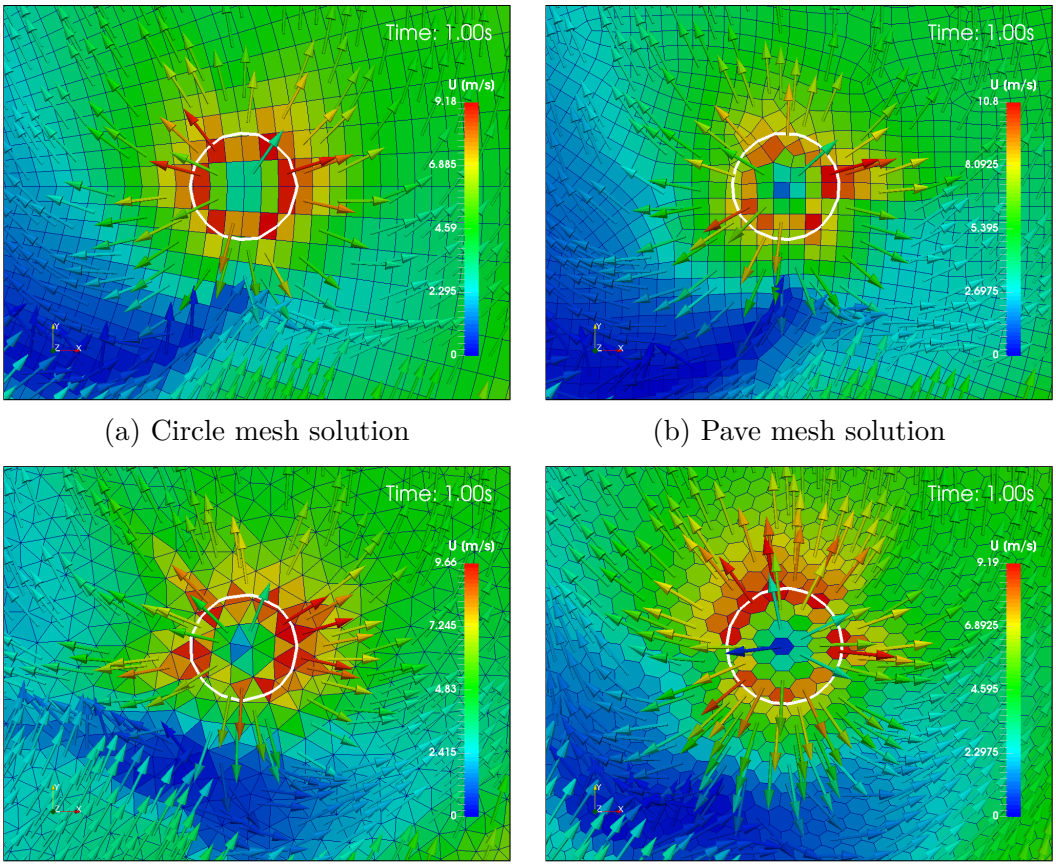

(a) Circle mesh solution

(b) Pave mesh solution

(c) Delaunay mesh solution

(d) Polyhedral mesh solution

Figure 5.17: Mesh artifacts: Same excentric case using different meshes

It is very important to point out that the mesh quality cannot be judged based on its geometric quality only. While the geometric quality provides a general guidance on the mesh, it might say a little about the mesh connection to the solution accuracy. Thus mesh has to be evaluated to make sure it leads to realistic solutions.

A single excentric simulation case was used in order to compare solutions in the numerically sensitive inlet area on all four meshes, see figure 5.17. The velocity flow field shows strong numerical artifacts at the interface of two fluid flows, the film flow interacting with the inlet outflow, in the case of three meshes. The circle and pave topology both lead to highly distorted solutions at the inlet south area as the flow is highly non-orthogonal against the cell edges. The Delaunay triangulation due to a marginally better alignment of the inlet cells towards the circular inlet is able to produce differently shape solution in the inlet south area that is more realistically resolving the flow fronts. That might be surprising considering its much worse geometric properties. Only the polyhedral mesh is able to capture uniformly distributed velocities at the flow fronts. The cells of the polyhedral mesh have a favourable shape approximating a circle that keeps them aligned against

Case	Δr [mm]	ν [$m^2 s^{-1}$]	Q [lpm]	ω [rpm]
3a	0	2.87×10^{-6}	1.5	500
3b	30	2.87×10^{-6}	1.5	500
3c		1×10^{-6}		
3d	50	2.87×10^{-6}	1.5	500
3e		1×10^{-6}		

Table 5.2: Case definitions for TFA

any flow direction. This makes the polyhedral mesh superior for a dynamically moving inlet and the mesh of choice.

5.5 Simulations

The validation of the TFA solver is done by a comparison of the TFA solution against 3D VoF solution. The comparison is realised on five simulation cases that cover three different impingement regimes, see the table 5.2.

The first case, case 3a, represents a central impingement example. The cases 3b and 3c are excentric cases with a radial excentricity $\Delta r = 30$mm that still allows a full disc coverage with the fluid film. That last two cases 3d and 3e are having a strong excentricity $\Delta r = 50$mm that causes a dry spot formation at the middle of the disc.

All cases use the same volumetric flow rate Q and rotational speed ω with both parameters mimicking a configuration used in a semiconductor industry. The fluid viscosity is being varied in the excentric cases. The kinematic viscosity $\nu = 1 \times 10^{-6} m^2 s^{-1}$ corresponds to water while the value $\nu = 2.87 \times 10^{-6} m^2 s^{-1}$ refers to an etching solution Spinetch D reported by Staudegger[99].

The 3D VoF simulations, courtesy of TU Graz, were conducted using the ANSYS Fluent 12.1.2 software. The volumetric computational mesh had approximately 5 million cells in order to resolve the thin film features. The inlet in the 3D VoF simulation is static. The simulation was parallelised on the 4 CPU cores of the Intel Core i7 Bloomfield-family and simulation time for 1s of the process took about 30 days.

The 2D TFA simulations were performed with the described TFA solver implemented in the OpenFOAM® distribution `foam-1.6-extend`. The FA polyhedral surface mesh had in total of 36 886 cells. The inlet was static, a limitation imposed by 3D VoF simulation. The inlet used a constant inlet profile with a prescribed solution of the film height $h = 0.5$mm based on the 3D VoF simulation itself and the defined volumetric flow rate Q. The simulation was running on a single CPU core of the Intel Core i7 Bloomfield-family. The simulation time for 1s of

the process was about 2 hours; a speed-up of 1440 is achieved with the 2D TFA solver.

The key characteristics for comparison purposes are the film height h and the shear stress τ at the disc bottom. 3D VoF and 2D TFA solutions of both characteristics are presented in instantaneous contour plots at time $t = 1$s. The impinging jet has xz- and yz-planes placed through after ward and time averaged values of both characteristics are plotted on the planes.

5.5.1 Central Impingement

The first case 3a represents a central impingement. The 2D TFA solution, see the figure 5.18, shows a hydraulic jump formation in the close vicinity of the impinging jet. Both solutions–3D VoF and 2D TFA–develop artifacts in the hydraulic jump formation in a form of "rose petals". These artifacts are connected to the misalignment of the inlet cells. An another typical artifact, a very fine form of flow arms, can be noticed in the film height relief.

Comparing the film height and shear stress contour plots of the 3D VoF and 2D TFA, both solutions are very similar. The striking difference is only the surface waviness of the 3D VoF solution that cannot be resolved by the 2D TFA method due to the suppressed cross flow in the normal direction.

The observed surface waviness projects as well into the evaluation of the xz- and yz-plane cuts through the impinging jet. The 2D TFA solution is surprisingly well capturing the thin film thickness h even in the impingement area where the solution is expected to be invalid. A similar observation can be done in the prediction of the shear stress τ. Note the shaded zone of the plots depicting the area with a prescribed solution.

5.5.2 Excentric Impingement

5.5.2.1 Full Disc Coverage

The cases 3b and 3c represent an excentric impingement with a moderate excentricity. The radial excentricity $\Delta r = 30$mm still allows a full coverage of the rotating disc with both fluids, the etchant Spinetch D and the water.

The higher viscosity of the Spinetch D solution, the case 3b, leads to a higher height of the hydraulic jump in the 2D TFA approach, see the figure 5.21. The hydraulic jump forms its peak on the right side of the inlet outflow against the disc rotation.

Comparisons of the 3D VoF and the 2D TFA solutions show a good agreement of the film features. The height extremes in the hydraulic jump predicted by the 3D

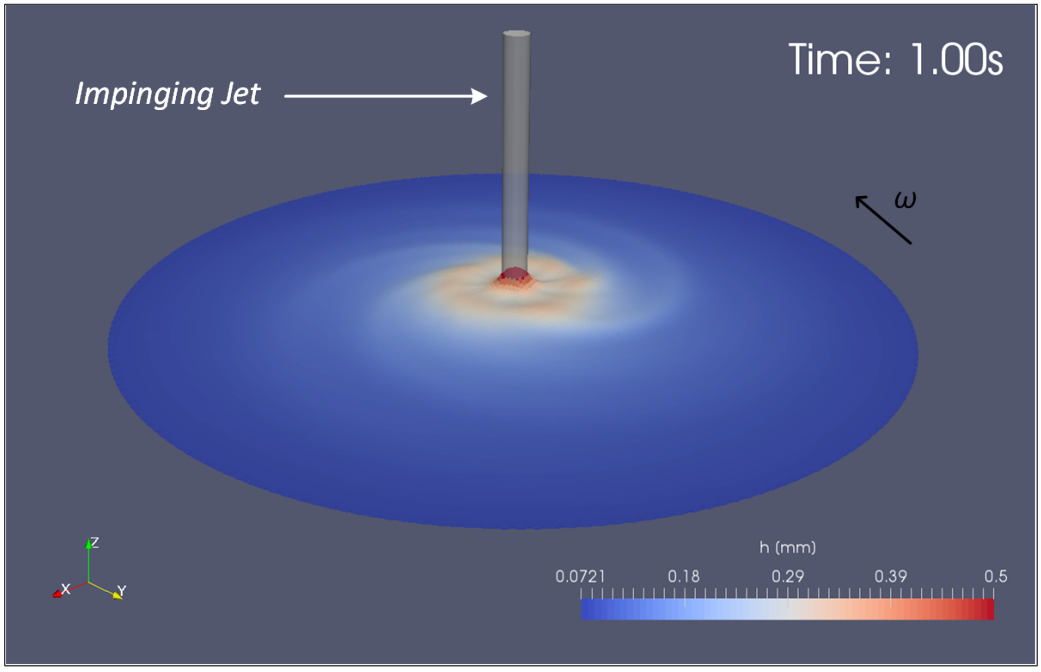

(a) Film relief (2D TFA): z-axis scaled 30×

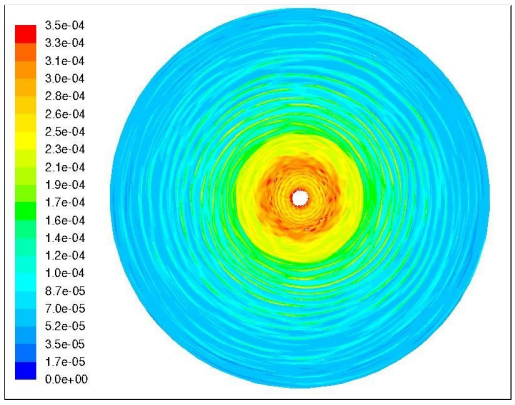

(b) Film height (3D VoF)

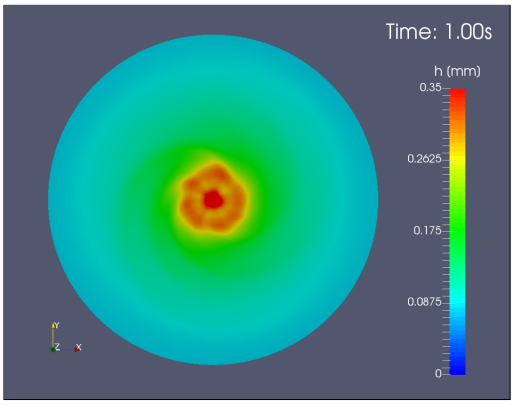

(c) Film height (2D TFA)

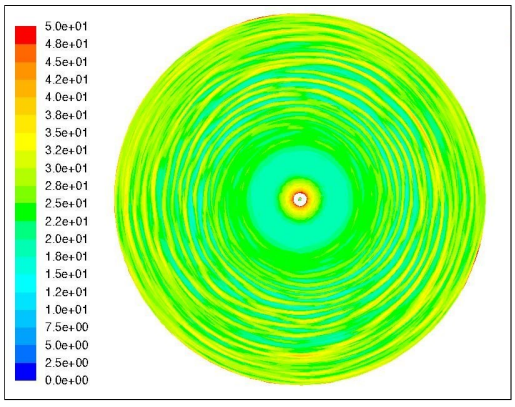

(d) Shear stress (3D VoF)

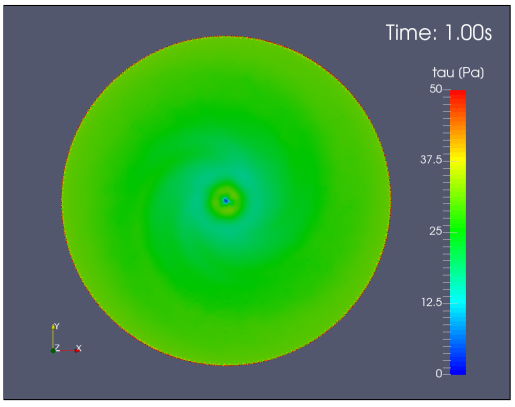

(e) Shear stress (2D TFA)

Figure 5.18: Case 3a: $\Delta r = 0\text{mm}$, $\nu = 2.87 \times 10^{-6}\text{m}^2\,\text{s}^{-1}$, $Q = 1.5\text{lpm}$, $\omega = 500\text{rpm}$; 3D VoF solution courtesy of TU Graz

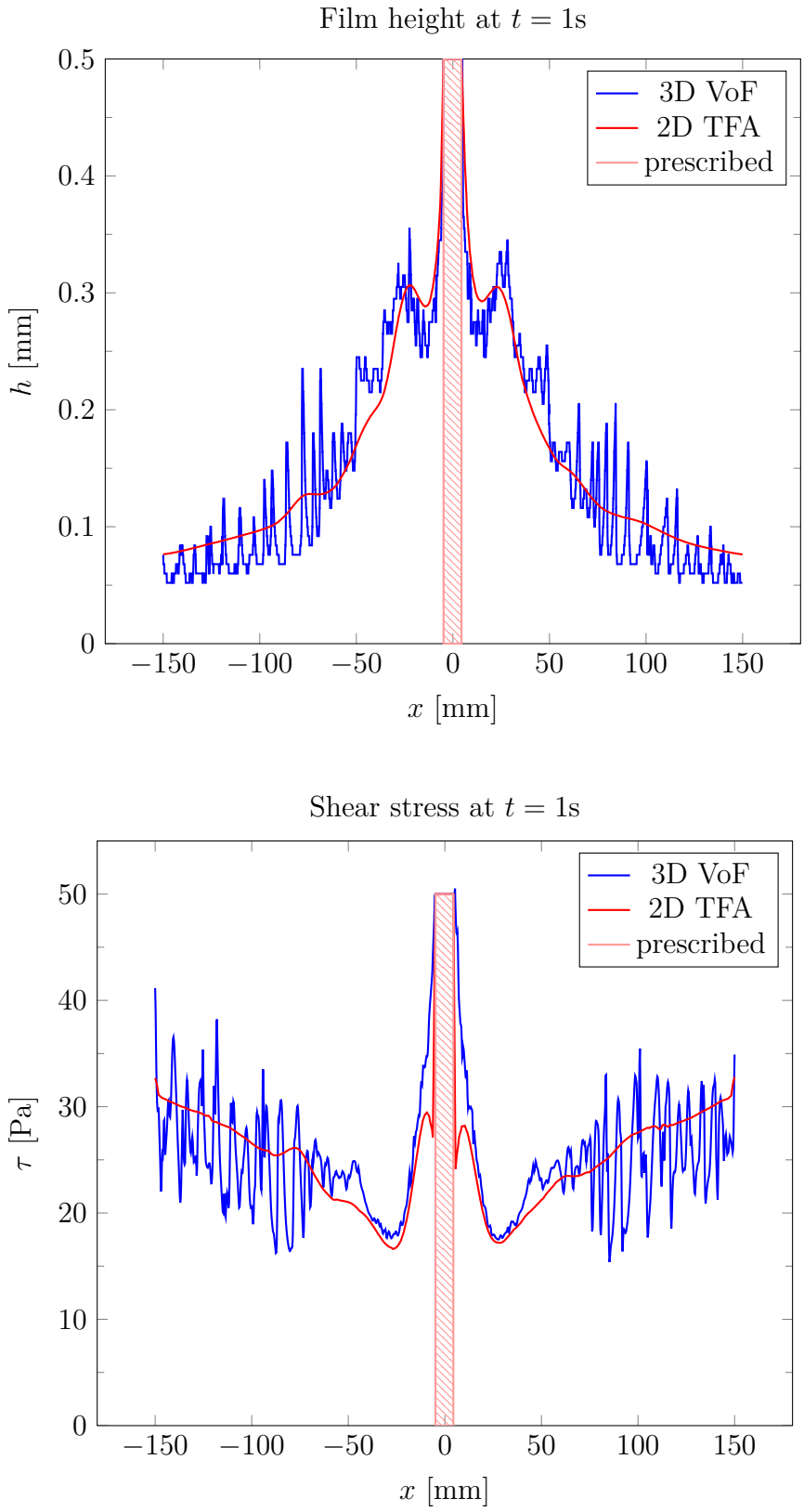

Figure 5.19: Case 3a: xz-plane through the impinging jet; 3D VoF solution courtesy of TU Graz

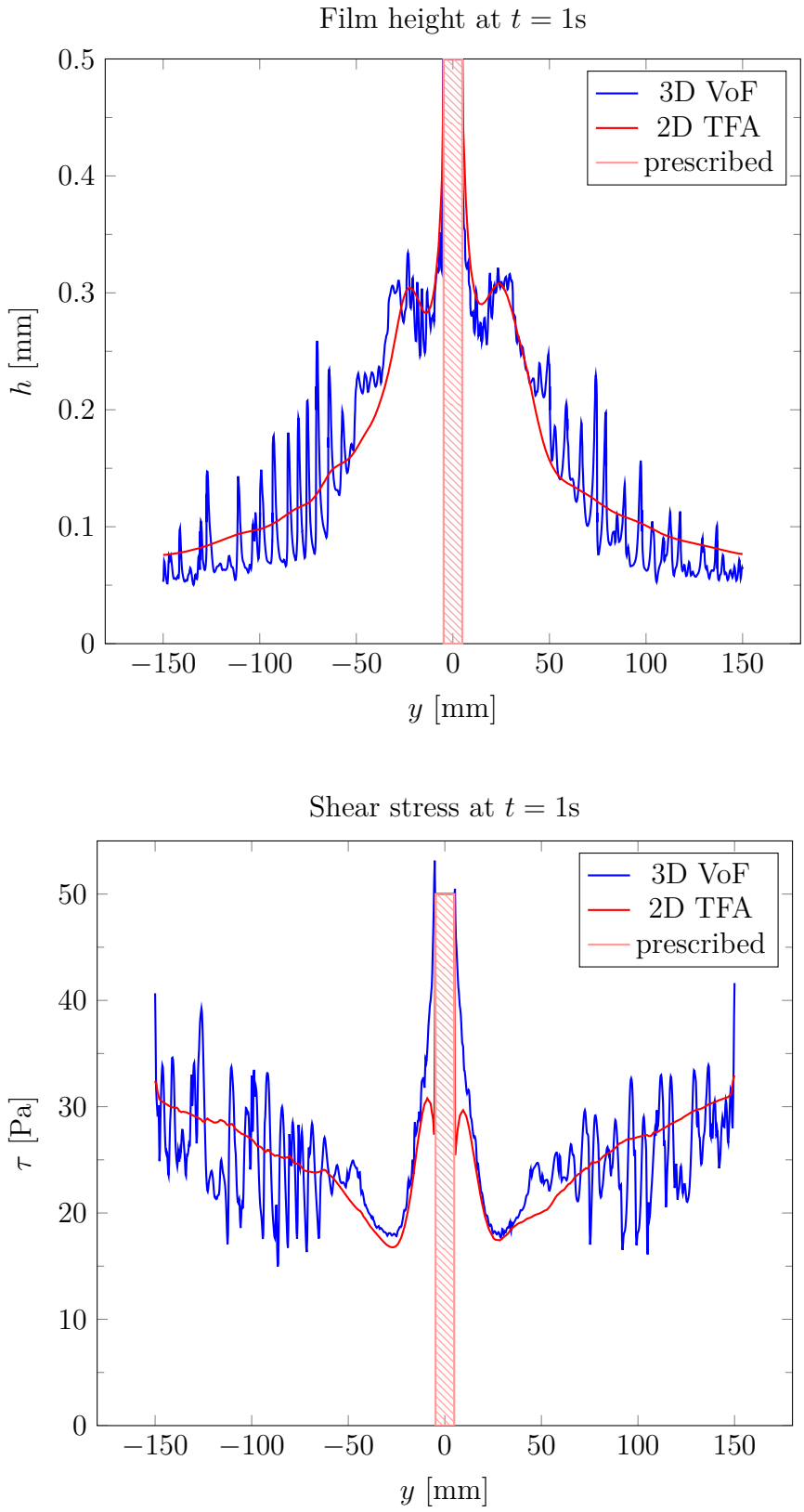

Figure 5.20: Case 3a: yz-plane through the impinging jet; 3D VoF solution courtesy of TU Graz

VoF method have the same location as in the 2D TFA solution, but scale. The same applies for the shear stress that is connected to the film thickness through the film velocity profile.

The xz- and yz-plane cuts present as well a good agreement between both, 3D VoF and 2D TFA, approaches. Very noticeable are errors in the hydraulic jump and the inlet vicinity which are not a surprise. Both zones generally represent phenomena that render some of the TFM assumptions invalid as discussed previously. Still it has to be pointed out that the mass is correctly conserved in both problematic areas and both solutions show a very good agreement, just a bit farther from the inlet influence.

The case variation with the lower fluid viscosity, the case 3c, can be seen in the figure 5.24. The lower viscosity is directly connected to the lower and a bit wider hydraulic jump solution in the 2D TFA approach. With an exception of the hydraulic jump height extremes, both methods–the 3D VoF and the 2D TFA–demonstrate the same flow features when comparing the film height and shear stress contour plots.

The comparisons by the help of cutting planes confirm the observation of the very good solution agreement seen in the contour plots. There exist only two notable differences. The first difference is the film height prediction in the xz-plane cut on the right side of the film height plot, see the figure 5.25. The area with the error is influenced by the inlet outflow and is marked by the missing feedback to the inlet itself. The second solution discrepancy is the hydraulic jump visible in the film height plot in the yz-plane cut on picture left side, see the figure 5.26.

It is assumed that errors are on the side of the 2D TFA predictions. However, the 3D VoF prediction is rising a question if the predicted abrupt, nearly vertical, increase of the film height and its scale is not influenced by some numerical error as well.

5.5.2.2 Dry Spot Formation

The last two simulation cases, the case 3d and 3e, are both having an increased radial excentricity $\Delta r = 50$mm that leads to the film discontinuity and creates a dry spot in the disc centre, see the figures 5.27 and 5.30. The size of the dry spot is directly influenced by the fluid viscosity. The higher viscosity of the etchant Spinetch D causes a bigger dry spot as the lower viscosity of the water.

There are noticeable differences between both methods–3D VoF and 2D TFA–in the dry spot prediction. The 3D VoF predicts bigger and much more pronounced dry spots opposite to the 2D TFA method. This should not be surprising though as the lack of one phase is naturally filled by the other phase in the 3D VoF method. The 2D TFA method has only one single phase and the dry spot as such would

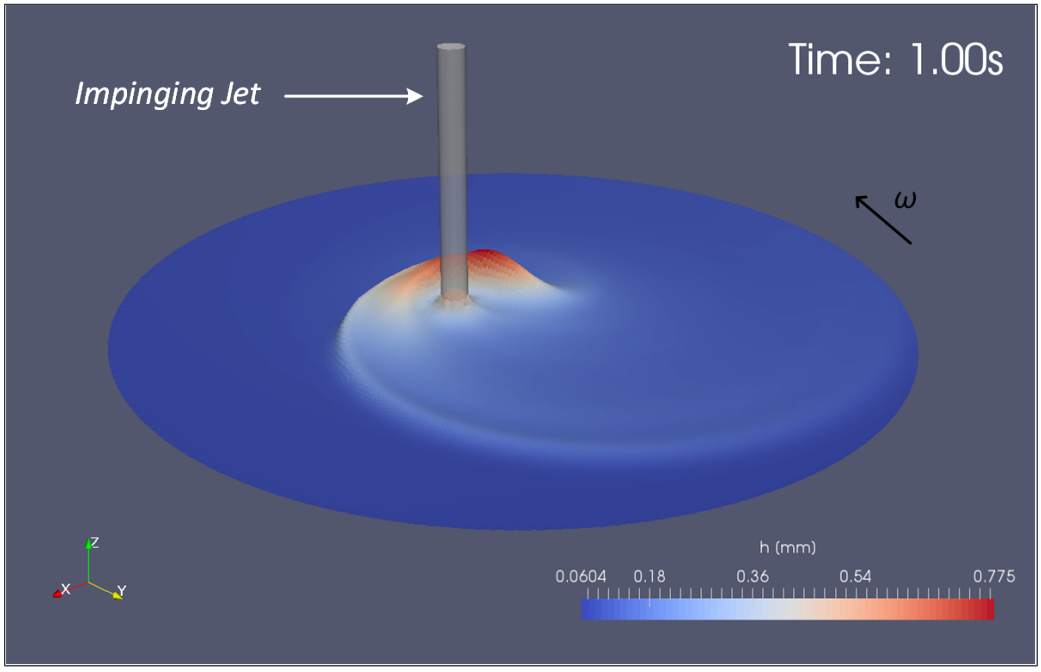

(a) Film relief (2D TFA): z-axis scaled 30×

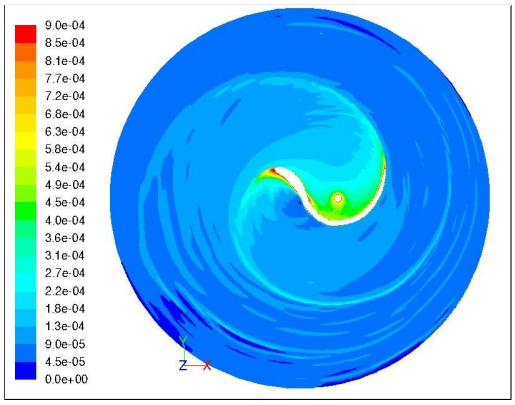

(b) Film height (3D VoF)

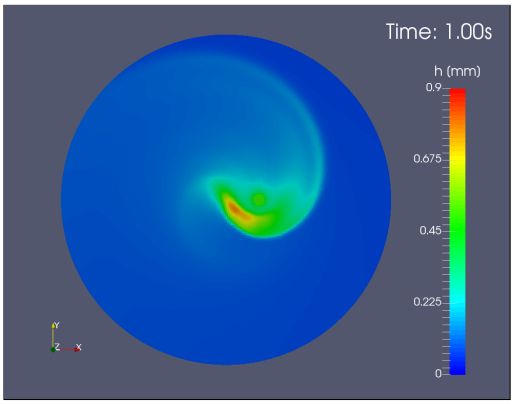

(c) Film height (2D TFA)

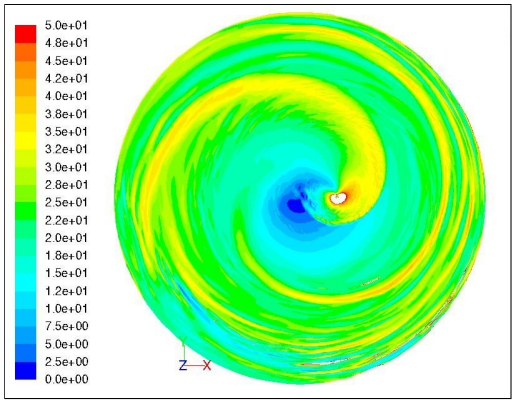

(d) Shear stress (3D VoF)

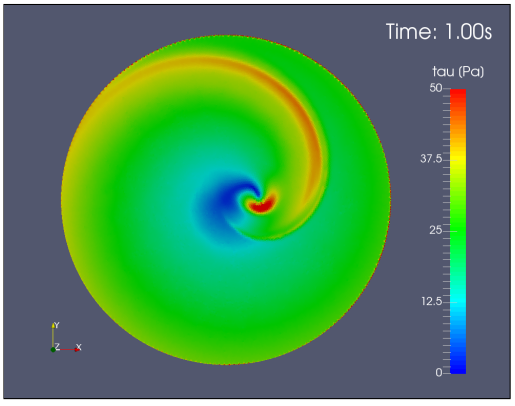

(e) Shear stress (2D TFA)

Figure 5.21: Case 3b: $\Delta r = 30\text{mm}$, $\nu = 2.87 \times 10^{-6}\text{m}^2\,\text{s}^{-1}$, $Q = 1.5\text{lpm}$, $\omega = 500\text{rpm}$; 3D VoF solution courtesy of TU Graz

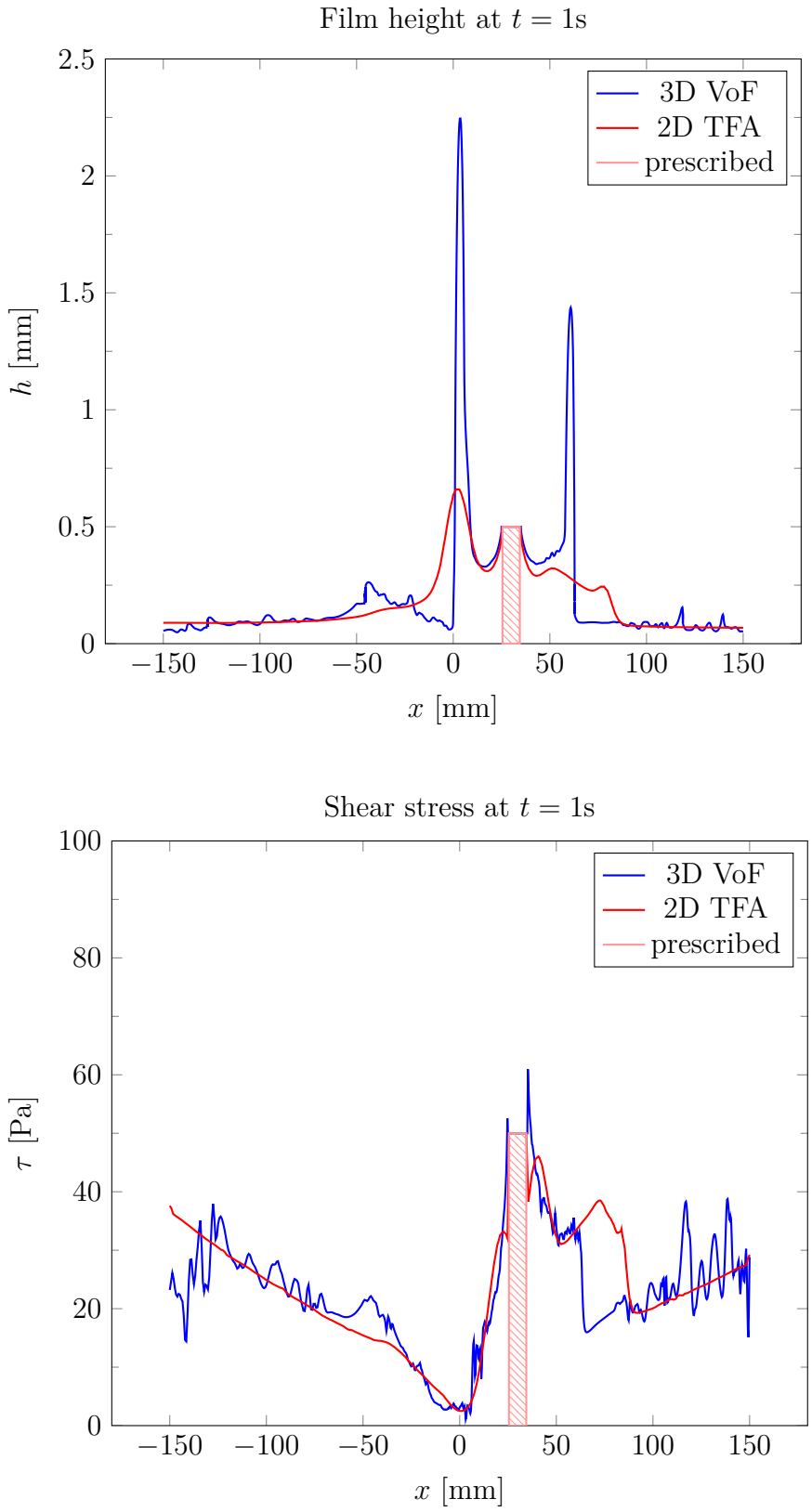

Figure 5.22: Case 3b: xz-plane through the impinging jet; 3D VoF solution courtesy of TU Graz

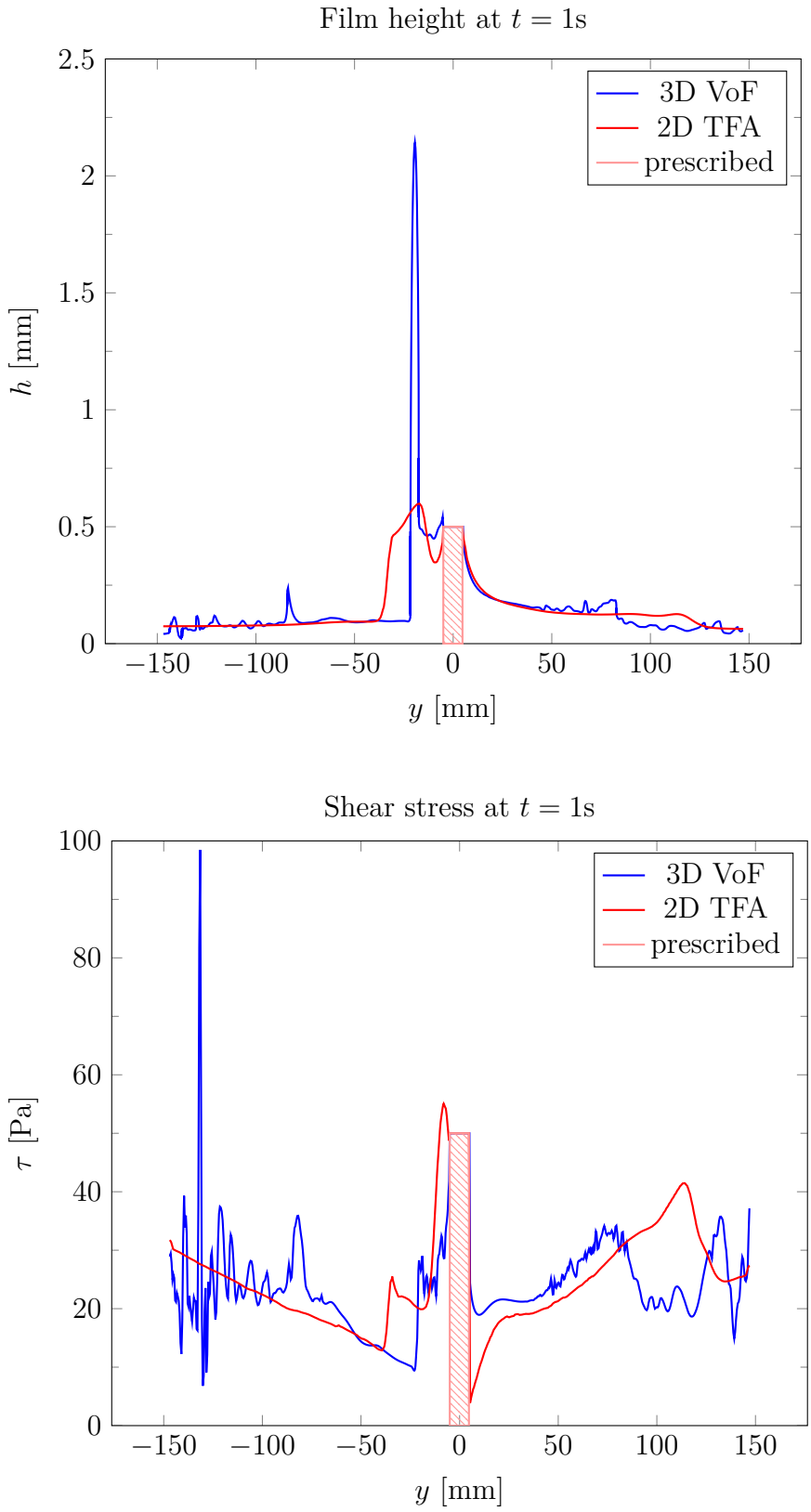

Figure 5.23: Case 3b: yz-plane through the impinging jet; 3D VoF solution courtesy of TU Graz

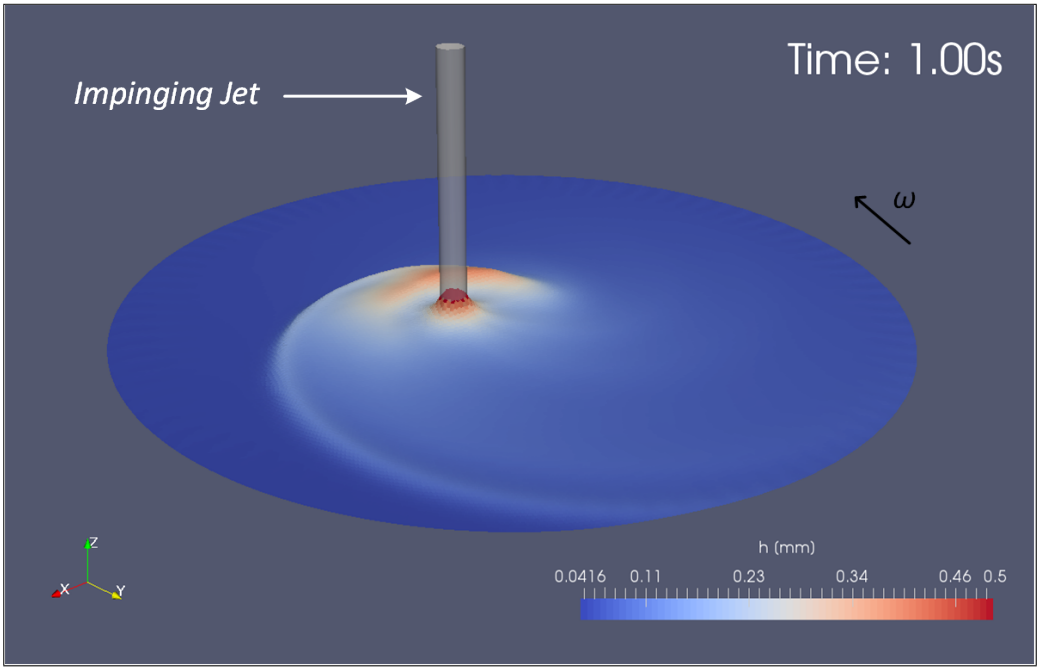

(a) Film relief (2D TFA): z-axis scaled 30×

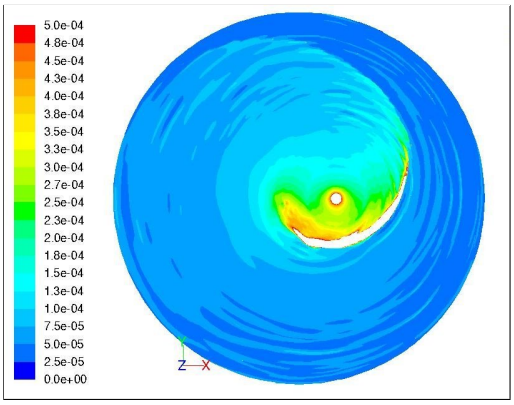

(b) Film height (3D VoF)

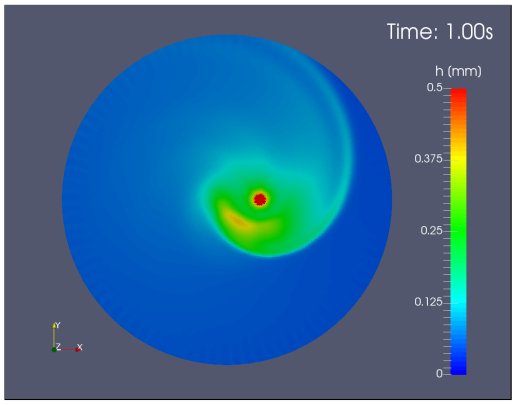

(c) Film height (2D TFA)

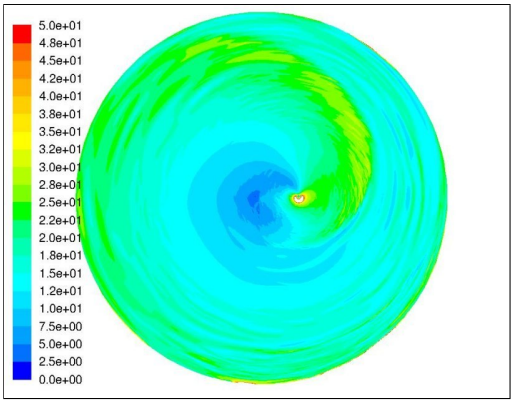

(d) Shear stress (3D VoF)

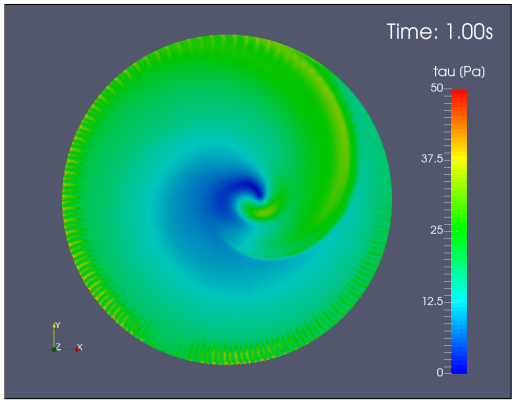

(e) Shear stress (2D TFA)

Figure 5.24: Case 3c: $\Delta r = 30\text{mm}$, $\nu = 1 \times 10^{-6}\text{m}^2\,\text{s}^{-1}$, $Q = 1.5\text{lpm}$, $\omega = 500\text{rpm}$; 3D VoF solution courtesy of TU Graz

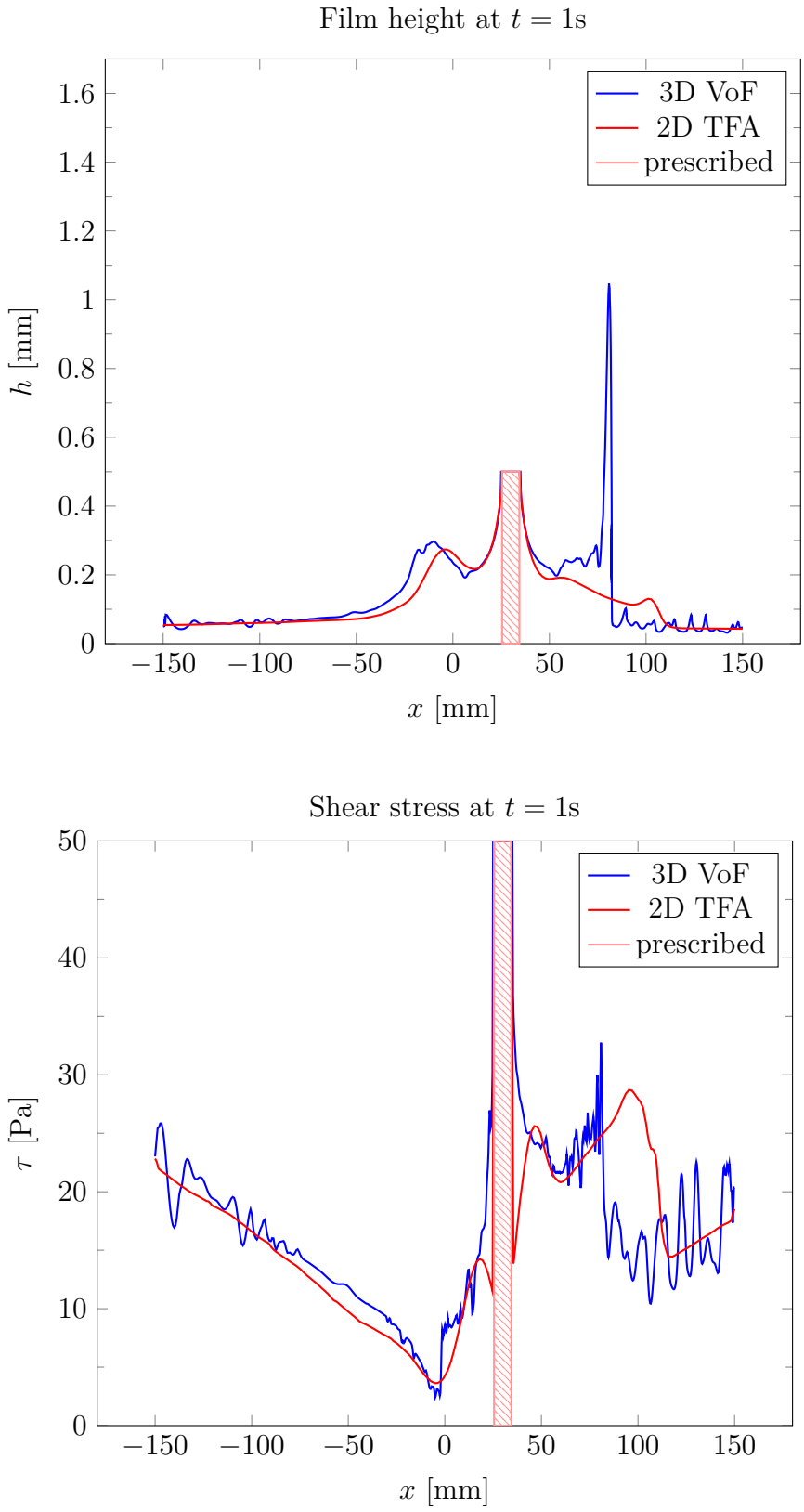

Figure 5.25: Case 3c: xz-plane through the impinging jet; 3D VoF solution courtesy of TU Graz

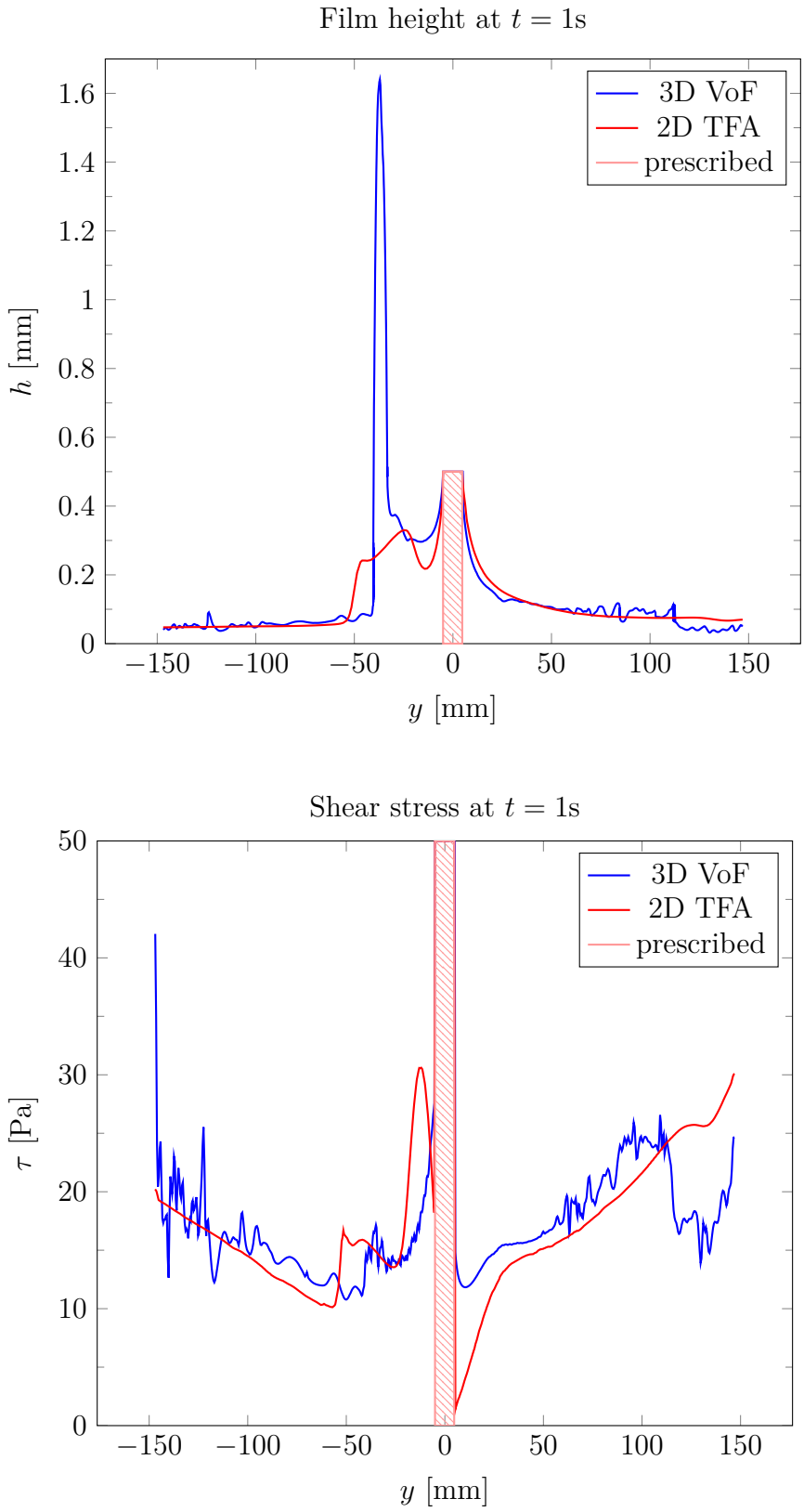

Figure 5.26: Case 3c: yz-plane through the impinging jet; 3D VoF solution courtesy of TU Graz

represent a *jump discontinuity* in the underlaying equations. Therefore a dry spot in the 2D TFA simulation is never really "dry" but it contains an extremely thin fluid film that has to be interpreted as a dry spot. The 3D VoF method develops a sharper phase interface compared to the 2D TFA method.

The film flow solutions of the case 3d, see the figure 5.27, show notable differences in the hydraulic jump front formation. The 3D VoF film height contour plot suggests a very thin hydraulic jump wave, in contrary to the 2D TFA solution that predicts considerably thicker wave. The comparison of the shear stress contour plots shows some differences especially along the the wave borders. In general, a relatively good agreement is achieved.

The observations are confirmed by the xz- and yz-plane cuts through the impinging jet. The very thin and high hydraulic jump prediction of the 3D VoF simulation is in the strong contrast to the 2D TFA method as seen on the yz-plane cut, see the figure 5.29. The different film height in the hydraulic jump projects as well into the different shear stress at the same location. The areas outside of the hydraulic jump are showing a good agreement.

The lower fluid viscosity of the case 3e, see the figure 5.30, leads similarly to the previous cases to the wider and not so high hydraulic jump solution. The hydraulic jump is not only considerably thicker in the 2D TFA solution opposite to the 3D VoF method, but it is as well wider. Farther, a wavelet pattern, visible in the film height relief, develops near to the disc edge. The wavelet pattern shines in the shear-stress 2D TFA contour plot as the very thin film of high velocity is connected to a very high shear stress. The size of the dry spot is due to the lower viscosity smaller and clearly less pronounced in the case of 2D TFA simulation.

The xz- and yz-plane cuts through the impinging jet confirm the observations. The thicker hydraulic jump of lower height predicted by the 2D TFA simulation is in the contrast to the thin and high prediction of hydraulic jump in the 3D VoF method, well visible on the left side of the plot in the figure 5.32. The wider hydraulic jump prediction than introduces a bigger discrepancy into the yz-plane cut visible from the radius of 90mm.

5.5.3 Dynamic Inlet

A specifically requested feature of the TFA solver is a dynamic inlet that can move freely over the rotating disc surface. The inlet implementation is optimised for the dynamically moving jet. As a result it is very simple to change the position of the inlet within every time step. In fact, it is just a question of selecting new control areas and fixing the solution values in them. Considering the high-performance of the TFA solver, the dynamic inlet implementation opens a new possibilities in the thin film simulation on the rotating disc.

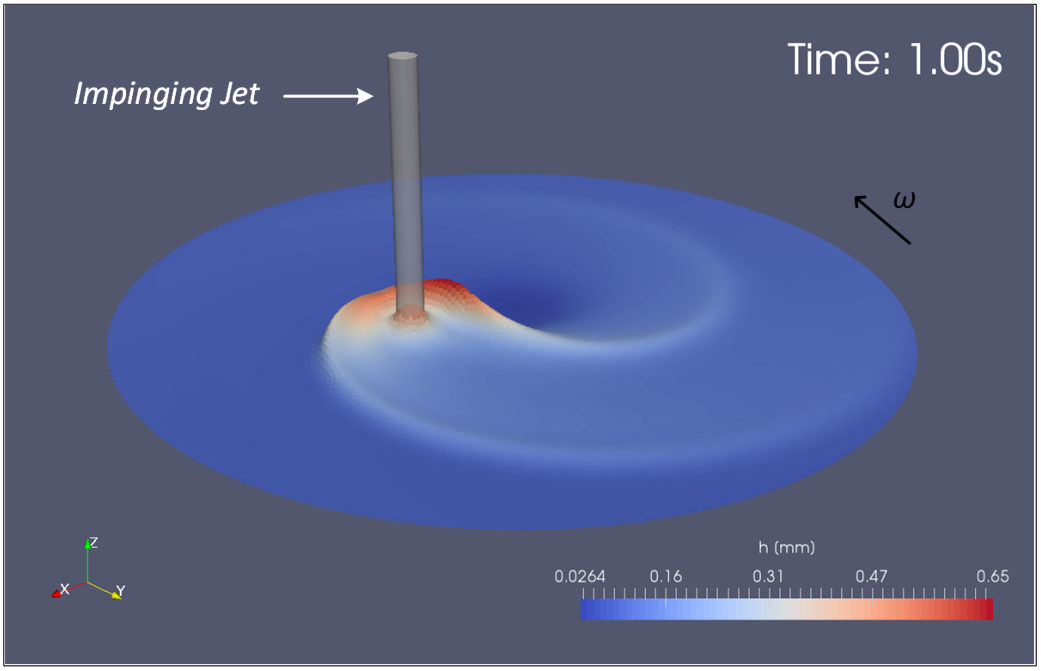

(a) Film relief (2D TFA): z-axis scaled 30×

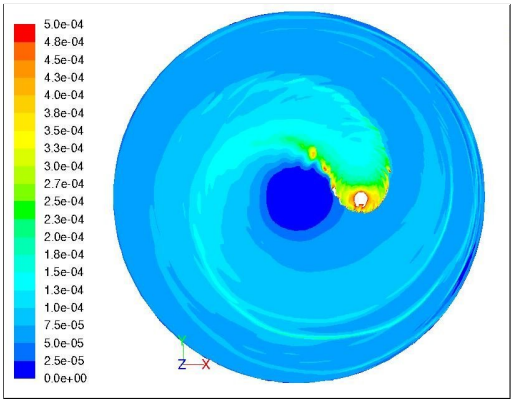

(b) Film height (3D VoF)

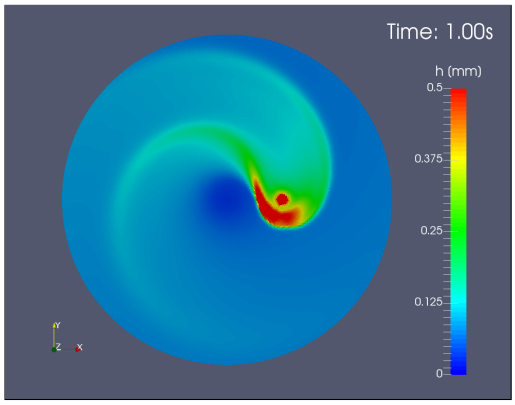

(c) Film height (2D TFA)

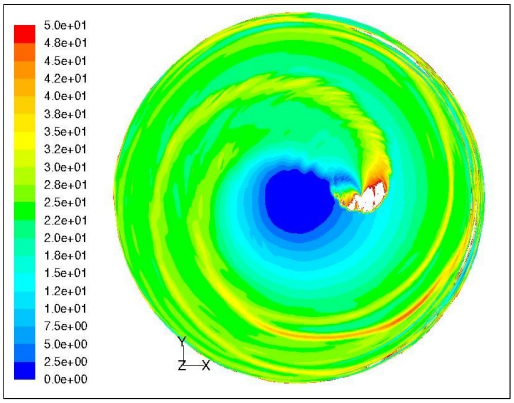

(d) Shear stress (3D VoF)

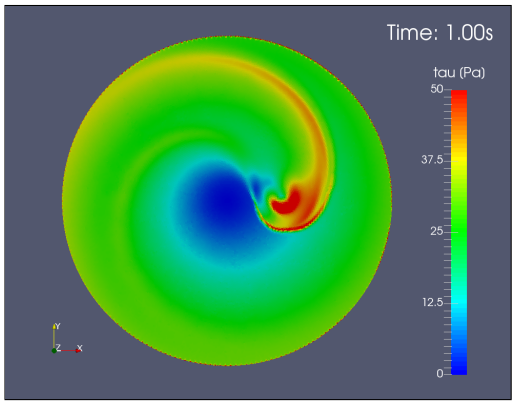

(e) Shear stress (2D TFA)

Figure 5.27: Case 3d: $\Delta r = 50\text{mm}$, $\nu = 2.87 \times 10^{-6}\text{m}^2\,\text{s}^{-1}$, $Q = 1.5\text{lpm}$, $\omega = 500\text{rpm}$; 3D VoF solution courtesy of TU Graz

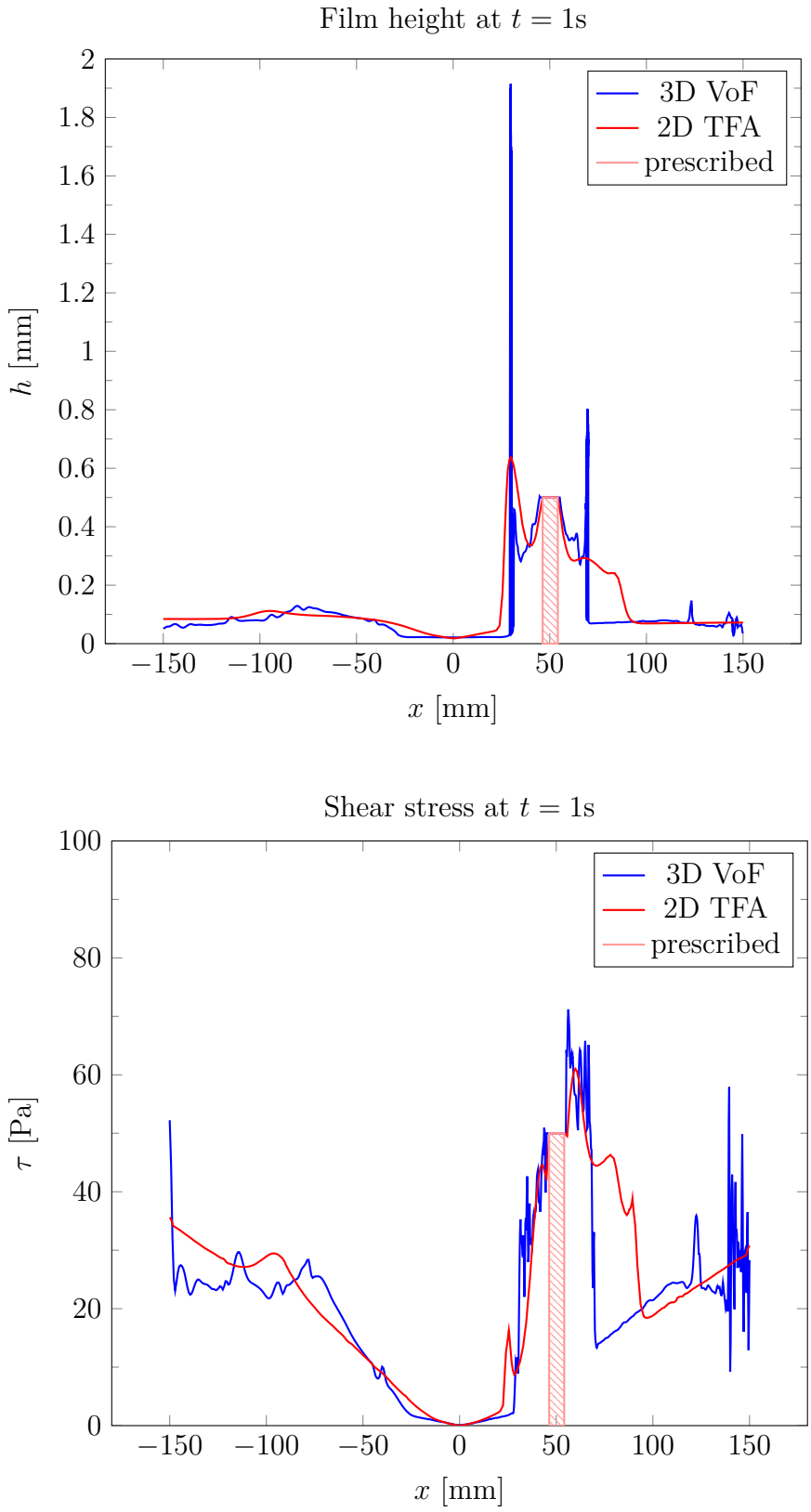

Figure 5.28: Case 3d: xz-plane through the impinging jet; 3D VoF solution courtesy of TU Graz

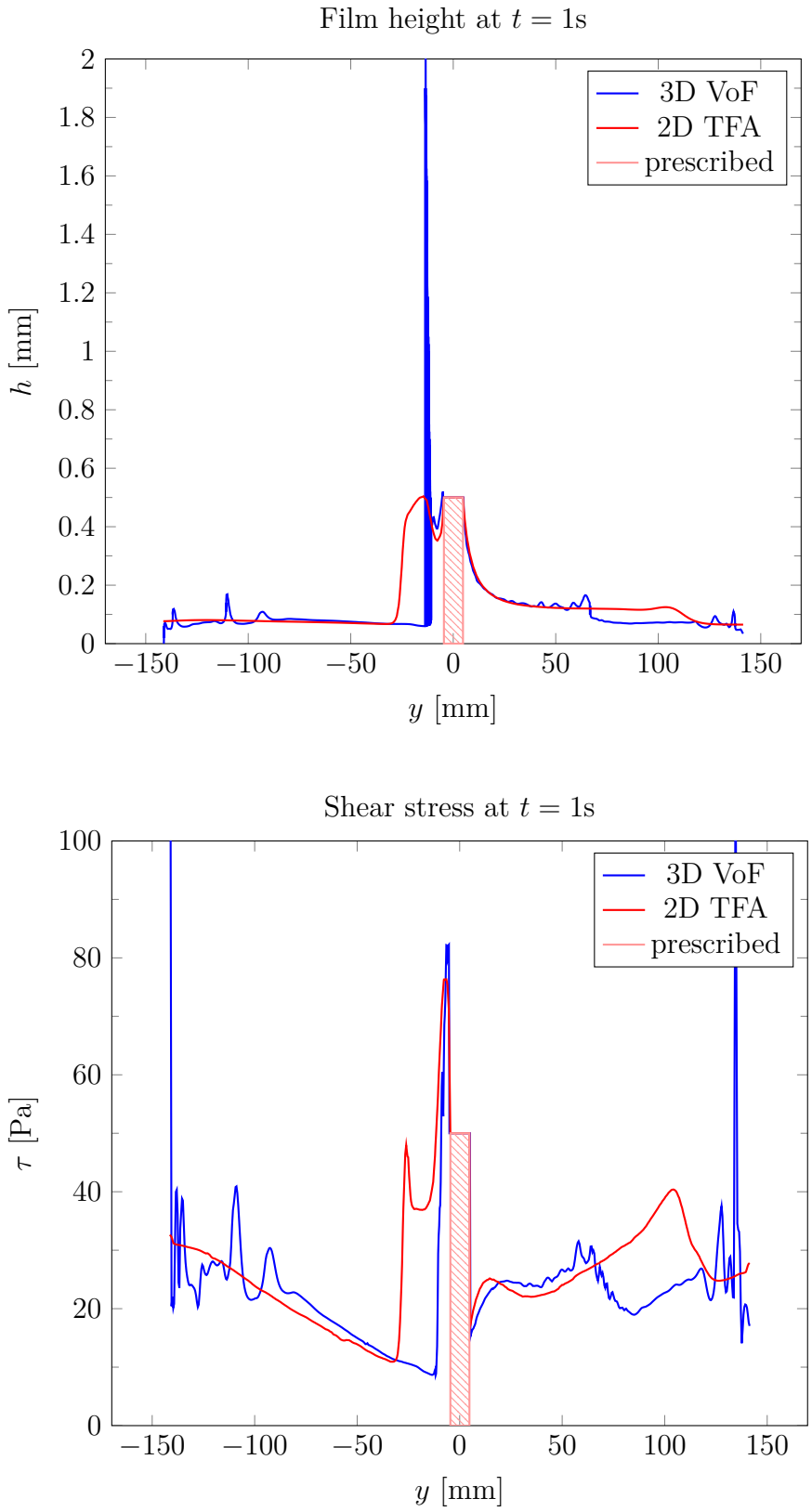

Figure 5.29: Case 3d: yz-plane through the impinging jet; 3D VoF solution courtesy of TU Graz

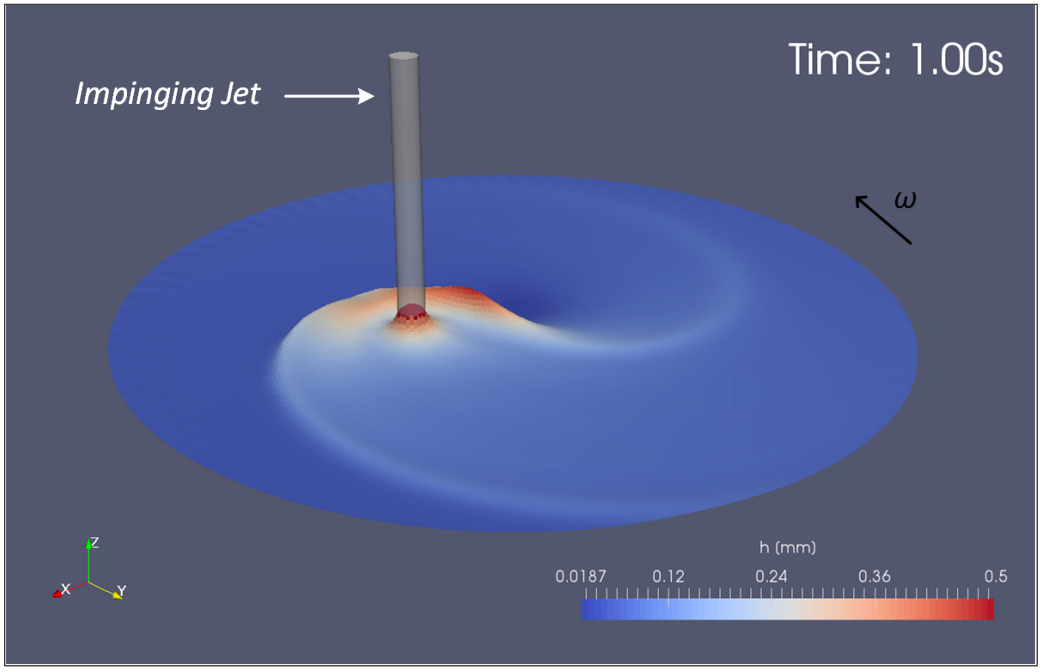

(a) Film relief (2D TFA): z-axis scaled 30×

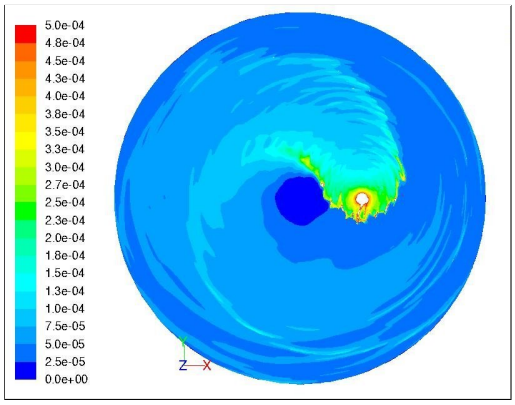

(b) Film height (3D VoF)

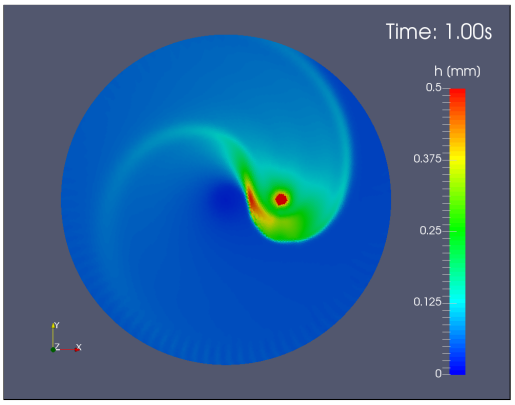

(c) Film height (2D TFA)

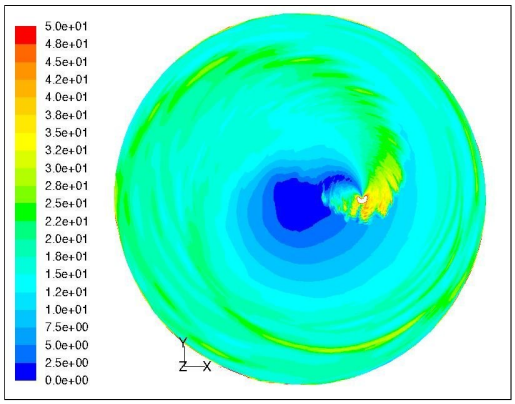

(d) Shear stress (3D VoF)

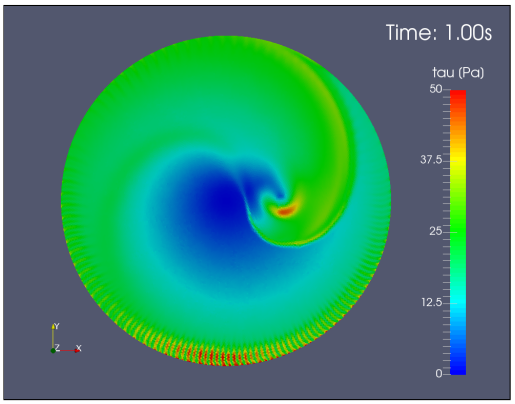

(e) Shear stress (2D TFA)

Figure 5.30: Case 3e: $\Delta r = 50\text{mm}$, $Q = 1.5\text{lpm}$, $\nu = 1 \times 10^{-6}\text{m}^2\,\text{s}^{-1}$, $\omega = 500\text{rpm}$; 3D VoF solution courtesy of TU Graz

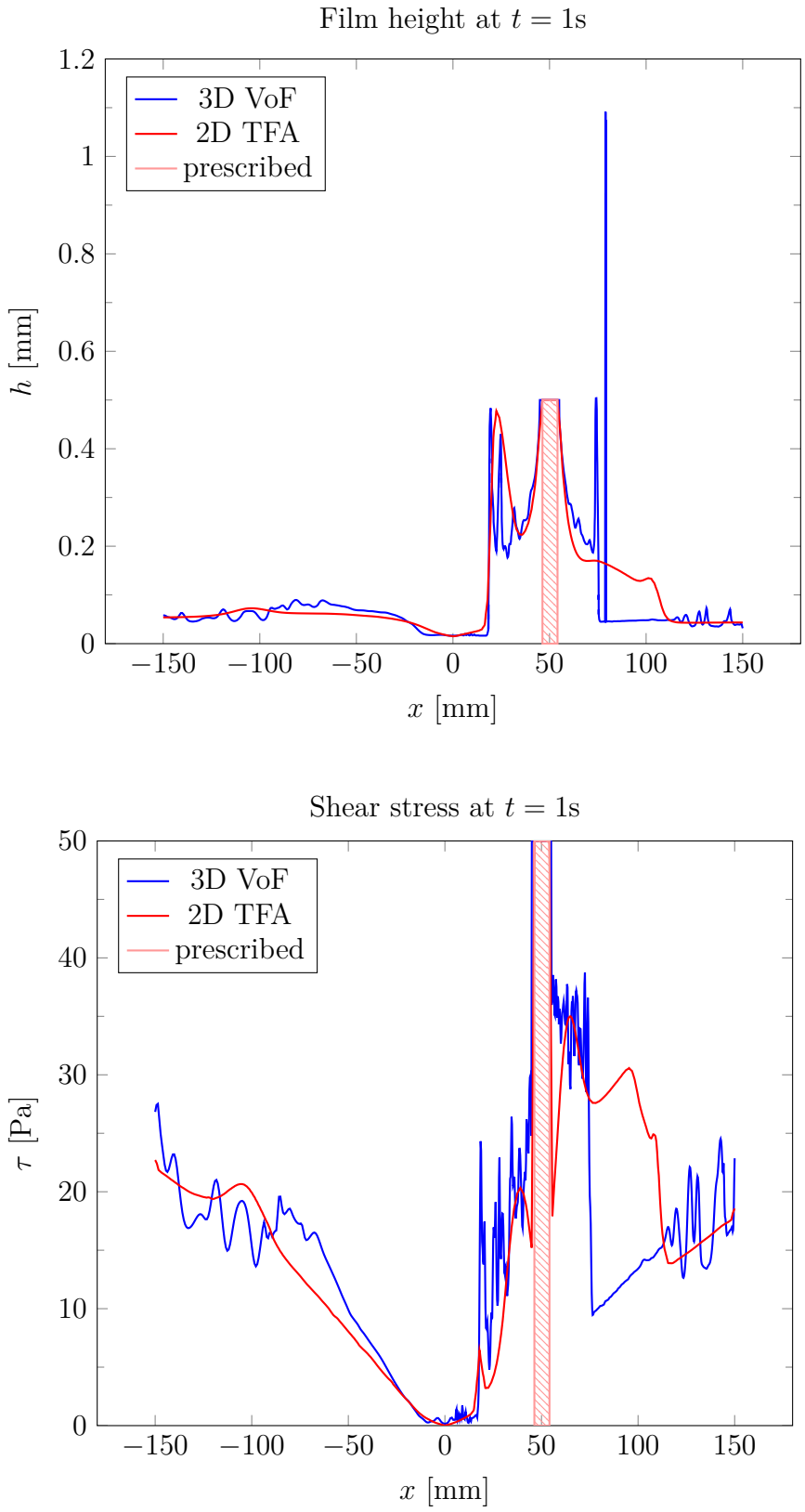

Figure 5.31: Case 3e: xz-plane through the impinging jet; 3D VoF solution courtesy of TU Graz

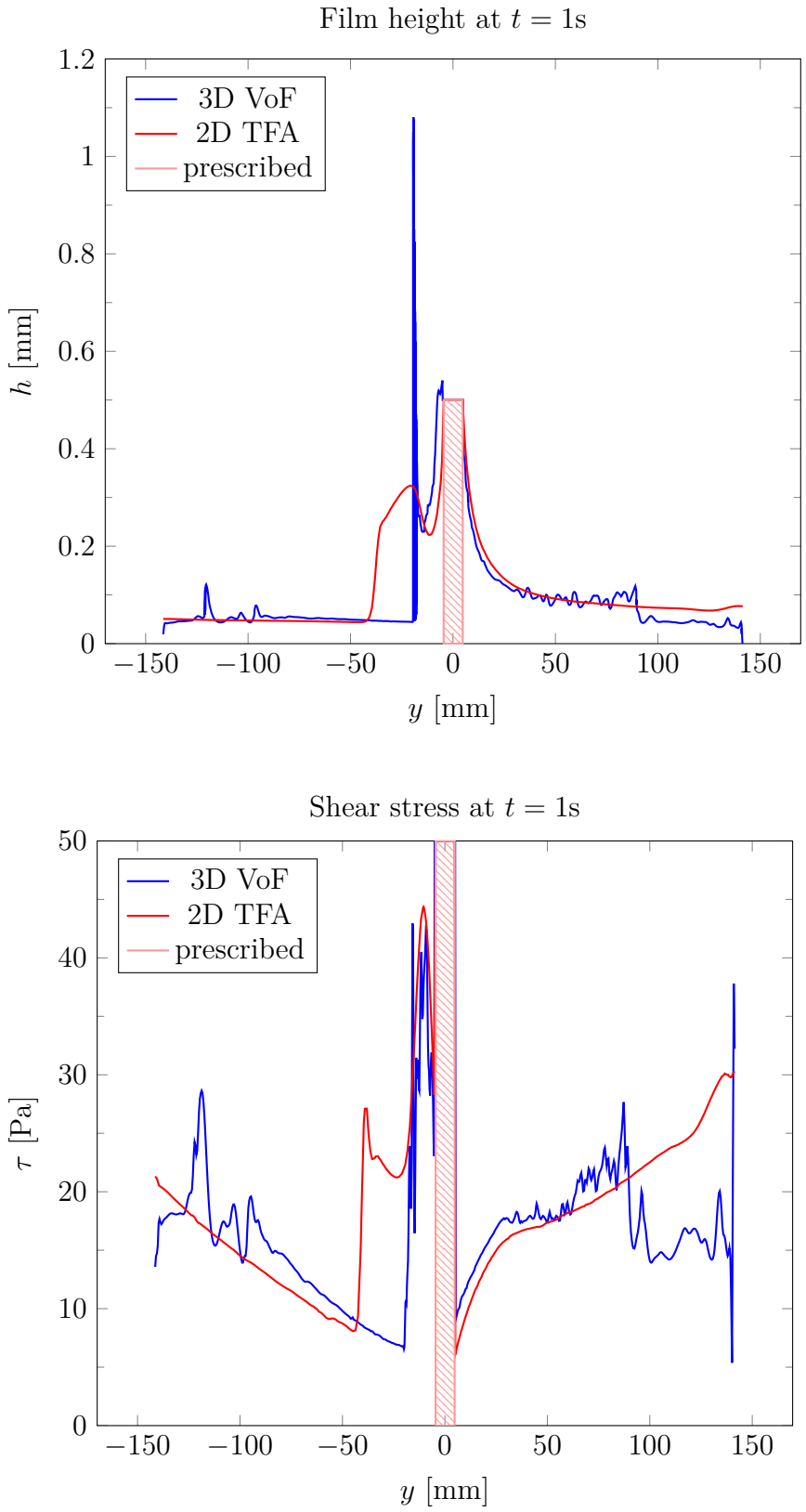

Figure 5.32: Case 3e: yz-plane through the impinging jet; 3D VoF solution courtesy of TU Graz

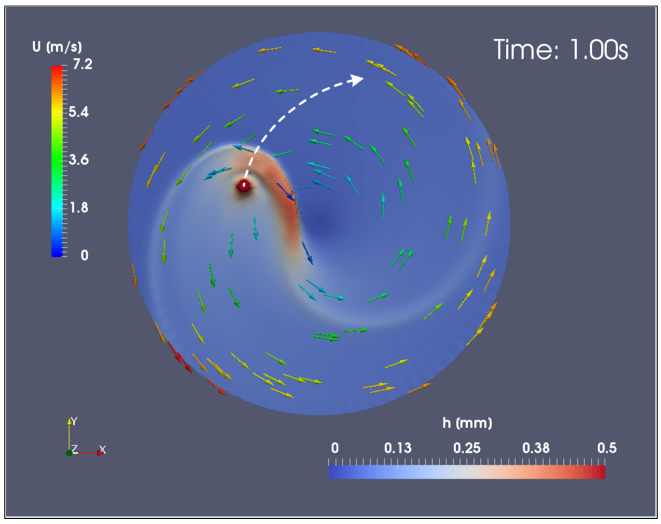

(a) Dynamic inlet at $t = 1$s

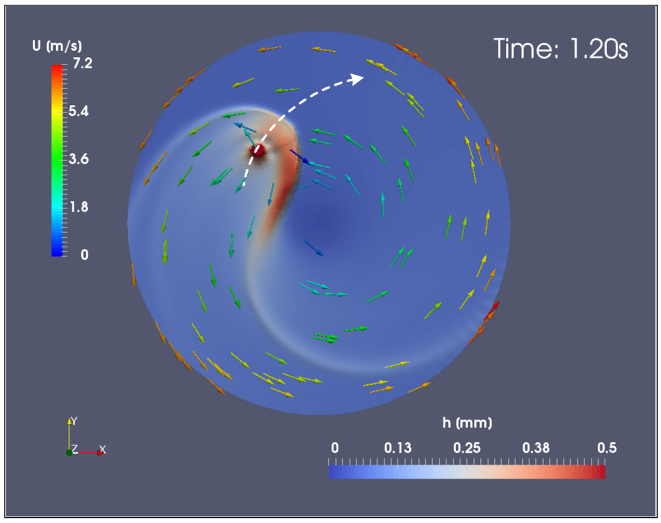

(b) Dynamic inlet at $t = 1.2$s

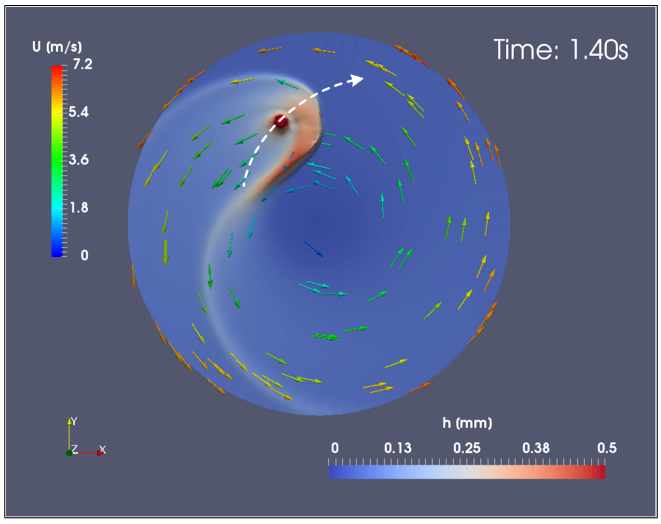

(c) Dynamic inlet at $t = 1.4$s

Figure 5.33: Dynamic inlet (1s–1.4s): $\nu = 1 \times 10^{-6}\mathrm{m}^2\,\mathrm{s}^{-1}$, $Q = 1.5$lpm, $\omega = 400$rpm; dynamic inlet trajectory is marked with the white dashed line

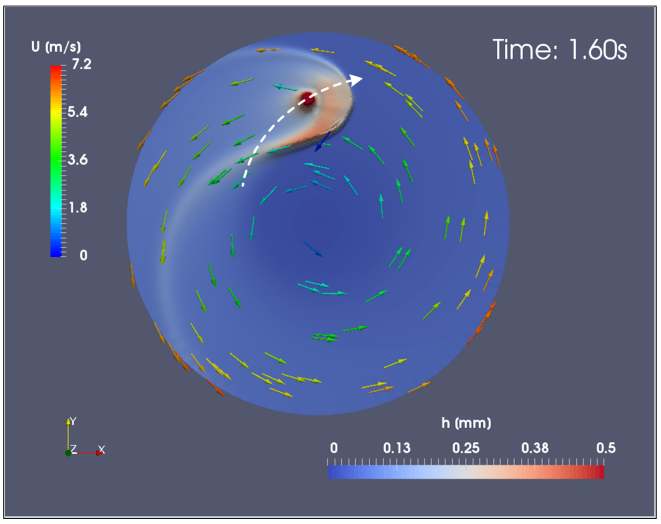

(a) Dynamic inlet at $t = 1.6$s

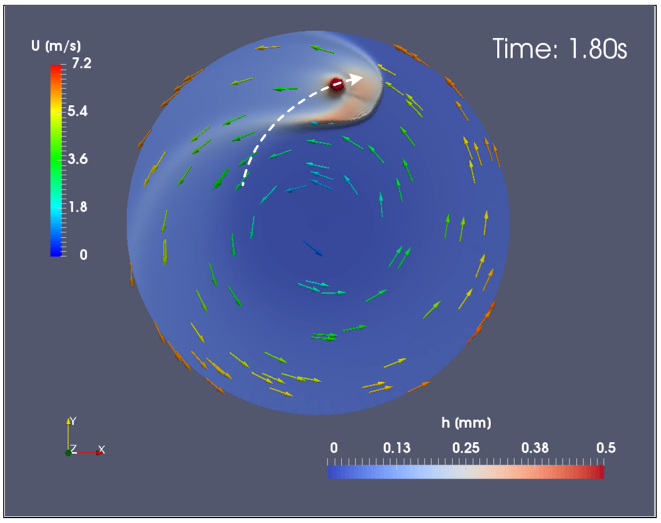

(b) Dynamic inlet at $t = 1.8$s

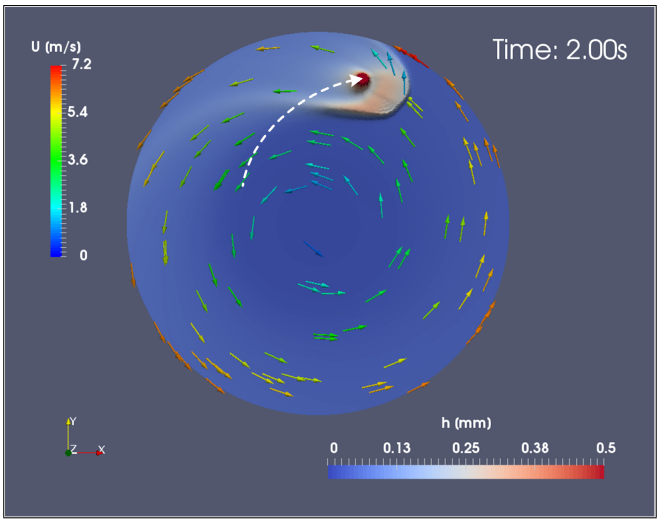

(c) Dynamic inlet at $t = 2$s

Figure 5.34: Dynamic inlet (1.6s–2s): $\nu = 1 \times 10^{-6}\mathrm{m}^2\,\mathrm{s}^{-1}$, $Q = 1.5$lpm, $\omega = 400$rpm; dynamic inlet trajectory is marked with the white dashed line

The validation of the dynamically moving inlet is not possible at the moment due to the lack of the data to compare with. However it can be assumed that the accuracy of the dynamic inlet solution should not deviate much from the accuracy of the static inlet solution.

A single case with an excentric impingement is presented for an illustration of the dynamic inlet in the figure 5.33. The picture shows series of instantaneous film height contour plots enhanced with the fluid velocity glyphs from the start time $t_{\text{start}} = 1\text{s}$ to the end time $t_{\text{end}} = 2\text{s}$. The trajectory of the dynamically moving inlet is marked with a dashed line. The changing shape of the hydraulic jump and the development of the dry spot in the disc centre need no additional comments.

The dynamic inlet can have defined any trajectory imposed by an industrial process. There exist no limitations or additional assumptions regarding the inlet trajectory. The trajectory itself is decided on the case-by-case basis. The complex trajectories can be analysed in order to detect, for example, dry spot formations.

5.6 Summary and Discussion

An application of the TFM model on real problems, so called TFA approximation, has been discussed. The limitations of the TFM model–the hydraulic jump and the impingement area–were pointed out. The resulting approximation, the TFA solution, can be still used for a study of the thin film on the rotation disc, provided the method weaknesses are kept in mind.

The numerical FA method, a specialisation of the FV method for the film flows on three-dimensional surfaces, used for the implementation of the TFA solver was introduced. A short primer on specifics of the FA method, FA discretisation and solving of the resulting linear equations was given.

The following discussion of the TFA solver implementation pointed out specific implementation details as the handling on the non-linear convective term, the calculation of the edge flux, the PISO-based pressure-velocity coupling and the outlet and the inlet. Especially the inlet implementation that enables the dynamic inlet was worked out in details.

An overview of used meshes and their selection was given. The picked computational mesh, the polyhedral mesh, showed generally least solution artifacts as its honeycomb cells are neutral toward the flow direction.

The TFA solver was validated in comparisons of 2D TFA and 3D VoF solutions at the end of the chapter. The 2D TFA solutions are showing a good agreement with the 3D VoF results. The only problematic areas are the hydraulic jump and the impingement zone, both connected to invalidated assumptions of the TFM model.

One of the 2D TFA characteristics is a very smooth solution with the lack of the

	3D VoF ANSYS Fluent 12.1.2	2D TFA `foam-1.6-extend`
mesh	5×10^6 cells	36886 cells
Intel Core i7 CPU Bloomfield-family	4 cores	1 core
1s of simulated process	30days	2h

Table 5.3: 2D TFA and 3D VoF performance

surface waviness. This is the price payed for the neglected flow in the vertical dimension.

On the second side the 2D TFA simulation convinces with its extremely short simulation times, see the table 5.3.

While relatively little can be done with the solution of the impingement area, the hydraulic jump modelling can be improved with better velocity profiles of higher polynomial order. An introduction of the following additional boundary condition

$$\overline{\mathbf{u}}|_{z=\delta} = 0 \tag{5.38}$$

where δ is the the flow separation line, would than account for the separation region and increase the velocity profile accuracy.

The approximation accuracy, the dynamic inlet and the little computational resources needed suggest, that the 2D TFA method is a feasible alternative approach to the investigation of the thin film on a rotating disc.

Chapter 6

Chemistry Model

An important step in the semiconductor production process is the thinning of the silicon wafers. The main part of the thinning is usually done by mechanical grinding that leaves a rough surface. In order to achieve a higher surface quality and removal of mechanically damaged surface layer an additional step, so called *wet chemical etching*, follows. An important requirement on the wet chemical etching step is a uniformity of the etching process which is strongly influenced by hydrodynamics. The numerical and experimental investigations by Kaneko et al.[53] suggested that the wet etching process can be modelled with a great accuracy by a diffusion-controlled chemical model. In this chapter, a simple chemistry model for the TFM based on the work of Kaneko et al. together with results of TFA simulations is presented.

6.1 Simple Chemistry Model

The wet etching is based on the application of an etching solution consisting essentially of nitric acid HNO_3 and a high concentration of hydrofluoric acid HF. The two main reaction steps in the etching reaction are given by the following

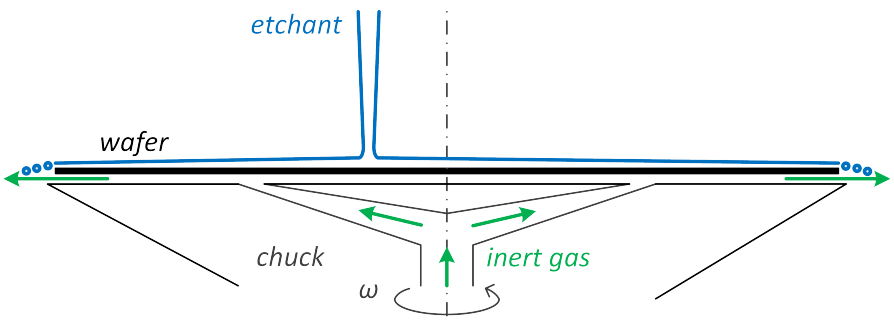

Figure 6.1: Wet chemical single side etching

reaction equations

$$\begin{aligned} \mathrm{Si} + 4\mathrm{HNO_3} &\rightarrow \mathrm{SiO_2} + 4\mathrm{NO_2} + 2\mathrm{H_2O} \\ \mathrm{SiO_2} + 6\mathrm{HF} &\rightarrow \mathrm{H_2SiF_6} + 2\mathrm{H_2O} \end{aligned} \tag{6.1}$$

with the first reaction being an oxidation followed by the second reaction, a dissolution, as described by Schwartz and Robbins[93].

The etching rate of the presented reaction scheme is limited by the concentration of HNO_3 as the etching solution has a high concentration of HF and only a low concentration of HNO_3.

The work of Kaneko et al. suggested a simplification to the reaction model. The reaction rate is proportional to the diffusion of HNO_3 toward the surface of the silicon wafer. Further was assumed an infinitely fast reaction as the time scale of the reaction is small compared to the time scale of the HNO_3 diffusion.

The connection of the etching rate to the mass fraction of the nitric acid HNO_3 only allows to model the etching solution as a binary mixture of a solvent, the carrier fluid, and an etching agent, the nitric acid itself. As the thin film model imposes incompressibility and constant density ρ on the carrier fluid, the transport of the nitric acid HNO_3 can be described with a single species transport equation

$$\frac{\partial c}{\partial t} + \nabla\bullet\left(\mathbf{u}c\right) = \nabla\bullet\left(D\nabla c\right) + S_c \tag{6.2}$$

where D is a diffusion coefficient of the species.

The etching rate can be determined from the mass flux of nitric acid into the wafer surface described by

$$j_{\mathrm{HNO_3}} = -\rho D \frac{\partial c}{\partial z}\bigg|_{z=0} \tag{6.3}$$

It can be assumed that the mass flux of nitric acid HNO_3 to the wafer surface reacts in a stoichiometric proportion with the silicon Si according to the first, the oxidation reaction 6.1. The etching rate R is than given by

$$R = \beta\left(\frac{M_{\mathrm{Si}}}{4M_{\mathrm{HNO_3}}}\right)\frac{j_{\mathrm{HNO_3}}}{\rho_{\mathrm{Si}}} \tag{6.4}$$

where β is an empiric correction factor, M_{Si} and $M_{\mathrm{HNO_3}}$ are molar masses of silicon and nitric acid.

6.2 Thin Film Transformation

The transformation of the species transport equation uses the same methodology as introduced in Chapter 4.

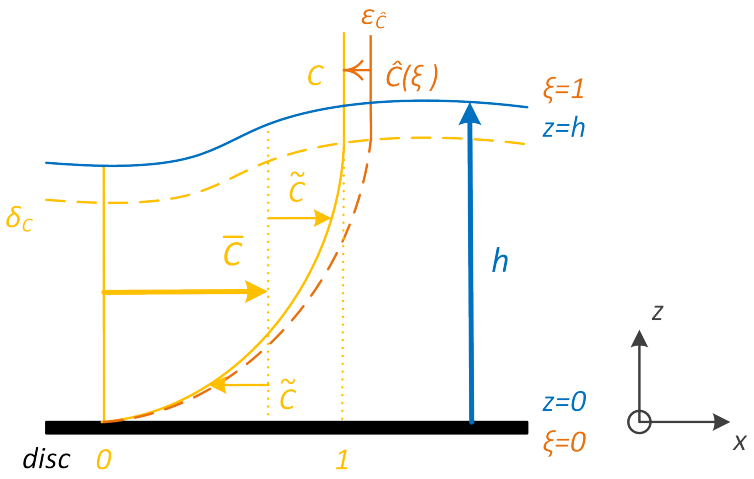

Figure 6.2: Concentration

6.2.1 Concentration

Before the transformation of the species transport equation, a concentration C based on the mass fraction of nitric acid HNO_3 against the inlet mass fraction has to be introduced

$$C = \frac{c}{c_{\text{inlet}}} \tag{6.5}$$

The concentration helps to avoid possible numerical problems in the solution of the transport equation and simplifies the definition of the boundary conditions.

The mean concentration $\overline{C}$, a new dependent variable in the thin film model, is then defined as

$$\overline{C} = \frac{1}{h}\int_h C\,dz \tag{6.6}$$

The mean concentration loses the concentration distribution across the film height. Therefore a concentration profile function $\hat{C}$ has to be defined in order to determine the concentration gradient at the wafer surface

$$\begin{aligned} C(t,x,y,z) &= \hat{C}(t,x,y,\xi) + \varepsilon_{\hat{C}} \\ \hat{C}(\xi) &= b_0 + b_1\xi + b_2\xi^2 \\ \xi \in \langle 0,1\rangle, z &= h\xi \end{aligned} \tag{6.7}$$

where $\varepsilon_{\hat{C}}$ denotes the concentration profile modelling error and ξ is the normalised vertical coordinate.

The polynomial coefficients b_i are determined by the set of the boundary conditions

- All the reactant is consumed in the etching reaction at the disc

$$\hat{C}(\xi)|_{\xi=0} = 0 \tag{6.8}$$

- Von Neumann boundary condition at the free-surface

$$\left.\frac{\partial \hat{C}(\xi)}{\partial \xi}\right|_{\xi=1} = 0 \tag{6.9}$$

- Relation to the mean reactant concentration

$$\int_0^1 \hat{C}(\xi)\, d\xi = \overline{C} \tag{6.10}$$

which provide the following solution of the concentration profile function, Appendix A.2

$$\hat{C}(\xi) = 3\overline{C}\left(\xi - \frac{1}{2}\xi^2\right) \tag{6.11}$$

The boundary conditions above assume a parabolic concentration profile across the full film height. That means that the concentration boundary layer δ_C is expected to be identical with the film free-surface. Should the concentration boundary δ_C be considered, a corresponding boundary condition has to be introduced

$$\left.\frac{\partial C}{\partial z}\right|_{z=\delta_C} = 0 \tag{6.12}$$

As the concentration distribution across the film height is not uniform the spatial concentration fluctuations have to be used to accurately determine species transport in the nonlinear advection term

$$C = \overline{C} + \tilde{C} \tag{6.13}$$

Provided that the concentration profile function $\hat{C}$ accurately models the concentration distribution across the film height, the concentration fluctuation $\tilde{C}$ can be approximated by

$$\tilde{C} = C - \overline{C} = \lim_{\varepsilon_{\hat{C}} \to 0} \left\{\hat{C}(\xi) - \overline{C}\right\} \tag{6.14}$$

6.2.2 Transformation of Species Transport Equation

The species transport equation starts with reformulation of the equation 6.2 for the concentration C

$$\frac{\partial C}{\partial t} + \nabla\bullet\,(\mathbf{u}C) = \nabla\bullet\,(D\nabla C) + S_C \tag{6.15}$$

First of all the LHS of the equation is being integrated across the film height in

the analogy to the momentum equation transformation 4.3.3

$$\begin{aligned}
&\int_0^h \left[\frac{\partial C}{\partial t} + \nabla\bullet\left(\mathbf{u}C\right)\right] dz \\
&\quad= \int_0^h \frac{\partial C}{\partial t}\, dz + \int_0^h \nabla\bullet\left[(\overline{\mathbf{u}}+\tilde{\mathbf{u}})(\overline{C}+\tilde{C})\right] dz \\
&\quad= \frac{\partial}{\partial t}\int_0^h C\, dz + \nabla\bullet\left[\int_0^h (\overline{\mathbf{u}C} + \overline{\mathbf{u}}\tilde{C} + \tilde{\mathbf{u}}\overline{C} + \tilde{\mathbf{u}}\tilde{C})\, dz\right] \\
&\quad= \frac{\partial}{\partial t}(h\overline{C}) + \nabla\bullet\left(h\overline{\mathbf{u}C}\right) + \nabla\bullet\left(\int_0^h \tilde{\mathbf{u}}\tilde{C}\, dz\right)
\end{aligned} \tag{6.16}$$

The boundary terms after application of the Leibniz integral rule, Appendix B.2.2, diminish in the same way as already presented in the Chapter 4. The product terms of the spatial fluctuations with the mean quantities as well reduce to zero.

The newly introduced term, the product of the concentration spatial fluctuation and momentum spatial fluctuation, is then expressed by the help of the equations 6.14 and 4.21 and approximated by the solutions of the profile functions 6.11 and 4.16 as

$$\begin{aligned}
&\rho\nabla\bullet\left(\int_0^h \tilde{\mathbf{u}}\tilde{C}\, dz\right) \\
&\quad= \lim_{\substack{\varepsilon_{\hat{C}}\to 0 \\ \varepsilon_{\hat{\mathbf{u}}}\to 0}} \left\{\nabla\bullet\left[\int_0^1 (\hat{\mathbf{u}}(\xi)-\overline{\mathbf{u}})\left(\hat{C}(\xi)-\overline{C}\right) h\, d\xi\right]\right\} \\
&\quad= \nabla\bullet\left[\frac{11}{50} h\overline{C}(\overline{\mathbf{u}}-\mathbf{u}_{\text{disc}})\right]
\end{aligned} \tag{6.17}$$

The RHS of the species transport equation is transformed into

$$\begin{aligned}
&\int_0^h \nabla\bullet\left(D\nabla C\right) dz + S_C \\
&\quad= \nabla\bullet\left(hD\nabla\overline{C}\right) + \int_0^h \frac{\partial}{\partial z}\left(D\frac{\partial C}{\partial z}\right) dz + S_C \\
&\quad= \nabla\bullet\left(hD\nabla\overline{C}\right) - D\frac{\partial C}{\partial z}\bigg|_{z=0} + S_C
\end{aligned} \tag{6.18}$$

where the boundary terms emerging during the transformation either diminish due to boundary conditions or are assumed to be negligible.

The concentration gradient at the disc surface is resolved by the help of the con-

centration profile function $\hat{C}$ as

$$\begin{aligned} D\frac{\partial C}{\partial z}\bigg|_{z=0} & \\ &= \lim_{\varepsilon_{\hat{C}}\to 0}\left\{ D\frac{\partial \hat{C}(\xi)}{\partial h\xi}\bigg|_{\xi=0}\right\} \\ &= 3\frac{D}{h}\,\overline{C} \end{aligned} \tag{6.19}$$

The resulting species transport equation for the thin film has the form

$$\frac{\partial}{\partial t}(h\overline{C}) + \nabla\bullet\left(h\overline{\mathbf{u}C} + K\right) = \nabla\bullet\left(hD\nabla\overline{C}\right) - D\frac{\partial C}{\partial z}\bigg|_{z=0} + S_C \tag{6.20}$$

where the advective term K and the concentration gradient at the disc bottom are expressed with the help of solutions of the profile models $\hat{C}$ and $\hat{\mathbf{u}}$ as

$$\begin{aligned} K &= \frac{11}{50}h\overline{C}(\overline{\mathbf{u}} - \mathbf{u}_{\text{disc}}) \\ \frac{\partial C}{\partial z}\bigg|_{z=0} &= 3\frac{1}{h}\,\overline{C} \end{aligned}$$

and concentration source S_C has to be determined on the case-to-case basis.

6.2.3 Transformation of the Simple Chemistry Model

The simple diffusion-controlled chemistry model, the equations 6.3 and 6.4, uses the concentration profile $\hat{C}$ and its solution 6.11 to express the etching rate R as

$$\begin{aligned} R &= \beta\left(\frac{M_{\text{Si}}}{4M_{\text{HNO}_3}}\right)\frac{j_{\text{HNO}_3}}{\rho_{\text{Si}}} \\ &= \beta\left(\frac{M_{\text{Si}}}{4M_{\text{HNO}_3}}\right)\frac{\rho}{\rho_{\text{Si}}}D\frac{\partial c}{\partial z}\bigg|_{z=0} \\ &= \lim_{\varepsilon_{\hat{C}}\to 0}\left\{\beta\left(\frac{M_{\text{Si}}}{4M_{\text{HNO}_3}}\right)\frac{\rho}{\rho_{\text{Si}}}D\left(c_{\text{inlet}}\frac{\partial \hat{C}(\xi)}{\partial(h\xi)}\bigg|_{\xi=0}\right)\right\} \\ &= \beta\left(\frac{M_{\text{Si}}}{4M_{\text{HNO}_3}}\right)\frac{\rho}{\rho_{\text{Si}}}D\left(3\frac{c_{\text{inlet}}}{h}\overline{C}\right) \end{aligned} \tag{6.21}$$

where β is the empiric reaction rate correction factor that has to be fitted to experimental reaction rates.

Case	Δr [mm]	ν [$m^2\,s^{-1}$]	Q [lpm]	ω [rpm]
4a	55	1×10^{-6}	2.8	400
4b	95			
4c	30	2.87×10^{-6}	1.5	500

Table 6.1: Case definitions for chemistry model

6.3 Simulations

The presented simple chemistry model was implemented as an extension to the TFA solver code discussed in the Chapter 5. The species transport equation is being solved every time iteration after the solution of momentum and continuity equation. The reconstruction of concentration profiles follows after reconstruction of the velocity profiles. The resulting mass flux of transported species to the wafer surface is evaluated in the chemistry module and processed data fields–both area and their volumetric counterparts–are written out.

Three simulation cases, see table 6.1, based on the studies of silicon etching with an excentric medium application conducted by TU Graz are defined for the chemistry model. The cases 4a and 4b originate from the work of Burns et al.[16]. The case 4c has its process parameters closer to the ones used in the semiconductor industry. All three cases have a static inlet and very quickly develop a stationary solution. The cases are used to demonstrate capabilities of the presented chemistry model and for comparisons of etching profiles with varying etching times.

The case 4a, see figure 6.3, is an excentric impingement case with the radial excentricity $\Delta r = 55$mm. The disc is fully coated with the thin film and a distinctive wave, a hydraulic jump, across the disc radius forms. A high-velocity camera photo, courtesy of TU Graz, visually confirms the wave shape. The flow is considered laminar with Re lower as 1300. The wave front holds due to its height profile a higher concentration of nitric acid. Areas outside of the wave formation are considerably thinner what has a huge influence on the reaction rate R in the current model. Especially the wave upstream zone has up to twice higher reaction rate as the downstream area.

The second case, the case 4b, see figure 6.4, is having an increased excentricity to $\Delta r = 95$mm opposite to the case 4a. The induced flow forms a large dry spot of approximately 30mm radius at the centre of the wafer clearly visibly on the high-velocity camera still, courtesy of TU Graz. It should be noted that TFA-model is expressing the dry spot with an extremely thin film only. The film height of zero would lead to the jump discontinuity in the underlaying model equations. The flow is again laminar with Re not exceeding 1300. The concentration of the nitric acid outside of the hydraulic jump is much more even resulting in a more homogeneous reaction rates upstream and downstream of the hydraulic jump. Unfortunately the

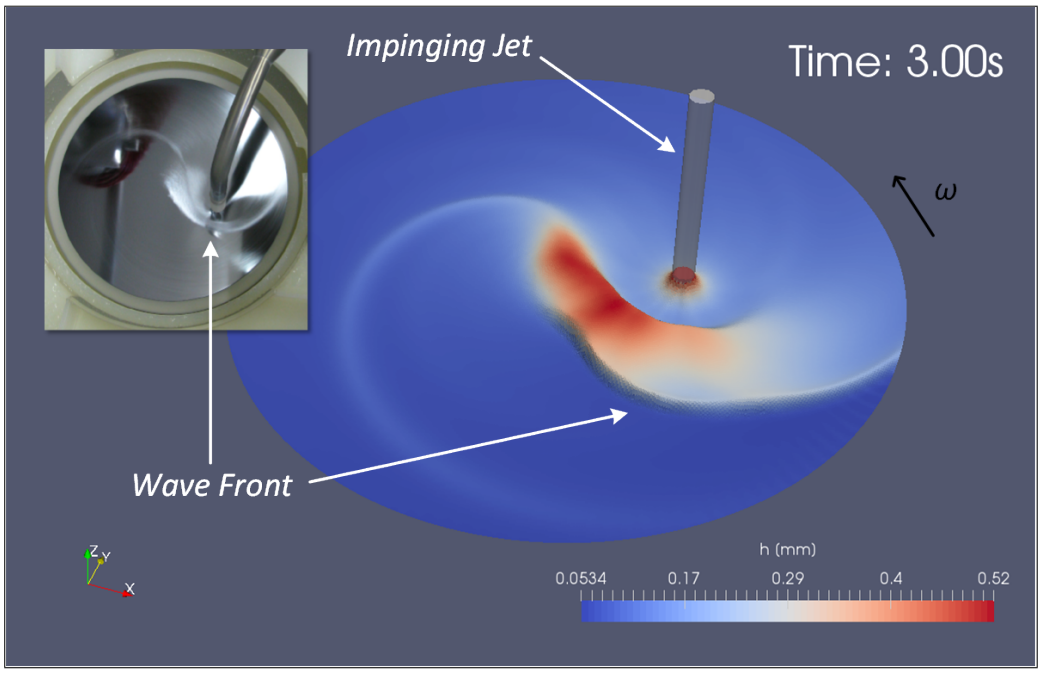

(a) Film relief (2D TFA): z-axis scaled 30×; photograph courtesy of TU Graz

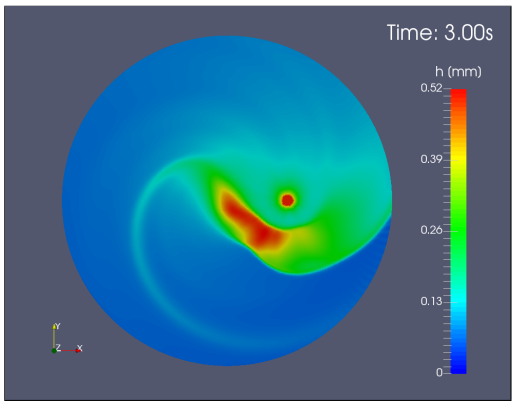

(b) Film height (2D TFA)

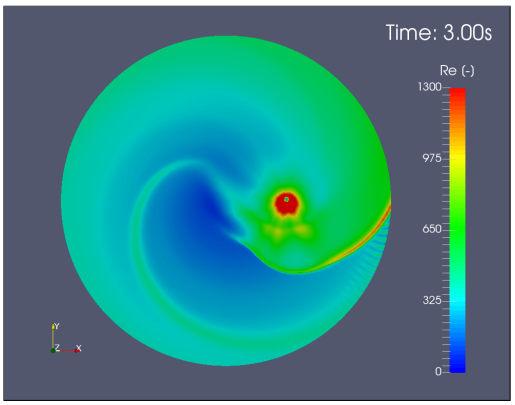

(c) Reynolds number (2D TFA)

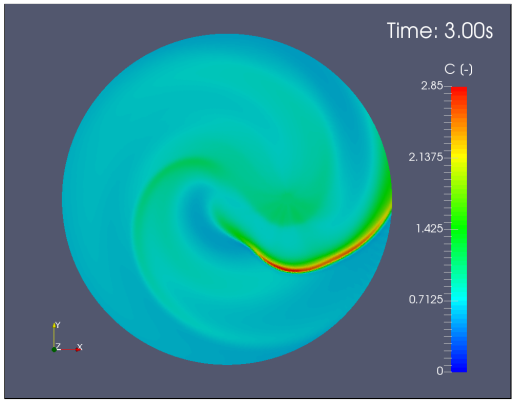

(d) Mean concentration (2D TFA)

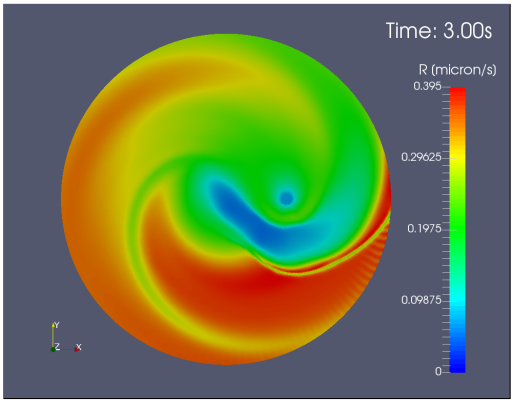

(e) Reaction rate (2D TFA)

Figure 6.3: Case 4a: $\Delta r = 55\text{mm}$, $\nu = 1 \times 10^{-6}\text{m}^2\,\text{s}^{-1}$, $Q = 2.8\text{lpm}$, $\omega = 400\text{rpm}$

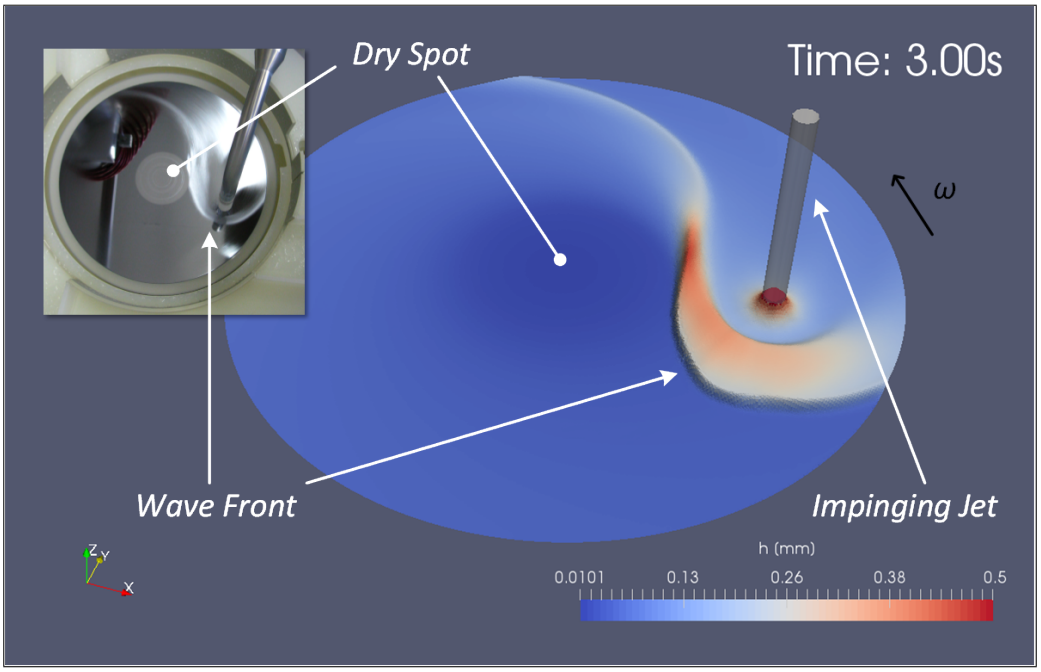

(a) Film relief (2D TFA): z-axis scaled 30×; photograph courtesy of TU Graz

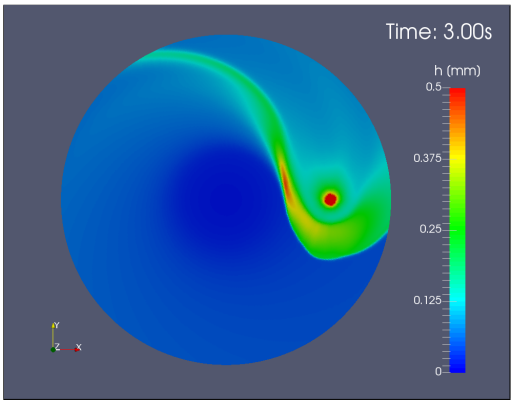

(b) Film height (2D TFA)

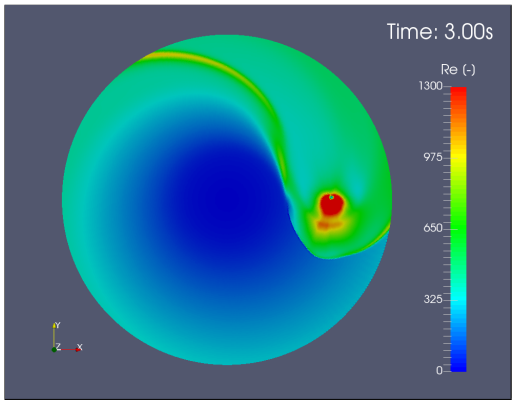

(c) Reynolds number (2D TFA)

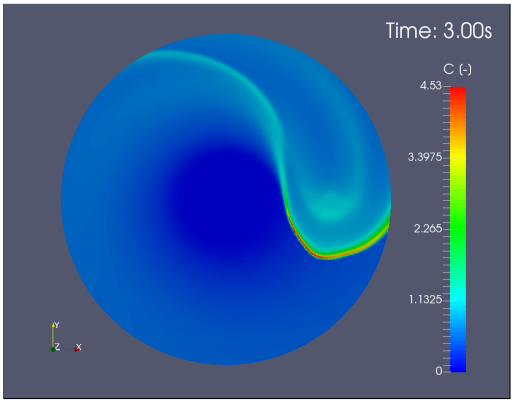

(d) Mean concentration (2D TFA)

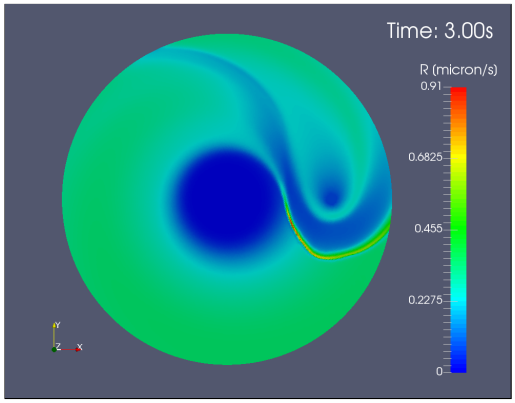

(e) Reaction rate (2D TFA)

Figure 6.4: Case 4b: $\Delta r = 95\text{mm}$, $\nu = 1 \times 10^{-6}\text{m}^2\,\text{s}^{-1}$, $Q = 2.8\text{lpm}$, $\omega = 400\text{rpm}$

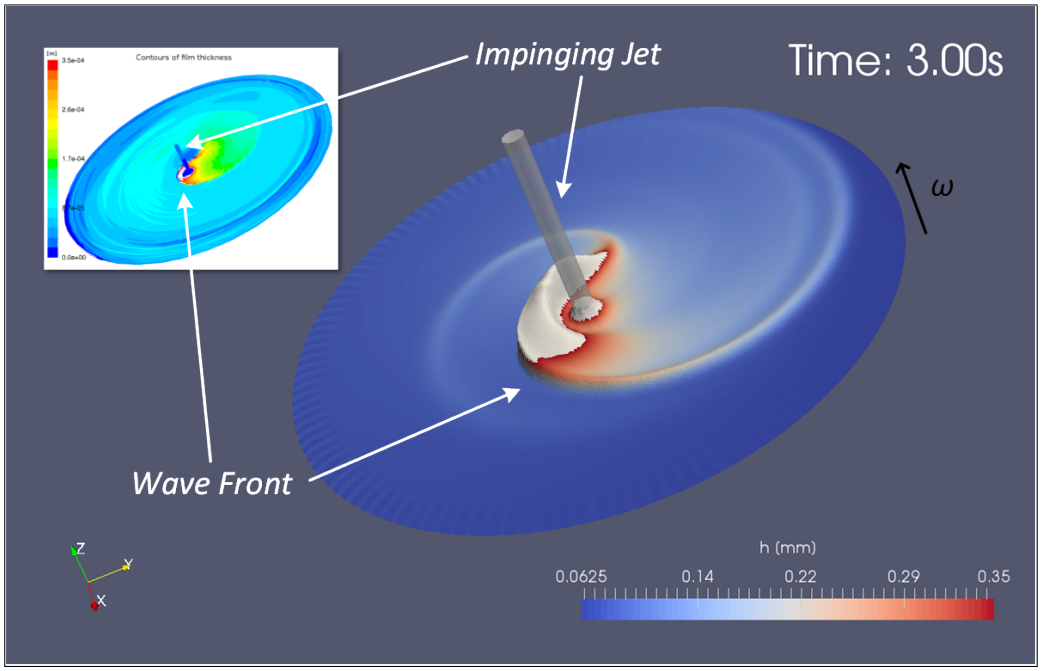

(a) Film relief (2D TFA): z-axis scaled 30×; 3D VoF solution courtesy of TU Graz

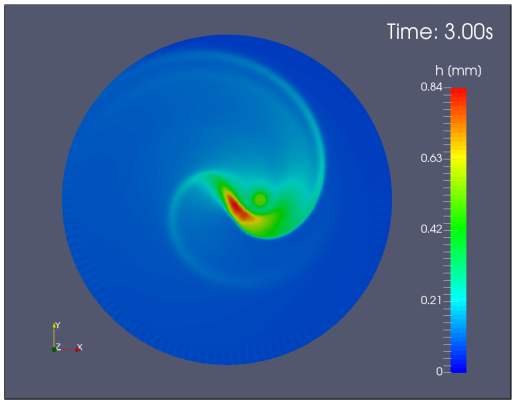

(b) Film height (2D TFA)

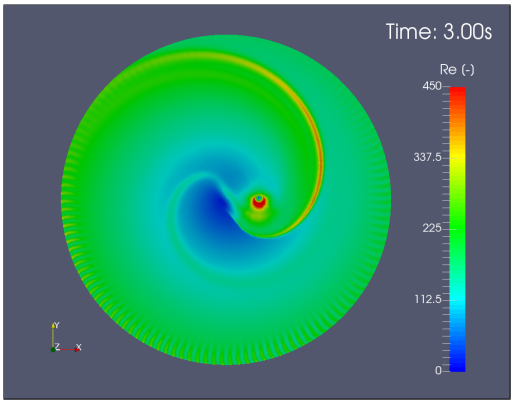

(c) Reynolds number (2D TFA)

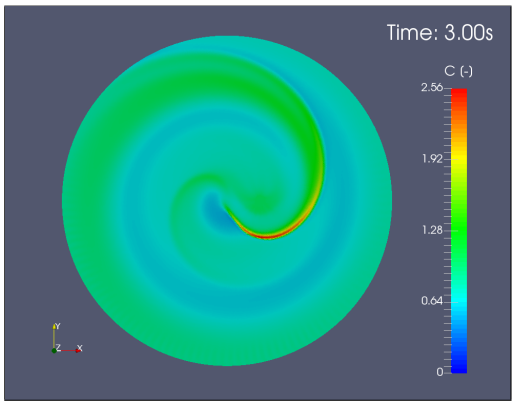

(d) Mean concentration (2D TFA)

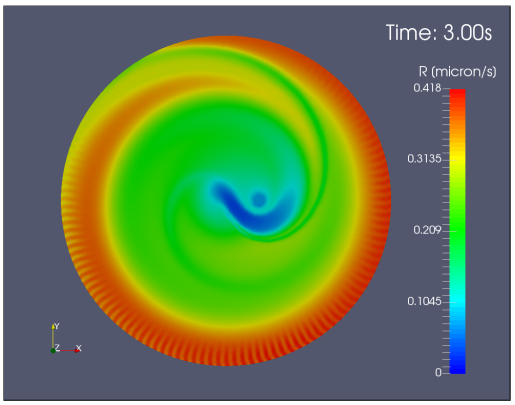

(e) Reaction rate (2D TFA)

Figure 6.5: Case 4c: $\Delta r = 30\text{mm}$, $\nu = 2.87 \times 10^{-6}\text{m}^2\,\text{s}^{-1}$, $Q = 1.5\text{lpm}$, $\omega = 500\text{rpm}$

dry spot wrecks the uniformity of the etching process and thus the given process configuration has no use for semiconductor industry.

The last simulation, the case 4c, develops a hydraulic jump of roughly a half radius size, see figure 6.5. The thin film approximation can be validated on hand of 3D VoF simulation, courtesy of TU Graz, that has however the peak values of the hydraulic jump cut off. The flow regime is laminar with Re nearly three times lower as in the cases 4a and 4b. The higher rotational speed, compared to the previous cases, of 500rpm causes a very thin film at the zone around the disc edge. As a result the case shows etching rates up to twice higher at the outside disc zone as in the centre.

There are some issues hidden in parameters of the chemistry model, namely an exact composition and properties of the etching solution and the reaction rate correction factor β.

Reported experiments usually provide reaction rates however are sparse on the etching data. The enchant composition is often not publicly accessible. That represents a serious problem in the definition of proper values of the diffusion coefficient D and the inlet mass fraction of nitric acid. Therefore the literature value of $D = 2.4 \times 10^{-9} \mathrm{m}^2\,\mathrm{s}^{-1}$ for the diffusion of nitric acid HNO_3 in a dilute aqueous solution by D'Ans[25] was used for the first. The inlet mass fraction c_{inlet} that directly scales the etching rate is unknown and was set, for simplicity, to 1.

The second problem is the reaction rate correction coefficient β that has to be fitted to experimental data. If the comparison against other experiments or models has to be done, the result has to be fitted to the target data.

Reported experiments are often in central impingement configurations only in order to be validated against 2D axisymmetric simulations or analytical models, for example Staudegger et al.[99]. That is basically a workaround to avoid expensive 3D calculations. Public data for an excentric impingement or even a dynamically moving inlet are very rare if not non-existent.

Furthermore the experimental data are often burdened by a hard-to-estimate error, as discussed by Kaneko et al.[53], as it is simply not possible to maintain a perfect axisymmetric flow configuration in experiments due to shape of ducts and nozzles, alignment of the centre axes of various components and at last due to the jet velocity distribution itself.

The uncertainty in the model parameters and the lack of data on the excentric impingement makes comparison of the simulation results with literature or experiments impossible, only the trends could be compared at the best.

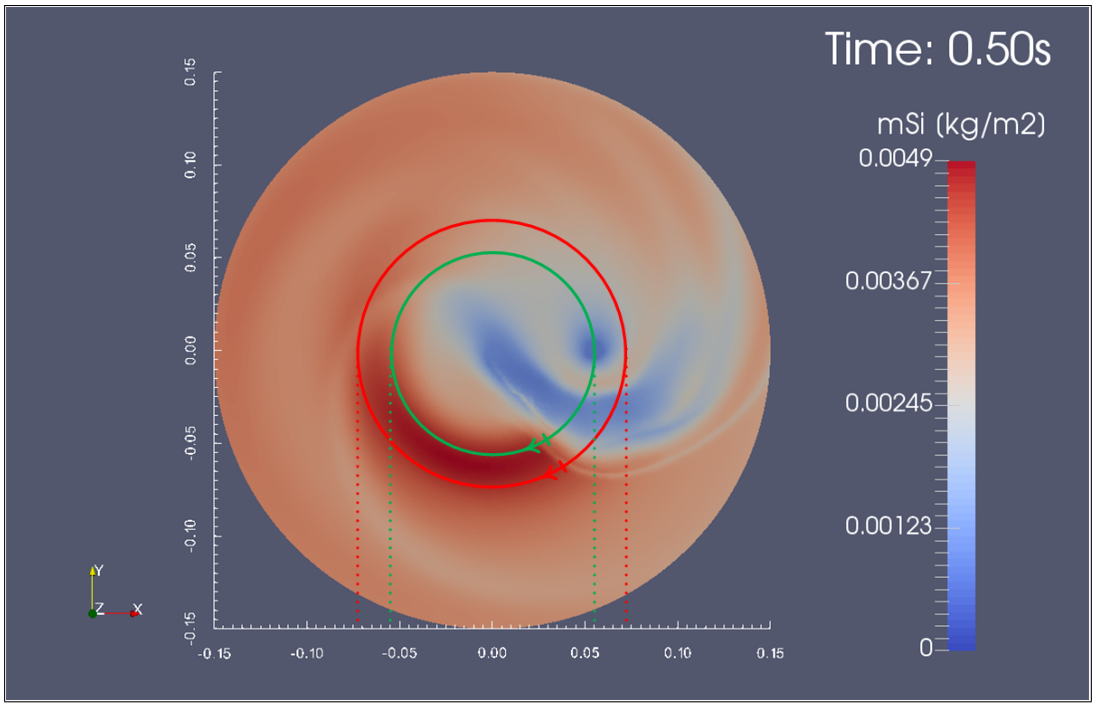

Figure 6.6: Case 4a: Etched silicon mass; green circumference passes through the impinging jet, red circumference marks the maximal mean circumferential etched mass

6.3.1 Disc Etching Profile

One of the important aspects of the wet etching process is the need for as uniform etching of the surface as possible. The usual approach to evaluate the uniformity of the etching process is plotting of the etching rates of the fully developed fluid flow against the disc radius. This approach has its limitations and is usually found in the 2D axisymmetric simulations with the central impingement.

However, plotting of the etching rates against disc radius is not suitable for the transient simulations with the dynamic inlet moving freely over the disc where the etching rates are changing all the time. As the disc under the fluid film is rotating, the etched surface is periodically changing as well. Therefore a different way for evaluation of etching uniformity has to be used.

The silicon mass m_{Si} etched out during the chemical reaction, see figure 6.6, can be determined by solving an equation

$$\frac{\partial m_{\mathrm{Si}}}{\partial t} = R\rho_{\mathrm{Si}} \tag{6.22}$$

The etched mass allows to define a mean circumferential etched mass of silicon $\overline{m}_{\mathrm{Si}\,r}$ as an average of the etched silicon mass along a disc circumference of the given radius r

$$\overline{m}_{\mathrm{Si}\,r} = \frac{1}{N_r}\sum_{N_r} m_{\mathrm{Si}} \quad \forall \mathrm{cell} : x^2 + y^2 = r^2 \tag{6.23}$$

where N_r is the number of cells along the circumference of the radius r and every cell contributes to only one circumferential etched mass average in order to satisfy the global mass balance

$$\sum \overline{m}_{\mathrm{Si}\,r} = \sum m_{\mathrm{Si}} \tag{6.24}$$

A corrected standard deviation of the etched silicon mass $s_{\mathrm{Si}\,r}$ along the circumference of the radius r is than defined as

$$s_{\mathrm{Si}\,r} = \sqrt{\frac{1}{(N_r - 1)} \sum_{N_r} \left(m_{\mathrm{Si}} - \overline{m}_{\mathrm{Si}\,r}\right)^2} \tag{6.25}$$

and describes the non-uniformity of the etching process along the circumference.

The evaluation of the mean circumferential etched mass of silicon along the concentric rings of the given radii is depicted on the figure 6.7. The plot depicts the evaluation of the mean circumferential silicon etched mass $\overline{m}_{\mathrm{Si}\,r}$ and its corrected standard deviation $s_{\mathrm{Si}\,r}$. The corrected standard deviation expresses how much the values along the circumference vary. The higher the corrected standard deviation the less uniform the etching along the circumference of the given radius is.

Finally, the mean circumferential etched mass $\overline{m}_{\mathrm{Si}\,r}$ normalised against the process time t

$$\dot{\overline{m}}_{\mathrm{Si}\,r} = \frac{\overline{m}_{\mathrm{Si}\,r}}{t} \tag{6.26}$$

can be used to evaluate the uniformity of the etching process for any process configuration including a dynamic inlet. The plot of the normalised mean circumferential etched mass of silicon $\dot{\overline{m}}_{\mathrm{Si}\,r}$ against the wafer radius r is than called an *etching profile*.

Examples of the etching profiles for the simulation cases 4a, 4b and 4c are given in the figure 6.8. The two etching profiles for the case 4a capture the etching difference between the disc flooding phase and the fully developed stationary flow. The etching profile of the case 4b clearly shows the dry spot at the centre area of the disc. The varying simulation times are demonstrating the time independence of the etching profiles.

6.4 Summary and Discussion

The simple chemistry model for the thin film was presented. The model allows to evaluate etching rates of the diffusion driven chemical reactions. The extension step from the etching rate to the etching profile helps to quickly compare the various process parameters.

The etching solution is generally invalid due to the broken assumptions placed on the TFM in the impingement area and in the vicinity of the hydraulic jump.

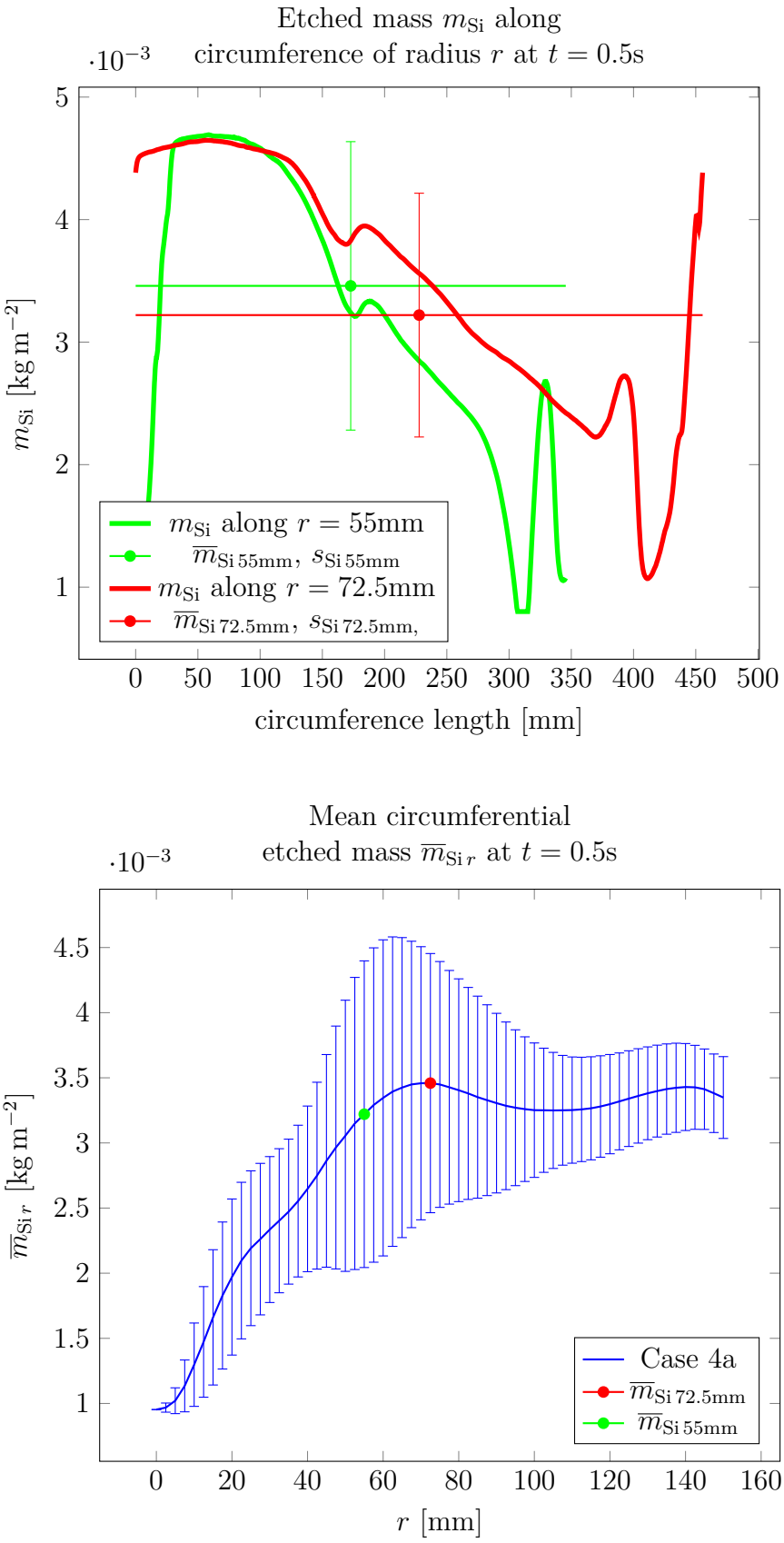

Figure 6.7: Case 4a: Mean circumferential silicon etched mass

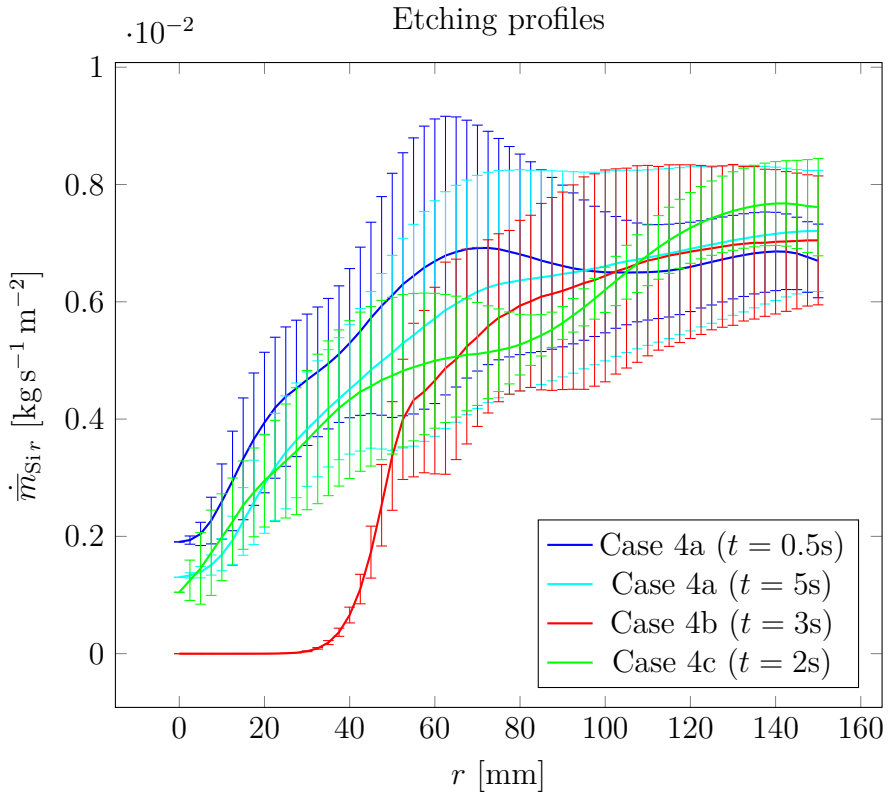

Figure 6.8: Etching profiles: Cases 4a, 4b and 4c with varying process lengths

The etching rates are definitely invalid in the impingement area. While the momentum and the film height are prescribed in the inlet, based on the 3D VoF-simulation, the etching rate is being derived from the given film height in the case of the chemistry model. The film height is usually much higher as the rest of the thin film in the impingement area what leads to very low etching rates in the current model contrary to the experimental measurements. The impingement area, in reality, has always the highest etching rate as the z-momentum of the jet transports the etching solution directly into the disc surface.

The dependency of the reaction rate on the thin film height is the weak spot of the chemistry model current formulation and is connected to the assumption of the concentration boundary layer δ_C being identical with the thin film free-surface and the current selection concentration profiles.

The disc areas with a very thin film are providing a good approximation which can be well compared and fitted to the experimental data with help of reaction rate correction factor β. The centrifugal forces that thin the film out are a huge factor and the higher rotational speeds thus generally improve the approximation. On the contrary, an increase in the film height is connected to the larger error in the parabolic concentration profile model. It is worthy to investigate as well different options, for example, a logarithmic concentration profile function

$$\hat{C}(\xi) = \beta \ln(\xi) \tag{6.27}$$

which would certainly improve the profile modelling.

Surprisingly, the profile modelling error mentioned above is masked in the hydraulic jump where the boundary layer separation significantly limits the transport of the etching solution into the disc and etching rates locally drops. This is indeed validated in experiments and mimicked by the erroneous concentration profile model as the hydraulic jump increases the film height.

The presented chemistry model can be used as a simple tool for the evaluation of the uniformity of the etching process and can provide a good approximation of the etching if its limitations are kept in mind.

Chapter 7

Summary and Conclusion

The main focus of the work was an investigation of the thin film flow on a rotating disc which has numerous industrial applications. It was demonstrated that standard 3D VoF simulations are impractical for real life applications. The spatial and temporal resolutions needed in the simulation of industrial processes lead to excessively long simulation times that severely limit the application of the classic numerical approaches. Industrial processes featuring a dynamic fluid impingement, multiple inlets with complex trajectories, involving chemical reactions and long process times are still beyond the economical feasibility of the classic methods.

The thesis suggests an alternative approach to the thin film simulation based on the well established integral method that reduces the problem complexity by reduction of its dimensionality. The derivation of the Thin Film Model recognises an importance of inertial and centrifugal forces in the presence of the spinning disc. An innovative application of Reynolds decomposition coupled with profile function modelling that allows to capture a crucial contribution of the inertial and centrifugal forces in the advective term is presented.

The derived TFM model is implemented using Finite Area method, a two-dimensional specialisation of the Finite Volume method for film flows on curved three-dimensional surfaces. The solver was conceived as a transient incompressible code with a dynamic inlet implementation that can be easily extended by additional models. A primer on the FA method and details on the solver implementation are given.

The developed solver is applied on realistic problems, both central and excentric impingement configurations, that locally invalidate some of TFM model assumptions. The result of the such application, called a Thin Film Approximation, is carefully evaluated in a comparison with the classic 3D VoF simulation performed in a commercial CFD code.

Results of the comparisons are very informative. Generally a very good agreement of the 2D TFA results with the 3D VoF simulation is achieved in a fraction of

computational resources. Where 3D VoF method needs months, 2D TFA approach needs merely few hours.

There exists only few problematic zones–the hydraulic jump, the impingement area–that show discrepancy in the solution at the moment.

The hydraulic jump is connected to the reversed flow and poses a challenge in the current model. The solution of the hydraulic jump is burdened by an error due to the vertical momentum transport. However, it has to be noted that the error is localised to only a small area containing the separation bubble where the velocity profile models fail to capture the proper shear stress contribution. The mass conservation together with the separation bubble locality keep the solution outside of the hydraulic jump untouched.

A similar problem is occurring in the impingement area. Unfortunately the dominance of the vertical momentum in the impinging jet cannot be resolved by TFM model and the solution in the impingement area has to be prescribed by other means. The surrounding of the impingement area is influenced by the lack of the film flow feedback in the current model. However the comparisons show that an assumption of the inlet influence being dominant hold well and the error in the impingement area is generally acceptable.

The lack of the surface waviness that is connected to the neglected cross flow in the vertical direction is specific for the integral methods and has to be mentioned in comparison to the 3D VoF results.

The TFA validation struggles with a dynamic inlet implementation due to lack of data to compare with. The dynamic inlet feature opens new, till now unseen, possibilities for the numerical simulation of the thin films. Considering the solver high performance and the fact that most industrial applications are tightly connected to the dynamic impingement, the TFA solver can be used as a rapid simulation tool for an optimisation of industrial process.

The thesis closes with an extension of the TFA solver with a simple chemistry model for a wet diffusion-controlled etching. The chemistry model is derived, implemented and shortly discussed. An evaluation method for the etching of the rotating disc is suggested. The presented chemistry model can be used, based on the experimental calibration, for the evaluation of the uniformity of the disc etching processes.

Concluding the goals of the thesis, it can be stated that the main goal, the development and validation of a high-performance tool for the transient numerical simulation involving the dynamic inlet implementation was met. The TFA solver performance suggests the solver usability in the design and optimisation of the industrial devices involving the thin films on the spinning disc.

7.1 Future Work

There are two important aspects that have to be considered in further improvements–the solution accuracy and the solver performance. Both aspects have to be kept in balance.

Some of interesting ideas for future improvements and implementations follows:

- One of the main problems is the hydraulic jump. The solution of the hydraulic jump can be fixed by an improved velocity profile model that would account for the flow separation boundary. The hydraulic jump modelling in the integral methods have been extensively studied and interesting works, for example Bohr et al.[11] and Putkaradze[84], exist.

- The impingement area solution is at the current state prescribed based on the external solution what precludes an interaction of the thin film with the inlet outflow. The possible solution to the whole impingement area as such would be a segregated hybrid solver with a coupled 3D VoF impingement and 2D TFA solution.

  The coupling code would be responsible for the mapping of 3D VoF solution to the 2D TFA inlet and backward feedback in the mapping of the 2D TFA solution on the 3D VoF boundary conditions.

  The performance balance has to be considered. The inclusion of the 3D VoF solver would mean nothing more than a light-weight coarse impingement mesh in order of few thousand cells only. The goal is to get the best out of the both worlds for the smallest price.

- The transient nature of the TFA solver called for the selection of the PISO algorithm. The PISO algorithm is not using any under-relaxation of the solution and thus is generally bound to small Courant number ($C < 1$). There exist an hybrid algorithm between PISO and SIMPLE, called a PIMPLE. The idea behind the PIMPLE algorithm is a bigger time advancement, that is a higher Courant number, with the use of an under-relaxation to reach a stable solution in the new time step. An implementation of the PIMPLE algorithm could certainly be considered.

- Thin film model can be extended by an implementation of the energy equation that could enhance transport coefficients, modelling of surface tension force and/or chemistry modelling.

- The simple chemistry model could have implemented a different concentration profile model based on the logarithmic profile function that would better model the concentration boundary layer δ_C.

Finally, the necessity of a thorough validation of all code changes against more comprehensive data, be it experiments or numerical simulations, does not need to be pointed out.

Appendix A

Solution of Polynomial Profiles

A.1 Polynomial Velocity Profiles

The solution of the polynomial velocity profile function $\hat{\mathbf{u}}$

$$\begin{aligned} \hat{\mathbf{u}}(\xi) &= \mathbf{a}_0 + \mathbf{a}_1\xi + \mathbf{a}_2\xi^2 + \mathbf{a}_3\xi^3 \\ &\xi \in \langle 0, 1\rangle, z = h\xi \end{aligned} \tag{A.1}$$

where ξ is the normalised vertical coordinate is determined by the the set of four boundary conditions:

- No slip boundary condition at the disc

$$\begin{aligned} &\hat{\mathbf{u}}(\xi)|_{\xi=0} = \mathbf{u}_{\text{disc}} : \\ &\qquad (\mathbf{a}_0 + \mathbf{a}_1\xi + \mathbf{a}_2\xi^2 + \mathbf{a}_3\xi^3)|_{\xi=0} = \mathbf{u}_{\text{disc}} \\ &\qquad \boxed{\mathbf{a}_0 = \mathbf{u}_{\text{disc}}} \end{aligned} \tag{A.2}$$

- Influence of the pressure gradient at the film bottom

$$\begin{aligned} &\left.\frac{\partial^2\hat{\mathbf{u}}(\xi)}{\partial\xi^2}\right|_{\xi=0} = 0 : \\ &\qquad \left.\frac{\partial^2}{\partial\xi^2}(\mathbf{a}_0 + \mathbf{a}_1\xi + \mathbf{a}_2\xi^2 + \mathbf{a}_3\xi^3)\right|_{\xi=0} = 0 \\ &\qquad \left.\frac{\partial}{\partial\xi}(\mathbf{a}_1 + 2\mathbf{a}_2\xi + 3\mathbf{a}_3\xi^2)\right|_{\xi=0} = 0 \\ &\qquad (2\mathbf{a}_2 + 6\mathbf{a}_3\xi)|_{\xi=0} = 0 \\ &\qquad 2\mathbf{a}_2 = 0 \\ &\qquad \boxed{\mathbf{a}_2 = 0} \end{aligned} \tag{A.3}$$

- Von Neumann boundary condition at the free-surface

$$\begin{aligned} \left.\frac{\partial \hat{\mathbf{u}}(\xi)}{\partial \xi}\right|_{\xi=1} &= 0 \\ \left.\frac{\partial}{\partial \xi}(\mathbf{a}_0 + \mathbf{a}_1\xi + \mathbf{a}_2\xi^2 + \mathbf{a}_3\xi^3)\right|_{\xi=1} &= 0 \\ (\mathbf{a}_1 + 2\mathbf{a}_2\xi + 3\mathbf{a}_3\xi^2)|_{\xi=1} &= 0 \\ \mathbf{a}_1 + 2\mathbf{a}_2 + 3\mathbf{a}_3 &= 0 \end{aligned} \tag{A.4}$$

- Relation to the mean velocity

$$\begin{aligned} \int_0^1 \hat{\mathbf{u}}(\xi)\, d\xi = \overline{\mathbf{u}}: \\ \int_0^1 (\mathbf{a}_0 + \mathbf{a}_1\xi + \mathbf{a}_2\xi^2 + \mathbf{a}_3\xi^3)\, d\xi &= \overline{\mathbf{u}} \\ \left[\mathbf{a}_0\xi + \frac{\mathbf{a}_1}{2}\xi^2 + \frac{\mathbf{a}_2}{3}\xi^3 + \frac{\mathbf{a}_3}{4}\xi^4\right]_0^1 &= \overline{\mathbf{u}} \\ \mathbf{a}_0 + \frac{\mathbf{a}_1}{2} + \frac{\mathbf{a}_2}{3} + \frac{\mathbf{a}_3}{4} &= \overline{\mathbf{u}} \end{aligned} \tag{A.5}$$

Applying the solution A.3 into A.4 one can express the coefficient $\mathbf{a}_1$ as

$$\mathbf{a}_1 = -3\mathbf{a}_3 \tag{A.6}$$

Using the solutions A.2, A.3 and the substitution A.6 in A.5 yields

$$\begin{aligned} -\frac{3}{2}\mathbf{a}_3 + \frac{1}{4}\mathbf{a}_3 &= \overline{\mathbf{u}} - \mathbf{u}_{\text{disc}} \\ \boxed{\mathbf{a}_3 = -\frac{4}{5}\left(\overline{\mathbf{u}} - \mathbf{u}_{\text{disc}}\right)} \end{aligned} \tag{A.7}$$

Substituting the solution A.7 back into A.6 gives

$$\boxed{\mathbf{a}_1 = \frac{12}{5}\left(\overline{\mathbf{u}} - \mathbf{u}_{\text{disc}}\right)} \tag{A.8}$$

The polynomial coefficients than provide the solution of the polynomial velocity profile function $\hat{\mathbf{u}}$

$$\hat{\mathbf{u}}(\xi) = \mathbf{u}_{\text{disc}} + \left(\overline{\mathbf{u}} - \mathbf{u}_{\text{disc}}\right)\left(\frac{12}{5}\xi - \frac{4}{5}\xi^3\right) \tag{A.9}$$

A.2 Polynomial Concentration Profiles

The solution of the polynomial profile function $\hat{C}$ for the reactant concentration

$$\begin{aligned} \hat{C}(\xi) &= b_0 + b_1\xi + b_2\xi^2 \\ \xi &\in \langle 0,1\rangle, z = h\xi \end{aligned} \tag{A.10}$$

with ξ being the normalised vertical coordinate as in the case of the polynomial velocity profile function is given by the set of three boundary conditions:

- All the reactant is consumed in the etching reaction at the bottom

$$\begin{aligned} \hat{C}(\xi)|_{\xi=0} = 0 : \\ (b_0 + b_1\xi + b_2\xi^2)|_{\xi=0} &= 0 \\ \boxed{b_0 = 0} \end{aligned} \tag{A.11}$$

- Von Neumann boundary condition at the free-surface

$$\begin{aligned} \left.\frac{\partial \hat{C}(\xi)}{\partial \xi}\right|_{\xi=1} &= 0 \\ \left.\frac{\partial}{\partial \xi}(b_0 + b_1\xi + b_2\xi^2)\right|_{\xi=1} &= 0 \\ (b_1 + 2b_2\xi)|_{\xi=1} &= 0 \\ b_1 + 2b_2 &= 0 \end{aligned} \tag{A.12}$$

- Relation to the mean reactant concentration

$$\begin{aligned} \int_0^1 \hat{C}(\xi)\, d\xi = \overline{C} : \\ \int_0^1 (b_0 + b_1\xi + b_2\xi^2)\, d\xi &= \overline{C} \\ \left[b_0\xi + \frac{b_1}{2}\xi^2 + \frac{b_2}{3}\xi^3\right]_0^1 &= \overline{C} \\ b_0 + \frac{b_1}{2} + \frac{b_2}{3} &= \overline{C} \end{aligned} \tag{A.13}$$

The boundary condition A.12 with help of the solution A.11 can be used to express the coefficient b_1

$$b_1 = -2b_2 \tag{A.14}$$

Inserting A.11 together with A.14 into the last boundary condition A.13 provides

the solution

$$\begin{aligned} -b_2 + \frac{b_2}{3} &= \overline{C} \\ \boxed{b_2 = -\frac{3}{2}\overline{C}} & \end{aligned} \tag{A.15}$$

Substituting the solution A.15 back into A.14 yields

$$\boxed{b_1 = 3\overline{C}} \tag{A.16}$$

The solution of the polynomial concentration profile function $\hat{C}$ is then

$$\hat{C}(\xi) = 3\overline{C}\left(\xi - \frac{1}{2}\xi^2\right) \tag{A.17}$$

Appendix B

Important Formulas

B.1 Dimensionless Numbers

B.1.1 Reynolds Number

The Reynolds number (Re) quantifies the relative importance of inertial and viscous forces

$$\mathrm{Re} = \frac{\text{inertial forces}}{\text{viscous forces}} = \frac{\mathbf{u}L}{\nu} \tag{B.1}$$

where L denotes a characteristic length and ν is the kinematic viscosity.

The definition of the Reynolds number for the TFA solver follows

$$\mathrm{Re} = \frac{\|\overline{\mathbf{u}}\|\, h}{\nu} \tag{B.2}$$

where h represents the characteristic length of the thin film.

B.1.2 Froude Number

The Froude number (Fr) is defined as the ratio of inertial forces to external field

$$\mathrm{Fr} = \frac{\text{inertial forces}}{\text{external field}} = \frac{\mathbf{u}}{\sqrt{gL}} \tag{B.3}$$

where $\mathbf{g}$ is the gravity and the external field characteristic in one.

The Froude number definition for the TFA solver

$$\mathrm{Fr} = \frac{\|\overline{\mathbf{u}}\|}{\sqrt{\|\mathbf{g}\|\, h}} \tag{B.4}$$

can be used to judge a *subcritical*, $\mathrm{Fr} < 1$, and *supercritical*, $\mathrm{Fr} < 1$, flow of the thin film. Note that the hydraulic jump is possible only in supercritical flows.

B.1.3 Courant Number

The Courant number (C), connected to Courant-Friedrichs-Lewy (CFL) condition, describes how information spread in the discretized problem domain

$$\mathrm{C} = \frac{\mathbf{u}\Delta t}{\Delta x} \tag{B.5}$$

where $\mathbf{u}$ describes information velocity, Δx is the length interval and Δt represents the time step.

The Courant number derivate for the TFA solver is defined as

$$\mathrm{C} = \frac{(\overline{\mathbf{u}})_e \Delta t}{\|\mathbf{l}\|} \tag{B.6}$$

where $(\overline{\mathbf{u}})_e$ denotes the interpolation of the mean velocity at the edge and $\mathbf{l}$ is the edge length vector.

B.2 Math Formulas

B.2.1 Gauss' Divergence Theorem

Let V be a subset of $\mathbb{R}^n$ which is compact and has a piecewise smooth boundary S, also indicated with ∂V, that is oriented by an outward pointing unit normal field $\mathbf{n}$. If $\mathbf{F}$ is a continuously differentiable vector field defined on an open set U, such that $V \subseteq U$, then

$$\int_V \nabla \bullet \mathbf{F}\, d^{(n)}V = \oint_{\partial V} \mathbf{F} \cdot \mathbf{n}\, d^{(n-1)}S \tag{B.7}$$

see Forster[33] for details.

B.2.2 Leibniz Integral Rule

Let $f(t, x)$ be a function such that both $f(t, x)$ and its partial derivative $\frac{\partial}{\partial x} f(t, x)$ are continuous in t and x in some region of the (t, x)-plane, including

$$\begin{aligned} a(x) \leq & t \leq b(x) \\ x_0 \leq & x \leq x_1. \end{aligned}$$

Further suppose that the functions $a(x)$ and $b(x)$ are both continuous and both have continuous derivatives $a'(x)$ and $b'(x)$ for $x_0 \leq x \leq x_1$.

Then for $x_0 \leq x \leq x_1$

$$\begin{aligned} \frac{d}{dx}\left(\int_{a(x)}^{b(x)} f(t,x)\,dt\right) &= \int_{a(x)}^{b(x)} \frac{\partial}{\partial x} f(t,x)\,dt \\ &\quad + \Big\{ f\left(b(x),x\right) b'(x) - f\left(a(x),x\right) a'(x) \Big\}, \end{aligned} \tag{B.8}$$

see Flanders[32] for details.

Bibliography

[1] Rohan Abeyaratne. Continuum mechanics: Volume II of lecture notes on the mechanics of elastic solids. Technical report, MIT Department of Mechanical Engineering, 2012.

[2] ANSYS, Inc. *ANSYS Fluent Theory Guide Release 13.0*, November 2010.

[3] Rutherford Aris. *Vectors, Tensors and the Basic Equations of Fluid Mechanics*. Dover Publications, 1989.

[4] Timothy Barth. Numerical aspects of computing high Reynolds number flows on unstructured meshes. Technical report, NASA, Ames Research Center, Moffett Field, CA, 1991.

[5] S. Basu and B. M. Cetegen. Analysis of hydrodynamics and heat transfer in a thin liquid film flowing over a rotating disk by the integral method. *Journal of Heat Transfer*, 128:217–225, 2006.

[6] G. K. Batchelor. *An Introduction to Fluid Dynamics*. Cambridge University Press, reprint of 1967 edition, 2002.

[7] T. Benjamin. Wave formation in laminar flow down an inclined plane. *Journal of Fluid Mechanics*, 2(6):554–573, 1957.

[8] D. Benney. Long waves on liquid films. *Journal of Mathematical Physics*, 45(2):150–155, 1966.

[9] A. Binnie. Instability in a slightly inclined water channel. *Journal of Fluid*, 5(4):561–570, 1959.

[10] J. Blazek. *Computational Fluid Dynamics: Principles and Applications*. Elsevier, first edition edition, 2001.

[11] Tomas Bohr, Vachtang Putkaradze, and Shinya Watanabe. Averaging theory for the structure of hydraulic jumps and separation in laminar free-surface flows. *Phys. Rev. Lett.*, 79(6):1038–1041, Aug 1997.

[12] J. P. Boris and D. L. Book. Flux-corrected transport. I. SHASTA, a fluid transport algorithm that works. *Journal of Computational Physics*, 11(1):38–69, January 1973.

[13] J. U. Brackbill, D. B. Kothe, and C. Zemach. A continuum method for modeling surface tension. *Journal of Computational Physics*, 100:335–354, 1992.

[14] A. Bunov, E. Demekhin, and V. Shkadov. On the non-uniqueness of nonlinear wave solutions in a viscous layer. *Journal of Applied Mathematics and Mechanics*, 48(4):495–499, 1984.

[15] Guido Buresti. A note on Stokes' hypothesis. *ACTA MECHANICA*, 2015.

[16] J. R. Burns, C. Ramshaw, and R. J. Jachuck. Measurement of liquid film thickness and the determination of spin-up radius on a rotating disc using an electrical resistance technique. *Chemical Engineering Science*, 58:2245–2253, 2003.

[17] John W. M. Bush and Jeffrey M. Aristoff. The influence of surface tension on the circular hydraulic jump. *Journal of Fluid Mechanics*, 489:229–238, 2003.

[18] L. S. Caretto, R. M. Curr, and D. B. Spalding. Two numerical methods for three-dimensional boundary layers. *Computer Methods in Applied Mechanics and Engineering*, 1(1):39–57, June 1972.

[19] CD adapco Group. *Comet, Version 2.000 - User Manual*, 2000.

[20] Tuncer Cebeci and Peter Bradshaw. *Momentum Transfer in Boundary Layers*. Thermal and Fluids Engineering. Hemisphere Publishing Corporation, 1977.

[21] H.-C. Chang and E.A. Demekhin. *Complex Wave Dynamics on Thin Films*. Elsevier, 2002.

[22] A. F. Charwat, R. E. Kelly, and C. Gazley. The flow and stability of thin liquid films on a rotating disk. *Journal of Fluid Mechanics*, 53(2):227–255, 1972.

[23] R.V. Craster and O. K. Matar. Dynamics and stability of thin liquid films. *Review of Modern Physics*, 81(3), 2009.

[24] Santiago Márquez Damián. *An Extended Mixture Model for the Simultaneous Treatment of Short and Long Scale Interfaces*. PhD thesis, Universidad Nacional del Litoral, 2013.

[25] Jean D'Ans and Ellen Lax. *Taschenbuchchenbuch für Chemiker und Physiker*. Springer Science + Business Media, 1983.

[26] Clint Dawson and Christopher M. Mirabito. The shallow water equations. Technical report, Institute for Computational Engineering and Sciences, University of Texas, Austin, September 2008. slides.

[27] Yannis Dimakopoulos, George Karapetsas, Nikolaos A. Malamataris, and Evan Mitsoulis. The free (open) boundary condition at inflow boundaries. *Journal of Non-Newtonian Fluid Mechanic*, 187-188:16–31, 2012.

[28] Youngs D.L. Time-dependent multi-material flow with large fluid distortion. *Numerical Methods for Fluid Dynamics*, pages 273–285, 1982.

[29] H. Espig and R. Hoyle. Waves in a thin liquid layer on a rotating disk. *Journal of Fluid Mechanics*, 22(4):671–677, 1965.

[30] Robert Eymard, Thierry Gallouët, and Raphaèle Herbin. *Handbook of Numerical Analysis*, volume 7, chapter Finite Volume Methods, pages 713–1020. North-Holland, Amsterdam, 2000.

[31] Joel H. Ferziger and Milovan Perić. *Computational Methods for Fluid Dynamics*. Springer Science + Business Media, 2002.

[32] Harley Flanders. Differentiation under the integral sign. *The American Mathematical Monthly*, 80(6):615, June 1973.

[33] Otto Forster. *Analysis 3: Integralrechnung im IR^n mit Anwendungen*. Springer Science + Business Media, 1983.

[34] Mathieu Foucaud, Philippe Garnier, Vincent Joseph, Erwine Pargon, Névine Rochat, and Raluca Tiron. Surface preparations impact on 248nm deep uv photo resists adhesion during a wet etch. *Solid State Phenomena*, 195:58–61, 2013.

[35] Sam Fredriksson. A buoyantBoussinesqSurfactantFoam tutorial: an introduction to FAM. Technical report, Chalmers University of Technology, 2011.

[36] Mohamed Gad-el-Hak. Questions in fluid mechanics: Stokes' hypothesis for a newtonian, isotropic fluid. *Journal of Fluids Engineering*, 117:3–5, 1995.

[37] Andrzej Gajewski. Contact angle and sessile drop diameter hysteresis on metal surfaces. *International Journal of Heat and Mass Transfer*, 51(19-20):4628–4636, 2008.

[38] D. Gao, N.B. Morley, and V. Dhir. Numerical simulation of wavy falling film flow using VoF method. *Journal of Computational Physics*, 192(2):624–642, 2003.

[39] V. R. Gopala and B. G. M. van Wachem. Volume of fluid methods for immiscible-fluid and free-surface flows. *Chemical Engineering Journal*, 141(1-3):204–221, 2008.

[40] C. J. Grant, J. M. Sharrow, and J. J. Snyder. Method and apparatus for etch rate uniformity control, 2006. US Patent 6.992.014.

[41] Bernhard F. W. Gschaider, Doris Prieling, Helfried Steiner, and Petr Víta. Thin film simulation on a rotating wafer. Presentation at 3rd Meeting of the Austrian OpenFOAM User Group, Leoben, October 2011.

[42] Bernhard F. W. Gschaider, Petr Víta, Doris Prieling, and Helfried Steiner. Liquid coverage of rotating discs: A comparison of solvers and approaches. Presentation at 5th OpenFOAM® Workshop, Gothenburg, June 2010.

[43] M.E. Gurtin. *An Introduction to Continuum Mechanics*. Mathematics in Science and Engineering. Elsevier Science, 1982.

[44] F. H. Harlow and P. I. Nakayama. Transport of turbulence energy decay rate. Technical Report Report LA 3854, Los Alamos National Laboratory, January 1968.

[45] Charles Hirsch. The basic equations of fluid dynamics. In *Numerical Computation of Internal and External Flows*, pages 27–64. Elsevier BV, 2007.

[46] C.W Hirt and B.D Nichols. Volume of fluid (VoF) method for the dynamics of free boundaries. *Journal of Computational Physics*, 39(1):201–225, jan 1981.

[47] R. I. Issa. Solution of the implicitly discretised fluid flow equations by operator-splitting. *Journal of Computational Physics*, 62(1):40–65, 1985.

[48] R. I. Issa, A. D. Gosman, and A. P. Watkins. The computation of compressible and incompressible recirculating flows by a non-iterative implicit scheme. *Journal of Computational Physics*, 62(1):66–82, January 1986.

[49] H. Jasak and H. G. Weller. Interface tracking capabilities of the inter-gamma differencing scheme. Technical report, Department of Mechanical Engineering Imperial College of Science, Technology and Medicine, London, February 1995.

[50] Hrvoje Jasak. *Error Analysis and Estimation for the Finite Volume Method with Applications to Fluid Flows*. PhD thesis, Imperial College of Science, Technology and Medicine, Department of Mechanical Engineering, June 1996.

[51] Hrvoje Jasak, Aleksandar Jemcov, and Željko Tuković. OpenFOAM: A C++ library for complex physics simulations. Technical report, Wikki Ltd, United Kingdom, 2007.

[52] Markus Junk, Frank Holsteyns, Felix Staudegger, Christiane Lechner, Hendrik Kuhlmann, Doris Prieling, Helfried Steiner, Bernhard Gschaider, and Petr Vita. Simulations of liquid film flows with free surface on rotating silicon wafers (RoWaFlowSim). In *The 10th International Conference on Modeling and Applied Simulation*, pages 149–154. Universita di Genova, September 2011. ISBN 978-88-903724-5-2.

[53] Kimihisa Kaneko, Akira Tamenori, Norbert Alleborn, and Franz Durst. Numerical and experimental investigation of wet chemical etching of silicon wafers. *ECS Transactions*, 2 (6):295–303, 2007.

[54] P. L. Kapitza and S. P. Kapitza. Wave flow of thin layers of a viscous liquid: III. experimental study of undulatory flow conditions. *Soviet Journal of Experimental and Theorethical Physics*, 19:105–120, 1949.

[55] Fabian Peng Kärrholm. Rhie-Chow interpolation in OpenFOAM. Technical report, Department of Applied Mechanics, Chalmers Univesity of Technology, Göteborg, Sweden, 2006. Appendix from Numerical Modelling of Diesel Spray Injection and Turbulence Interaction, by Fabian Peng Kärrholm, Chalmers University.

[56] Tae-Sung Kim and Moon-Uhn Kim. The flow and hydrodynamic stability of a liquid film on a rotating disc. *Fluid Dynamics Research*, 41(3):035504 (28pp), June 2009.

[57] Pijush K. Kundu and Ira M. Cohen. *Fluid Mechanics, Third Edition.* Academic Press, 2004.

[58] Lam Research Corporation webplatform. `http://www.lamresearch.com/`, 2016.

[59] B.E. Launder and D.B. Spalding. The numerical computation of turbulent flows. *Computer Methods in Applied Mechanics and Engineering*, 3(2):269–289, March 1974.

[60] Seung-Jun Lee and In Lee. The unified fluid solver for solid-liquid-gas interaction phenomenon. Transactions of the Korean Nuclear Society Spring Meeting, Taebaek, Korea, May 2011.

[61] B. P. Leonard. A stable and accurate convective modelling procedure based on quadratic upstream interpolation. *Computer Methods in Applied Mechanics and Engineering*, 19(1):59–98, jun 1979.

[62] B. P. Leonard. Simple high-accuracy resolution program for convective modelling of discontinuities. *International Journal for Numerical Methods in Fluids*, 8(10):1291–1318, oct 1988.

[63] I. Leshev and G. Peev. Film flow on a horizontal rotating disk. *Chemical Engineering and Processing: Process Intensification*, 42(11):925–929, 2003.

[64] J. Liu, J. Schneider, and J. Gollub. Three-dimensional instabilities of film flows. *Physics of Fluids*, 7(1):55–67, 1995.

[65] Nikos T. Malamataris and Tasos C. Papanastasiou. Unsteady free surface flows on truncated domains. *Industrial & Engineering Chemistry Research*, 30(9):2211–2219, 1991.

[66] O. K. Matar and C. J. Lawrence. Axisymmetric wave regimes in viscous liquid film flow over a spinning disc. *Journal of Fluid Mechanics*, 495:385–411, 2003.

[67] Evan Mitsoulis and Nikolaos A. Malamataris. The free (open) boundary condition with integral constitutive equations. *Journal of Non-Newtonian Fluid Mechanics*, 177-178:97–108, 2012.

[68] Y. Miyasaka. On the flow of a viscous free boundary jet on a rotating disk. *Bulletin of JSME*, 17:1461–1468, 1974.

[69] E. Momoniat and D. P. Mason. Investigation of the effect of the coriolis force on a thin fluid film on a rotating disk. *International journal of non-linear mechanics*, 33(6):1069–1088, 1998.

[70] S. Muzaferija, M. Peric, P. Sames, and T. Schelin. A two-fluid navier-stokes solver to simulate water entry. In *wenty-Second Symposium on Naval Hydrodynamics*, 1998.

[71] T. G. Myers and M. Lombe. The importance of the coriolis force on axisymmetric horizontal rotating thin film flows. *Chemical Engineering & Processing*, 45(2):90–98, 2006.

[72] D. J. Needham and J. H. Merkin. The development of nonlinear waves on the surface of a horizontally rotating thin liquid film. *Journal of Fluid Mechanics*, 184:357–379, 1987.

[73] W. Nusselt. Die oberflächenkondensation des wasserdampfes. *Zeitschrift des Vereins Deutscher Ingenieure*, 60:541–546, 1916.

[74] OpenFOAM webplatform. `http://openfoam.org/`, 2016.

[75] OpenFOAM extend project. `http://www.extend-project.de/`, 2016.

[76] B. Ozar, B. M. Cetegen, and A. Faghri. Experiments on the flow of a thin liquid film over a horizontal stationary and rotating disk surface. *Experiments in Fluids*, 34:555–565, 2003.

[77] T. C. Papanastasiou, N. Malamataris, and K. Ellwood. A new outflow boundary condition. *International Journal for Numerical Methods in Fluids*, 14:587–608, 1992.

[78] C. Park and T. Nosoko. Three-dimensional wave dynamics on a falling film and associated mass transfer. *AIChE Journal*, 49(11):2715–2727, 2003.

[79] Suhas V. Patankar. *Numerical Heat Transfer and Fluid Flow*. Computational and Physical Processes in Mechanics and Thermal Sciences. Hemisphere Publishing Corporation, 1980.

[80] Raad I. Issa Paulo J. Oliveira. An improved PISO algorithm for the computation of buoyancy-driven flows. *Numerical Heat Transfer, Part B: Fundamentals*, 40(6):473–493, December 2001.

[81] Titus Petrila and Damian Trif. *Basics of Fluid Mechanics and Introduction to Computational Fluid Dynamics*. Springer, 2005.

[82] Doris Prieling. *Computational Investigation of Liquid Film Flow on Rotating Disks*. PhD thesis, Graz University of Technology, 2013.

[83] Doris Prieling, Helfried Steiner, and Petr Víta. Numerical investigation of liquid film flow on a rotating disk. Presentation at Ercoftac ADA PC meeting, Vienna, November 2009.

[84] Vachtang Putkaradze. *Local Structures in Extended Systems*. PhD thesis, Niels Bohr Institute of Astronomy, Physics and Geophysics, University of Copenhagen, 1997.

[85] M. M. Rahman and A. Faghri. Numerical simulation of fluid flow and heat transfer in a thin liquid film over a rotating disk. *International Journal of Heat and Mass Transfer*, 35(6):1441–1453, 1992.

[86] David A. Randall. The shallow water equations. Technical report, Department of Atmospheric Science, Colorado State University, July 2006.

[87] J. W. Rauscher, R. E. Kelly, and J. D. Cole. An asymptotic solution for the laminar flow of a thin film on a rotating disk. *Journal of Applied Mechanics*, 40(1):43–47, 1973.

[88] C. M. Rhie and W. L. Chow. Numerical study of the turbulent flow past an airfoil with trailing edge separation. *AIAA Journal*, 21(11):1525–1532, November 1983.

[89] Jeremy Rice, Amir Faghri, and Baki Cetegen. Analysis of a free surface film from a controlled liquid impinging jet over a rotating disk including conjugate effects, with and without evaporation. *International Journal of Heat and Mass Transfer*, 48:5192–5204, 2005.

[90] Henrik Rusche. *Computational Fluid Dynamics of Dispersed Two-Phase Flows at High Phase Fractions*. PhD thesis, Imperial College of Science, Technology and Medicine, Department of Mechanical Engineering, Exhibition Road, London SW7 2BX, December 2002.

[91] C. Ruyer-Quil and P. Manneville. Improved modeling of flows down inclined planes. *The European Physical Journal B, Condensed Matter and Complex Systems*, 15(2):357–369, 2000.

[92] Ruben Scardovelli and Stephane Zaleski. Direct numerical simulation of free-surface and interfacial flow. *Annual Reviews Fluid Mechanics*, 31:567–603, 1999.

[93] B. Schwartz and H. Robbins. Chemical etching of silicon. *Journal of The Electrochemical Society*, 123(12):1903, 1976.

[94] Cüneyt Sert. Finite element analysis in thermofluids. Technical report, Middle East Technical University, 2014.

[95] V. Ya. Shkadov. Wave flow regimes of a thin layer of viscous fluid subject to gravity. *Izvestiia Akademii Nauk SSSR. Mekhanika Zhidkosti i Gaza*, 2(1):43–51, 1967.

[96] Jian-Jun Shu and Allen T. Chwang. Generalized fundamental solutions for unsteady viscous flows. *Phys. Rev. E*, 63(5):051201, 2001.

[97] G. Sisoev and V. Shkadov. On two-parametric manifold of the waves solutions of equation for falling film in viscous liquid. *Doklady Physics*, 44(7):454–459, 1999.

[98] R. P. Spiers, C. V. Subbaraman, and W. L. Wilkinson. Free coating of a newtonian liquid onto a vertical surface. *Chemical Engineering Science*, 29:389–396, 1974.

[99] Felix Staudegger, M. W. Hofbaur, and H.-J. Kruwinusa. Analyses and modeling of a wet-chemical-etch process on rotating silicon wafers with an impinging etchant jet. *Journal of The Electrochemical Society*, 156 (5):H340–H345, 2009.

[100] George Gabriel Stokes. On theories of the internal friction of fluids in motion. *Transactions of the Cambridge Philosophical Society*, 8:287–305, 1845.

[101] S. Thomas, A. Faghri, and W. Hankey. Experimental analysis and flow visualization of a thin liquid film on a stationary and rotating disk. *ASME Journal of Fluids Engineering*, 113:73–80, 1991.

[102] Željko Tuković and Hrvoje Jasak. Simulation of thin liquid film flow using OpenFOAM finite area method. Presentation at 4th OpenFOAM Workshop, Montreal, Canada, June 2009.

[103] O. Ubbink and R.I. Issa. A method for capturing sharp fluid interfaces on arbitrary meshes. *Journal of Computational Physics*, 153(1):26–50, jul 1999.

[104] Onno Ubbink. *Numerical prediction of two fluid systems with sharp interfaces*. PhD thesis, Imperial College of Science, Technology and Medicine, London, January 1997.

[105] J. D. van der Waals. *On the Continuity of the Gaseous and Liquid States*. PhD thesis, Leiden University, 1873.

[106] S.P Vanka. Block-implicit multigrid solution of navier-stokes equations in primitive variables. *Journal of Computational Physics*, 65(1):138–158, July 1986.

[107] H. K. Versteeg and W. Malalasekera. *An Introduction to Computational Fluid Dynamics: The Finite Volume Method*. Addison Wesley Longman Limited, Edinburgh Gate, Harlow, Essex CM20 2JE, England, 1995.

[108] Petr Víta, Bernhard Gschaider, Doris Prieling, and Helfried Steiner. Thin film flow simulation on a rotating disc. In J. Eberhardsteiner et al., editor, *ECCOMAS 2012 CD-ROM Proceedings*, 2012.

[109] Petr Víta and Bernhard F. W. Gschaider. Fast simulation of liquid films on a rotating disc. Presentation at Open Sourec CFD International Conference 2012, London, October 2012.

[110] C. B. Vreugdenhil. *Numerical Methods for Shallow-Water Flow*. Springer Netherlands, 1994.

[111] Tomasz Waclawczyk and Tadeusz Koronowicz. Comparison of CISCAM and HRIC high-resolution schemes for interface capturing. *Journal of Theoretical and Applied Mechanics*, 46(2):325–345, 2008.

[112] H. G. Weller, G. Tabor, H. Jasak, and C. Fureby. A tensorial approach to computational continuum mechanics using object-oriented techniques. *Computers in Physics*, 12 (6):620–631, November 1998.

[113] D. A. White and J. A. Tallmadge. Theory of drag out of liquids on flat plates. *Chemical Engineering Science*, 20:33–37, 1965.

[114] David C. Wilcox. *Turbulence Modeling for CFD*. DCW Industries, Inc., 1994 [1993].

[115] Gershon Wolansky and Abraham Marmur. Apparent contact angles on rough surfaces: the Wenzel equation revisited. *Colloids and Surfaces A: Physicochemical and Engineering Aspects*, 156(1-3):381–388, 1999.

[116] R. M. Wood and B. E. Watts. The flow, heat and mass transfer characteristics of liquid films on a rotating discs. *Chemical Engineering Research and Design*, 51:315–322, 1973.

[117] William Paul Woods. *The hydrodynamics of thin liquid films flowing over a rotating disc*. PhD thesis, Newcastle University, 1995.

[118] T. Yabe and P.-Y. Wang. Unified numerical procedure for compressible and incompressible fluid. *Journal of the Physical Society of Japan*, 60:2105–2108, 1991.

[119] C. Yih. Stability of liquid flow down an inclined plane. *Physics of Fluids*, 6(3):321–334, 1963.

[120] Kensuke Yokoi and Feng Xiao. Relationships between a roller and a dynamic pressure distribution in circular hydraulic jumps. *Phys. Rev. E*, 61(2):R1016–R1019, Feb 2000.

[121] Kenuke Yokoi and Feng Xiao. Mechanism of structure formation in circular hydraulic jumps: numerical studies of strongly deformed free-surface shallow flows. *Physica D: Nonlinear Phenomena*, 161(3-4):202–219, 2002.

[122] Steven T. Zalesak. Fully multidimensional flux-corrected transport algorithms for fluids. *Journal of Computational Physics*, 31(3):335–362, June 1979.

[123] J. G. Zhou and P. K. Stansby. 2d shallow water flow model for the hydraulic jump. *International Journal for Numerical Methods in Fluids*, 29:375–387, 1999.

[124] O. C. Zienkiewicz and R. L. Taylor. *The Finite Element Method*, volume Volume 3: Fluid Dynamics. Butterworth-Heinemann, fifth edition edition, 2000.

Acronyms

CFD Computational Fluid Dynamics

CFL Courant-Friedrichs-Lewy

CISCAM Compressive Interface Capturing Scheme for Arbitrary Meshes

CSF Continuum Surface Force

DIC Diagonal Incomplete-Cholesky

FA Finite Area

FCT Flux Corrected Transport

FD Finite Difference

FE Finite Element

FV Finite Volume

GAMG Geometric-Algebraic Multi-Grid

HRIC High Resolution Interface Capturing

IBL Integral Boundary Layer

LHS left hand side

NVD Normalised Variable Diagram

PBiCG Preconditioned Bi-Conjugate Gradient

PCG Preconditioned Conjugate Gradient

PISO Pressure Implicit Split of Operator

PLIC Piecewise Linear Interface Calculation

QUICK Quadratic Upwind Interpolation for Convective Kinematics

RANS Reynolds Averaged Navier-Stokes

RHS right hand side

SIMPLE Semi-Implicit Method for Pressure Linked Equations

SW Shallow Water

TFA Thin Film Approximation

TFM Thin Film Model

VoF Volume-of-Fluid

WRIBL Weighted Residual Integral Boundary Layer

Latin Symbols

A control area

$\mathbf{a}$ general vector value

A_b border control area

a_I general coefficient of the inlet cell

$\mathbf{a}_i$ polynomial velocity profile coefficient

a_N general coefficient of the neighbour cell

A_P control area around point

a_P general coefficient of the cell

b boundary edge, boundary edge centre

b film bottom

b_i polynomial normalised concentration profile coefficient

bvf boundary velocity factor

C normalised species concentration

$\mathbf{C}$ Courant number

c species concentration, mass fraction

$\tilde{C}$ normalised species concentration fluctuation

$\hat{C}$ polynomial normalised concentration profile

$\overline{C}$ mean normalised species concentration

c_p specific heat capacity at constant pressure

D diffusion coefficient

E edge flux

E total energy

e edge, edge centre

e internal energy

e_b border edge, border edge centre

e_k kinetic energy

$\mathbf{F}$ force

$\mathbf{F}_b$ body force

$\mathbf{Fr}$ Froude number

fs film free-surface

$\mathbf{g}$ gravity

h enthalpy

h film height

I inlet centre

$\mathbf{l}$ outward-pointing edge length vector

M molar mass

m mass

N neighbour cell centre

$\mathbf{n}$ outward-pointing surface unit normal vector

P owner cell centre

P point

p pressure

Q volumetric energy source

Q volumetric flow rate

$\mathbf{q}$ heat flux

R reaction rate

r radius

Re Reynolds number

s specific entropy

S_χ tensorial property source

$\mathbf{S}_S$ surface source

S_V volume source

T Cauchy stress tensor

T temperature

t time

Δt time step

$\overline{T}$ mean temperature

u velocity

$\tilde{\mathbf{u}}$ velocity fluctuation

$\hat{\mathbf{u}}$ polynomial velocity profile

$\overline{\mathbf{u}}$ mean velocity

v specific volume

V_M material volume

x position

Δx length interval

Greek Symbols

α heat transfer coefficient

α volume fraction

β reaction rate correction factor

χ tensorial property

Δr radial excentricity

δ boundary, separation line

δ_C concentration boundary

δ_T thermal boundary

ϵ rate-of-strain tensor

Γ_χ tensorial property coefficient

κ surface curvature

λ heat conductivity

μ dynamic viscosity

ν kinematic viscosity

ω rotational speed, speed of revolution

ϕ scalar property

ϕ_A acceptor property value

ϕ_D donor property value

ϕ_e edge property value

ϕ_f face property value

ϕ' scalar property time fluctuation

ϕ_I inlet property value

$\overline{\phi}$ scalar property mean value

ϕ_N the neighbour cell scalar property

ϕ_P the cell scalar property

ϕ^t scalar property at the time

ϕ_U upwind property value

ρ density

σ surface tension

τ deviatoric stress tensor

θ contact angle

$\varepsilon_{\hat{C}}$ normalised concentration profile error

$\varepsilon_{\hat{\mathbf{u}}}$ velocity profile error

ξ normalised z-coordinate

List of Figures

List of Tables